High Resolution Optical Microscopy
on Single Gold Nanoparticles

Dissertation

der Mathematisch-Naturwissenschaftlichen Fakultät

der Eberhard Karls Universität Tübingen

zur Erlangung des Grades eines

Doktors der Naturwissenschaften

(Dr. rer. nat.)

vorgelegt von

Tina Züchner

aus Reutlingen

Tübingen

2014

Tag der mündlichen Qualifikation: 21.07.2014

Dekan: Prof. Dr. Wolfgang Rosenstiel

1. Berichterstatter: Prof. Dr. Alfred J. Meixner

2. Berichterstatter: PD Dr. Marc Brecht

Danke…

Contents

Figures

Tables

Variables

ω	angular frequency			
ρ	charge density			
ε	complex permittivity			
σ	conductivity			
$\boldsymbol{\mu}$	dipole moment			
∇	divergence			
χ	electric susceptibility			
α	half-angle of the angular aperture			
μ	magnetic permeability			
φ	phase relation			
α	polarizability			
λ	wavelength			
$\omega(z)$	beam radius			
$\eta(z)$	phase correction			
$\varepsilon(\omega)$	dielectric function			
ε_0	electric field constant			
μ_0	magnetic field constant			
ρ_{Au}	density of gold			
ω_p	plasma frequency			
$\Delta x,\ \Delta z$	diffraction limit along x, z			
∂	partial derivative			
ξ_l	Ricatti-Bessel function			
Φ	quantum efficiency			
ψ_l	Ricatti-Bessel function			

A	area		*L*	geometrical factor
a	particle length		**m**	degree of the mode
a_l	scattering coefficient		**M**	magnetization
B	magnetic induction		*m*	mass
b	particle width		*M*	molecular weight
b_l	scattering coefficient		N	noise
c	concentration		*N*	number
C	cross-section		**n**	order of the mode
c	speed of light		*n*	refractive index
d	diameter		N_A	Avogadro's Number
D	electric displacement		*NA*	numerical aperture
e	electric charge		$n_{x,y}$	unity vector along x, y
E	electric field		**P**	polarization
Ext	extinction		*QF*	quality factor
F_{enh}	enhancement factor		**Q**	efficiency
h	height		*R*	aspect ratio
H	magnetic field		*R(z)*	wavefront radius
I	intensity		S	signal
j	current density		*t*	time
k	absorption coefficient		*V*	volume
k	wave vector			

Abbreviations

abs	absorption	PL	photoluminescence
AFM	atomic force microscopy	PMT	photomultiplier tube
APD	avalanche photo diode	PP	particle-plasmon
APDM	azimuthally polarized doughnut mode	PSF	point spread function
		PVA	polyvinylalcohol
BG	background	*ref*	reflection
CCD	charge coupled device	RPDM	radially polarized doughnut mode
conf	confocal		
CTAB	cetyltrimethylammonium bromide	rpm	rotations per minute
		sca	scattering
DAPI	4',6-Diamidino-2-phenylindole	SEM	scanning electron microscopy
DDA	discrete dipole approximation	SERS	surface-enhanced Raman scattering
det	detected		
DM	doughnut mode	SHG	second harmonic generation
EM	electron microscopy	SNOM	scanning near-field optical microscopy
ext	extinction		
FWHM	full width at half maximum	SNR	signal-to-noise ratio
HeNe	helium-neon	SP	surface-plasmon
HG	Hermite-Gaussian	SPR	surface-plasmon resonance
HOLM	higher order laser mode	STED	stimulated emission depletion microscopy
LG	Laguerre-Gaussian		
long	longitudinal	STORM	stochastic optical reconstruction microscopy
LPGM	linearly polarized Gaussian mode		
		TEF	tip-enhanced fluorescence
M	molar (mol/l)	TEM	transmission electron microscopy
MC	mode conversion		
min	minute	TENOM	tip-enhanced near-field optical microscopy
mM	millimolar (mmol/l)		
NA	numerical aperture	TERS	tip-enhanced Raman scattering
NF	near-field	TIR	total internal reflection
PALM	photoactivated localization microscopy	*trans*	transversal
		WP	wave plate
PH	pinhole		

1 Introduction

The broad field of nanotechnology has found its way into everyday life in recent years. Nano sells. Nanosized matter is used in textiles as stain- and water-resistant finish or as anti-bacterial treatment, for which silver nanoparticles are most important.[1] They are also found as food additives, *e.g.* silica nanoparticles are used as thickener in tomato ketchup.[1] In suntan lotion, nano pigments of titanium dioxide and zinc oxide nanoparticles are common UV filters.[1] Nanoscaled matter has been exploited for decades to improve the properties of varnish.[1] However, since nanotechnology and nanoscience comprises matter with dimensions ranging from single atoms or molecules to 100 (or a few hundred of) nanometres, the field is of great variety. A general finding for nanosized material is, however, that the physical properties are quite different from the bulk material. Upon reducing the size of an object towards the nanometre scale, the number of the surface atoms in relation to the volume atoms becomes more dominant. Therefore, the surface atoms play an increasingly important role in the physical properties of nanoparticles and the observed characteristics thus vary from the bulk material. When the dimensions are further reduced, the material gradually changes its properties towards the molecular state, that is the electronic properties finally become different. However, such effects are only observed for extremely small nanoparticles which might as well be considered as (almost) molecular clusters. For larger nanoparticles, typically consisting of a few thousand atoms and more, the electronic bulk band structure is preserved.

Here, gold nanoparticles were studied, which have remarkable optical properties that do in no means resemble to ones of bulk gold, when the particle size is considerably smaller than the wavelength of visible light. Aqueous solutions of spherical nanoparticles with diameters of approximately 100 nm or smaller are bright red in transmission. For gold nanorods, the colour depends on the aspect ratio R of the particles, that is the ratio of the length a over the width b. Consequently, the optical properties can be tuned when controlling the particle size and the whole

visible spectrum as well as the near infrared can be covered. A number of different methods to synthesize gold nanorods with a highly defined aspect ratio are nowadays available with a particle width of approximately 15 to 25 nm. The physical process being responsible for these extraordinary optical properties is the excitation of collective electron oscillations in the particles, the so-called particle-plasmon (PP) or surface-plasmon (SP) oscillation, through visible light. As a consequence of the SP excitation, the particles strongly scatter the light which holds responsible for the bright colours of the solutions. In addition to the strong scattering, the emission of photoluminescence (PL) can be observed from nanostructured gold, *e.g.* from rough gold films or nanoparticles.[2-13]

To optically characterize nanoparticles, confocal microscopy is well suited. It offers high sensitivity and thus allows to study single particles. In addition, the combination with different spectroscopic methods provides further possibilities. Thus, comparable to the well established field of single molecule microscopy, the microscopy of single nanoparticles, or more generally speaking, single nanoobjects has evolved in the last years. The implementation of laser modes with special polarization properties opens up a variety of different possibilities for optical microscopy. Doughnut modes (DMs) can be especially useful in various optical techniques.[14] Besides their established application in apertureless scanning near-field optical microscopy (SNOM),[15, 16] they allow to increase the optical resolution not only in standard confocal microscopy but also in surface-plasmon resonance (SPR) imaging[17-23] or second harmonic generation (SHG) microscopy[24, 25]. Applied in superresolution techniques like stimulated emission depletion (STED) microscopy[26], DMs provide a way to achieve optical resolutions well below the diffraction limit. Because of their special polarization properties, other applications also benefit from the implementation of DMs. The efficiency and stability of optical traps or tweezers, for example, is often increased when the trap is built with a DM.[27-32] Even the industrial laser drilling and cutting of metals is improved by DMs.[33, 34] In this work, however, confocal microscopy with azimuthally and radially polarized

doughnut modes (APDM and RPDM) is of main interest. Additionally, some measurements with apertureless SNOM were undertaken.

This work shows the possibilities provided by the combination of confocal microscopy with DMs to image and characterize individual gold nanoparticles of different shapes,[35-41] mainly gold nanorods and nanotriangles. For example, through the acquisition of either the elastically scattered or PL light, the particle orientation can be directly visualized. It can be determined both in 2D and 3D. Spontaneous particle rotations can be followed, even when not accompanied by a lateral movement of the particle. The scattering data also comprises information about the sample interface. Moreover, differently shaped particles can be distinguished without further data analysis. In the case of gold nanotriangles, particle orientation is mapped and different sizes can be distinguished.

Gold nanoparticles are taken up by cells without having a toxic effect.[42-44] In fact, spherical gold nanoparticles are frequently used as labels in electron microscopy (EM). Therefore, it is straightforward to think about using gold nanorods as similar labels for optical microscopy in biological samples. Compared to standard fluorescent dyes, their optical stability is much higher and their toxicity is expected to be lower. Preliminary results in this work show that the particles can be detected in the environment of a cell, showing that the particles are incorporated even without further functionalisation of their surface.

When SPs are excited in nanometre sized structures with a high surface curvature, considerable field enhancements can be observed at the points of the largest curvature. This effect is exploited *e.g.* in apertureless SNOM, where a sharp metal probe is excited with an external electric field polarized along the tip-axis. The excitation of SPs along the tip-axis produces a highly confined and enhanced field at the tip-apex. A similar effect is to be expected at the tips of gold nanorods as could be confirmed by near-field measurements on individual gold nanorods showing a pronounced localized increase in PL emission.

2 Theoretical Background

In this chapter, it shall be shown how the scattering and absorption of gold nanoparticles can be explained theoretically. Prerequisites are Maxwell's equations and the dielectric function of gold. The Mie theory, as well as its extension to ellipsoidal particles by Richard M. Gans shall be shortly introduced afterwards. Finally, the PL of nanostructured gold is treated.

2.1 Optical Properties of Gold Nanoparticles

In gold nanoparticles, light at optical frequencies excites collective oscillations of electrons, the so-called particle- (PP) or surface-plasmons (SPs). Therefore, gold nanoparticles strongly absorb and scatter the electromagnetic field especially in the visible and (near) infrared region of its spectrum. Their spectral properties depend on the shape, size and direct environment of the particles. In the beginning of the 20th century, Gustav Mie developed a theory to calculate the optical properties of spherical metal particles in liquid medium,[45] using a special class of solutions for Maxwell's equations. Later, his theory was extended to elliptical particles by Richard M. Gans.[46] The so-called Mie or Mie-Gans theory (depending on the shape of the respective particles) is valid not only for metallic nanoparticles of different sizes, but also *e.g.* for dielectric particles like water droplets. Applications range from the optical properties of colloidal solutions and the colour of the rainbow to the analysis of dust clouds or aerosols:[47] Sometimes, for simplicity, the particles are treated in the so-called electrostatic approximation which also shall be introduced in this chapter. The optical properties strongly depend on the dielectric function of the particle's material, in our case gold. Therefore, the experimentally measured values for bulk gold are crucial and deserve a careful discussion. Finally, the phenomenon of PL from gold and a discussion of the underlying processes concludes this chapter.

2.1 Optical Properties of Gold Nanoparticles

2.1.1 Maxwell's Equations

Mie's theory on the optical properties of spherical particles is based on the solution of Maxwell's equations. Therefore, they shall be shortly introduced in the following. Generally speaking, they describe the interaction of light with matter. James C. Maxwell found a short mathematical description for electromagnetic fields combining the laws of Faraday, Gauß and Ampère. His equations describe the dynamics of the electric and magnetic fields $\mathbf{E}$ and $\mathbf{H}$, and relate the fields to their respective sources, the charge and current densities ρ and $\mathbf{j}$, thus forming the basis of electrodynamics. In SI units, the macroscopic Maxwell's equations may be written as:[16, 47, 48]

$$\nabla \cdot \mathbf{D} = \rho \tag{2.1}$$

$$\nabla \cdot \mathbf{B} = 0 \tag{2.2}$$

$$\nabla \times \mathbf{E} = -\frac{\partial \mathbf{B}}{\partial t} \tag{2.3}$$

$$\nabla \times \mathbf{H} = \mathbf{j} + \frac{\partial \mathbf{D}}{\partial t} \tag{2.4}$$

with the divergence ∇, the electric displacement $\mathbf{D}$, the magnetic induction $\mathbf{B}$ and the time t. $\mathbf{D}$ and $\mathbf{H}$ are usually defined as:

$$\mathbf{D} = \varepsilon_0 \mathbf{E} + \mathbf{P} \text{ and } \mathbf{H} = \frac{\mathbf{B}}{\mu_0} - \mathbf{M} \tag{2.5}$$

where $\mathbf{P}$ is the electric polarization, $\mathbf{M}$ the magnetization, ε_0 and μ_0 the electric and magnetic field constants (or permittivity and permeability of free space).

The constitutive relations describe the generation of currents and charges in matter, and result for a linear homogeneous and isotropic medium as:

$$\mathbf{P} = \varepsilon_0 \chi \mathbf{E}, \ \mathbf{B} = \mu \mathbf{H} \text{ and } \mathbf{j} = \sigma \mathbf{E} \tag{2.6}$$

with the phenomenological coefficients of the respective medium, the electric susceptibility χ, the magnetic permeability μ and the conductivity σ. For a linear

medium, they are independent of the occurring fields while they become a function of space for inhomogeneous media and of direction for an anisotropic one.

An electromagnetic wave travelling in vacuum normally does not feel the influence of any field source, current or magnetic/electric charge. Therefore, one can assume $\rho = 0$ and $\mathbf{j} = 0$ to derive the wave equation for an electromagnetic field propagating in homogenous medium far away from any field source:[49]

$$\nabla^2 \mathbf{E} + \varepsilon_0 \mu_0 \frac{\partial^2 \mathbf{E}}{\partial t^2} = 0 \,. \tag{2.7}$$

The wave equation can be solved separating the time and space dependency:

$$\mathbf{E}(x,y,z,t) = \mathbf{A}(t) \cdot \mathbf{B}(x,y,z) \,. \tag{2.8}$$

With $\mathbf{A}(t) = e^{i\omega t}$ as well as the angular frequency $\omega = c \cdot k$, the wave vector k and the speed of light $c = 1/\sqrt{\mu_0 \varepsilon_0}$, the Helmholtz equation can be derived:

$$\nabla^2 \mathbf{E} + k^2 \mathbf{E} = 0 \tag{2.9}$$

describing the spatial dependence of an electromagnetic field in vacuum. Consequently, solutions to the Helmholtz equation describe the propagation of electromagnetic fields in vacuum. The time dependence of the electromagnetic field is assumed to be harmonic and therefore a solution to the general time-harmonic field $\mathbf{E} = \mathbf{A} \cdot \cos(\omega t) + \mathbf{B} \cdot \sin(\omega t)$:

$$\mathbf{E}(x,t) = \mathbf{C} \cdot e^{-i\omega t} \,,\ \mathbf{C} = \mathbf{A} + i\mathbf{B} \,. \tag{2.10}$$

2.1 Optical Properties of Gold Nanoparticles

Alternatively, a time dependency of $e^{+i\omega t}$ could be used, but here, the usual sign convention shall be followed. Together with the constitutive relations 2.6, Maxwell's equations can be written as:

$$\nabla \cdot (\varepsilon \mathbf{E}) = 0 \tag{2.11}$$

$$\nabla \cdot \mathbf{B} = 0 \tag{2.12}$$

$$\nabla \times \mathbf{E} = i\omega\mu\mathbf{H} \tag{2.13}$$

$$\nabla \times \mathbf{H} = -i\omega\varepsilon\mathbf{E} \tag{2.14}$$

where ε is the complex permittivity $\varepsilon = \varepsilon_0(1+\chi) + i\dfrac{\sigma}{\omega}$.

With the appropriate boundary conditions and the energy conversion, this set of equations allows to describe the time and spatial dependent propagation of electromagnetic fields in matter. For particular interest in this work are a class of solutions for the Helmholtz equation describing special laser modes which will be introduced in the following.

2.1.2 Higher Order Laser Modes

In the optical resonator of a laser, the laser cavity, many different electromagnetic modes can oscillate. However, for practical purposes, mainly single mode lasers are used. As these modes travel outside the laser cavity, they can also be called laser beams and thus, both terms are used in the literature. In most cases, the fundamental Gaussian mode is the one desired to exit the laser. Its intensity in the cross-section follows a Gaussian distribution. Different polarization states are found regularly, as *e.g.* a linear, circular or elliptical one. Higher order modes, however, show different intensity distributions with Hermite-Gaussian (HG) and Laguerre-Gaussian (LG) modes being most popular. Depending on the laser cavity geometry, or, more precisely, the geometry of the laser mirrors, modes from one of these two families are resonant inside the cavity. For rectangular mirrors, HG-modes are found, while LG-modes can be created with circular mirrors.[16] These modes are solutions of the Helmholtz equation and mathematically they can be described as follows:

$$\text{Gaussian mode:} \quad \mathbf{E}(x,y,z) = \mathbf{E}_0 \frac{w_0}{w(z)} e^{-\frac{x^2+y^2}{w^2(z)}} e^{i\left[kz-\eta(z)+\frac{k\left(x^2+y^2\right)}{2R(z)}\right]} \tag{2.15}$$

$$\text{HG-modes:} \quad \mathbf{E}_{nm}^{HG}(x,y,z) = w_0^{n+m} \frac{\partial^n}{\partial x^n} \frac{\partial^m}{\partial y^m} \mathbf{E}(x,y,z) \tag{2.16}$$

$$\text{LG-modes:} \quad \mathbf{E}_{nm}^{LG}(x,y,z) = k^n w_0^{2n+m} e^{ikz} \frac{\partial^n}{\partial z^n} \left(\frac{\partial}{\partial x} + i\frac{\partial}{\partial y}\right)^m \left[\mathbf{E}(x,y,z)e^{-ikz}\right] \tag{2.17}$$

with the beam radius $w(z) = w_0\sqrt{1+\frac{z^2}{z_0^2}}$, the beam radius w_0 of the Gaussian beam, the wave vector $k = \frac{2\pi n}{\lambda}$, the phase correction $\eta(z) = \arctan\frac{z}{z_0}$, the wavefront radius $R(z) = z\left(1+\frac{z_0^2}{z^2}\right)$, and the order $\mathbf{n}$ and the degree $\mathbf{m}$ of the beam. The electric field distribution as well as the intensity distribution can be equivalently described with HG- and LG-modes. Examples for some HG-modes are given in Figure 1, with the intensity resulting from the squared electric field $\mathbf{I}(x,y,z) = |\mathbf{E}(x,y,z)|^2$.

2.1 Optical Properties of Gold Nanoparticles
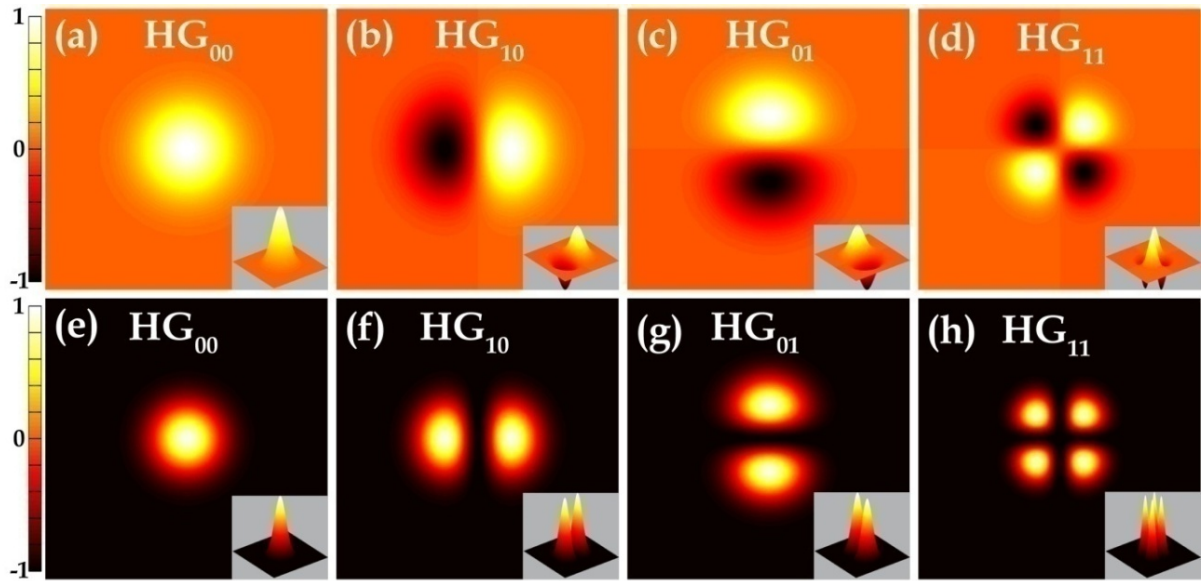
Figure 1:   Calculated, normalized electric fields (a-d) and intensity distributions (e-h) in the *xy*-plane of Hermite-Gaussian (HG$_{nm}$)-modes of different order **n** and degree **m** as indicated. The insets show a 3D representation of the respective graphs. Please note the different phases of the electric fields in (b-d), which are separated by the nodal planes and indicated by the underlying colour code and by the corresponding 3D representations.[1]

The zeroth order mode, the HG$_{00}$ follows a Gaussian distribution in its cross-section, as can be recognized from the 3D representation in the inset of Figure 1 a. For the higher order modes, nodal planes are included which divide the modes in parts of negative and positive phase, as indicated by the underlying colour code in Figure 1 b-d and by the corresponding 3D representations (insets). For practical applications, the intensity distributions, *i.e.* the squared field distributions of the respective modes are of more interest and are given in Figure 1 e-h.

In general, every mode oscillating in a laser cavity can be described as a super-position of HG- or LG-modes. Of particular interest for this work are the so-called doughnut modes (DMs) with a ring-shaped beam profile. Since these modes have been used and studied in many different fields of science,[14] varying names are found in the literature. As an example, they are often generally referred to as higher

---

[1] All calculations concerning DMs were generated with a Matlab® code written by Dr. Antonio Virgilio Failla based on the description in [16].

order laser modes (HOLMs)[16, 41] or as (cylindrical or optical) vector beams[50-53]. In some literature, they are simply called doughnut beams[33, 54-56] or doughnut modes (DMs)[16, 33, 36, 57-59], as they will be referred to here as well. They can be obtained combining a HG_{10}- and a HG_{01}-mode (see eq. 2.18, 2.19 and Figure 2). Because of their shape, these modes allow all possible states of polarization, *e.g.* radially and azimuthally polarized doughnut modes (RPDM/APDM) can be generated:

$$RPDM = n_x HG_{10} + n_y HG_{01} \tag{2.18}$$

$$APDM = -n_y HG_{10} + n_x HG_{01} \tag{2.19}$$

with the unit vector $n_{x,y}$ giving the polarization of the respective mode.

A graphical representation of these intensity summations is shown in Figure 2 where the polarizations are indicated by the blue arrows.
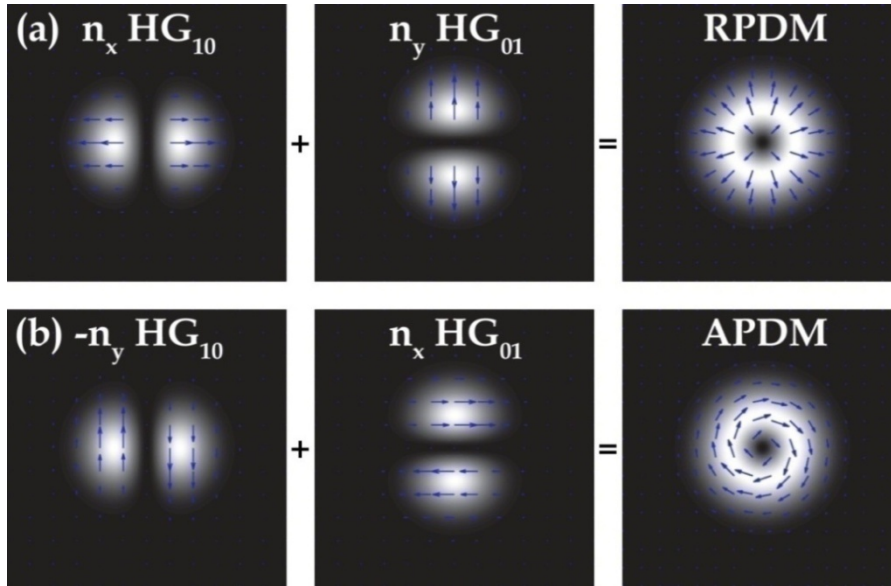
Figure 2:   Schematic summation of first order HG-modes to create a radially (a) or azimuthally (b) polarized doughnut mode (RPDM/APDM) with the blue arrows indicating the polarization as given by the unit vector $n_{x,y}$.

For the radial mode, the polarization vectors are aligned like the crossings of a wheel. In the case of the APDM, the vectors follow the rim of the wheel and are oriented in clockwise or anticlockwise direction (see Figure 2, to the right). Both modes offer different orientations of the polarization at any moment in time, thus providing especially appealing opportunities for microscopic applications.

2.1 Optical Properties of Gold Nanoparticles

Focusing of Doughnut Modes

The electric field distribution of a collimated beam focussed with a high numerical aperture (*NA*) objective lens can be described and hence calculated with a series of plane waves converging under different angles.[16, 60-62]

Since the electric field of a DM varies from that of the linearly polarized Gaussian beam, the behaviour upon tight focusing is also different.[16] For an APDM, the full width at half maximum (FWHM) of the focal spot is considerably larger than for a Gaussian beam and in the order of a wavelength since the ring shape is preserved. Figure 3 a shows the calculated field intensity distribution of an APDM in focus (*NA* = 1.25, λ = 633 nm) together with the normalized cross-section taken along the dashed line in b.[2]
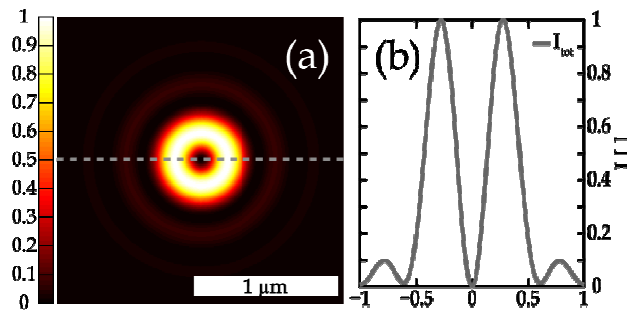
Figure 3: Normalized calculated field intensity of an APDM in focus (*NA* = 1.25, λ = 633 nm) at a glass-air interface. (a) In the *xy*-plane, the ring shape is preserved and the polarization in focus is fully transversal. (b) Normalized cross-section taken along the dashed line. The FWHM in the focal plane is in the order of one wavelength.[2]

An APDM is fully transversally polarized in focus, *i.e.* the polarization is preserved as in the beam profile and lies in the sample plane. Please note that this polarization distribution is purely 2D but offers different orientations of the polarization vectors at any moment in time.

---

[2] All calculations concerning DMs were generated with a Matlab® code written by Dr. Antonio Virgilio Failla based on the description in [16].

For a RPDM, the focal properties are remarkably different. Upon tight focusing, the polarization splits into two field components, a transversal and a longitudinal one. While the transversal component preserves the ring shape, the longitudinal component forms a spot. The calculated field intensity distribution is plotted in Figure 4.
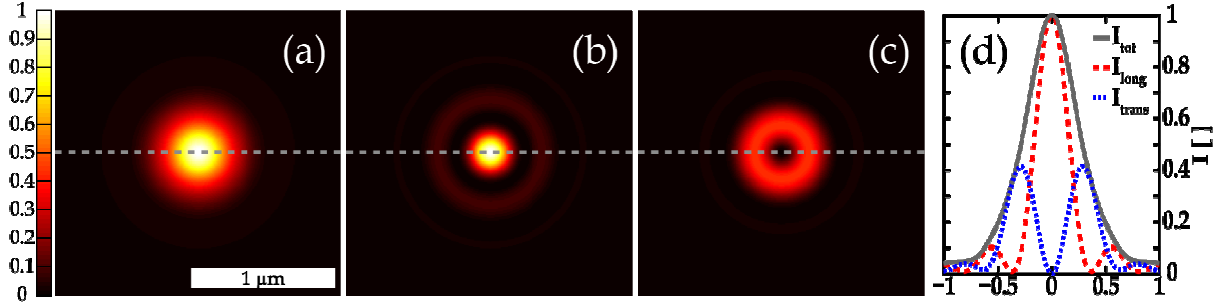
Figure 4:   Calculated field intensity of a RPDM in focus (NA = 1.25, λ = 633 nm) at a glass-air interface normalized with respect to the total field intensity. (a) Total, (b) longitudinal, (c) transversal field intensity in the xy-plane with equal intensity scales in (a-c) as provided by the underlying colour code. (d) Cross-sections taken along the dashed lines (continuous grey line: total intensity, dashed red line: longitudinal intensity, dotted blue line: transversal intensity). Please note that the longitudinal component overwhelms the transversal one by a factor > 2. While the FWHM of the transversally polarized component is in the order of a wavelength, the FWHM of the longitudinally polarized component is much smaller. This component is tighter focused than a conventional Gaussian beam.[3]

First, the total field intensity distribution is shown in Figure 4 a. The longitudinal and transversal components are depicted in b and c, respectively. The intensity scale is normalized with respect to the total field intensity and the underlying colour code is scaled equally in all cases. Cross-sections along the dashed lines are plotted in d. Please note that the longitudinal component is focused more tightly than the transversal one. The relative intensity of the two components depends on the applied NA. For a $NA \geq 1$, the longitudinal field intensity overwhelms the transversal one.[16] This effect becomes more pronounced with an increasing NA since the light is focused under higher angles. While the transversal component is mainly formed by

---

[3] All calculations concerning DMs were generated with a Matlab® code written by Dr. Antonio Virgilio Failla based on the description in [16].

low angular components, the longitudinal component consists of high angular components. Hence, an increasing opening angle favours the longitudinal component compared to the transversal one. Interestingly, this is a purely geometric effect since it does not depend on the refractive properties of the lens. It has been shown that there is no difference between an air-objective and an oil-immersion objective when corrected for the opening angle.[50] Such angular filtering can also be applied by influencing the shape of the parallel beam. When the dark central part of the DM is increased, *e.g.* with a circular beam stop (also called annular aperture), low angular components are blocked and the transversal component is weakened compared to the longitudinal one. This results in even tighter focusing of the longitudinal component.[63]

So far, the electric field properties of light were concerned. Regarding the magnetic component of light, the two modes are behaving exactly contrarily, *i.e.* the corresponding magnetic field distribution of the electric APDM is radially polarized, thus, it is a magnetic RPDM and vice versa.[50, 64] For example, the magnetic dipole absorption of a spherical quantum dot has been probed with an APDM. Since the selection rules differ from the ones for the electric dipole moment, they could be differentiated. Additionally, an increased resolution could be achieved depending only on the mode quality and the quantum dot size.[64]

2.1.3 The Dielectric Function of Gold

The optical properties of metals are governed by the response of their electrons to light of different energy. For most metals, the free electrons play the key role in this process, and partly this also holds for the noble metals. The optical response of the free electrons can be described with the Drude-Lorentz-Sommerfeld model. The free electrons are all acting in phase upon an external force, delivered by the electric part of the driving field (permeability μ is assumed to be unity). A coupling of the electrons to the ion core can be introduced with an effective electron mass instead of the real electron mass. The model results in the Drude or plasma frequency $\omega_p = \sqrt{\dfrac{Ne^2}{\varepsilon_0 m_e}}$ with the number of electrons N, the electric charge e, the electric field constant ε_0 and the electron mass m_e. For the noble metals, another important contribution to the dielectric function arises from interband transitions. This part sensitively depends on the band structure and the density of states in the Brillouin zone. Naturally, the deeper core levels also contribute.[65]

For theoretical calculations of the optical properties of metal particles, values for the dielectric function $\varepsilon(\omega)$ for the respective material are needed. Normally, such data base upon experimental measurements. There are many different techniques available, for bulk samples and thick gold films, *e.g.* ellipsometry[66, 67] and light reflected under different angles[68-74] are the most common ones while transmission measurements are suitable for thin films.[68, 72, 75] Since the real and imaginary part of the dielectric function are dependent on each other, data analysis often involves a Kramers-Kronig analysis.[71, 73, 74] Such an analysis is suitable for any frequency dependent function which linearly relates an output with an input. The problem usually involved is that of extrapolation.[65]

From the measured refractive index n and the absorption coefficient $\mathbf{k}$ $\left(\tilde{n} = n + i\mathbf{k} = \sqrt{\varepsilon} \right)$, the real and complex part of the dielectric function $\tilde{\varepsilon} = \varepsilon_1 + i\varepsilon_2$ can be calculated:

$$\varepsilon_1 = n^2 - \mathbf{k}^2 \text{ and } \varepsilon_2 = 2n\mathbf{k}. \tag{2.20}$$

2.1 Optical Properties of Gold Nanoparticles

The earliest data cited here was measured by Weiss in 1948 and only covers a small energy range of roughly 1 eV.[76] Comparable values have been found a few years later by Schulz[68, 75] or Otter[77], although obtained with differently prepared samples and with other approaches. In the 1960s, a large energyrange was covered, *e.g.* by Padalka and Shklyarevskii[78] as well as Dold and Mecke[66]. The most interesting range in-between 1 and 7 eV was carefully covered in the early 1970s by Irani and coworkers[71] as well as by Johnson and Christy[72], which are probably the most commonly cited values today. The experimentally found values are plotted in Figure 5, both as a function of photon energy (a, b) and wavelength (c, d).[66, 68, 71, 72, 75-78] To visualize the special features, Figure 5 b, d provide a different scaling.
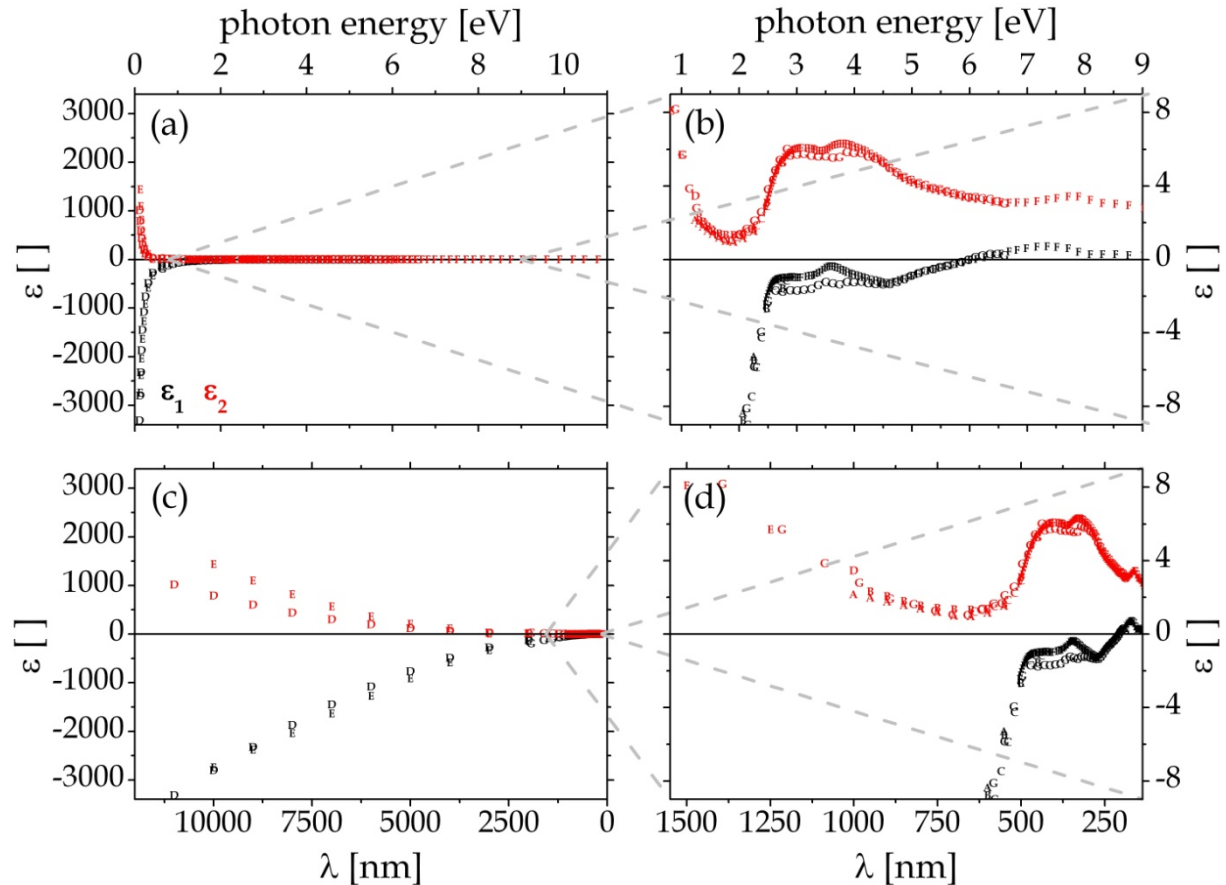
Figure 5: Experimentally measured real (ε_1) and imaginary (ε_2) part of the dielectric function for gold as a function of photon energy (a, b) and wavelength (c, d). (a, c) show a broad energy range while (b, d) visualize the special features in more detail. Experimental data have been taken from the literature as follows: A[76], B[68, 75], C[77], D[78], E[66], F[71] and G[72].

In the infrared, the optical constants are dominated by the free electrons while in the visible and ultraviolet range, interband absorption becomes appriciable. Therefore, the metal band structure plays the keyrole in this energyrange.[72] The steep rise in ε_2 close to 2.5 eV (500 nm) has been attributed to states from the *d*-band to Fermi-levels close to the L-symmetry point in the first Brillouin zone, while the edge arising around 1 eV (1250 nm) could be assigned to transitions close to the X-symmetry point where the density of states is very high in both cases. Thus, the interband absorption edge splits into two separate contributions due to the band structure of gold.[79]

Considering gold nanoparticles, the question remains how appropriate it is to work with the optical constants from bulk metal. For gold films, it has been shown that the dielectric function becomes that of the bulk material as soon as a film thickness of 25 to 30 nm is exceeded.[72] In the case of nanoparticles, the optical properties seem to be somewhat comparable or homogenous starting from a particle size of 10 nm.[65] However, this appears to be more like a rule of thumb, to be on the safe side. Nevertheless, for very small particles, the dielectric function depends on the particle size. Extremely small particles behave more like molecules with discrete energy levels which smear out more and more with increasing size until they finally become bulk-like. For silver nanoparticles, bulk-like behaviour is reached as soon as approximately 400 atoms are clustered together which corresponds to a particle size of 2.2 nm.[65, 80] Reasonably, a similar number of atoms can be expected for gold nanoparticles.

2.1 Optical Properties of Gold Nanoparticles

The number of atoms N in a metal nanoparticle can be estimated from the volume of the particle and the density of the metal $\rho_{Au} = 19.3 \frac{g}{cm^3}$. For a sphere, the volume is given with $V_{sp} = \frac{\pi d^3}{6}$ and from the particle's mass $m = \frac{N M_{Au}}{N_A} = \rho_{Au} V_{sp}$ the number of atoms N and the diameter d result as:

$$N = \frac{\rho_{Au} \pi d^3 N_A}{6 M_{Au}} \quad \text{and} \quad d = \sqrt[3]{\frac{6 M_{Au} N}{\pi \rho_{Au} N_A}} , \tag{2.21}$$

with Avogadro's Number N_A and the molecular weight $M_{Au} = 196.97 \frac{g}{mol}$. Numerical values for particle sizes treated in this work are summarized in Table 1.

Table 1: Estimated number of atoms N and volume V_{sp} of spherical gold nanoparticles for various diameters d following eq. 2.21. V_{sp} is given for better comparison with the data for ellipsoidal particles in Table 2.

d [nm]	2.3	5	10	20	40	50	60	80
N [ ]	400	$3.9 \cdot 10^3$	$3.1 \cdot 10^4$	$2.5 \cdot 10^5$	$8.3 \cdot 10^5$	$2.0 \cdot 10^6$	$3.9 \cdot 10^6$	$6.7 \cdot 10^6$
V_{sp} [nm³]	6.8	65	520	$4.2 \cdot 10^3$	$1.4 \cdot 10^4$	$3.4 \cdot 10^4$	$6.5 \cdot 10^4$	$1.1 \cdot 10^5$

Table 1 shows that similar sizes result for silver and gold nanoparticles (400 atoms correspond to $d \approx 2$ nm) since the differences in the density and the molecular weight of the two metals almost perfectly compensate each other. A 5 nm-sphere consists of approximately 4000 gold atoms and should therefore act rather bulk-like.[65, 80] However, the optical spectrum differs from that of the larger particles (see chapter 0, p. 53). Therefore, this size range somehow represents a transition state. For the larger particles, the number of atoms dramatically increases with particle size.

In this work, gold nanorods and their optical properties are of main interest. Therefore, not only spherical particles shall be considered here. For metal nanorods, their shape has to be approximated in some way. Such an estimation might consider the particle as a cylinder with two hemispheres as end caps. The cylinder height, which enters the calculation of the particle volume V_{rod}, results as the difference of the long and short particle axis a and b. Hence, the particle volume can be expressed as

$$V_{rod} = \frac{\pi a b^2}{4} - \frac{\pi b^3}{12} \text{ and } N = \frac{\rho_{Au} \pi N_A b^2}{2 M_{Au}} \left(\frac{a}{2} - \frac{b}{6} \right). \tag{2.22}$$

The resulting numbers for gold nanorods with $b = 20$ nm as treated here are presented in Table 2 with the aspect ratio $R = a/b$ as a size parameter. The volumes V_{rod} are given for better comparison of particle sizes with the data for the spherical particles listed in Table 1.

Table 2: Estimated number of atoms N in gold nanorods for various aspect ratios R ($b = 20$ nm) following eq. 2.22. The particle volume V_{rod} is given for better comparison with the data for spherical particles in Table 1.

R [ ]	1.9	2.5	3.0	3.5	3.8
N [ ]	$5.8 \cdot 10^5$	$8.0 \cdot 10^5$	$9.9 \cdot 10^5$	$1.2 \cdot 10^6$	$1.3 \cdot 10^6$
V_{rod} [nm^3]	$9.8 \cdot 10^3$	$1.4 \cdot 10^4$	$1.7 \cdot 10^4$	$2.0 \cdot 10^4$	$2.2 \cdot 10^4$

As can be recognized from Table 2, the gold nanorods possess a relatively large number of atoms, at least compared to the smaller gold spheres. Therefore, their electronic and optical properties can be safely regarded as bulk-like, similar as for the gold nanospheres with diameters above 10 nm.

2.1.4   Scattering and Absorption of Gold Nanoparticles

2.1.4.1   Mie Theory

Based on the electromagnetic theory, Gustav Mie found a rigorous solution of Maxwell's equations for the case of the diffraction of a plane monochromatic wave by a sphere of any material or diameter in a homogenous medium.[47, 61] Although the most common term for the considered work is that of the Mie theory, several scientists have contributed to the field. Peter Debye approached the closely related problem of the light pressure upon a spherical particle during his dissertation in parallel with Mie's work.[81] Similar results had been achieved even several years earlier by the Danish physicist Ludvig Valentin Lorenz based not on Maxwell's equations but on his own electromagnetic theory.[82] For this reason, in combination with the publication of the original work in Danish, his results have tended to be overlooked.[83] Independently of any historic facts, the work will be referred to here as Mie theory in accordance with most of the literature.

Mie concentrated on gold spheroids, but his theory can be applied to other materials as well. In general, his results hold for any kind of particles, if a dielectric function can be defined. This includes that neither the size or the material of the particles nor the energy of the electromagnetic wave influence the validity of his theory as long as the particles are sufficiently spherical and isolated from each other. Therefore, the Mie theory has found wide application in different fields of science ranging from the "original" nanoparticles applications to atmospheric optics, gas as well as aero- and hydrosol analysis to the examination of interstellar dust clouds. The Mie theory allows insight into the near as well as the far-fields of the particles, their absorption and angular dependent scattering. Because of the particles' high symmetry, the extinction spectra usually show resonance phenomena. Small, absorbing particles often show so-called Mie resonances due to interband transitions, plasmon-polariton excitations, phonons or excitons, depending on the material in question.[47, 61, 84, 85]

The excitation light is treated as a plane wave and Maxwell's equations are solved in polar coordinates, for convenience. Following his theory, the scattered light can be described with a series of partial waves, formed by the electrical and magnetic vibrations of the particles. Practically, only a limited number of these waves has to be taken into account, with the number depending on the particle size. The small particle diameters in colloidal solutions allow to only consider the first electrical vibration, the so-called Rayleigh radiation, since the contributions of the higher terms are negligible. Only for larger particles well above 100 nm in diameter, the second electrical as well as the first magnetic partial wave are appreciable.[45]

As a consequence, it is described how small particles scatter the light equally in the forward and backward direction. But with increasing size, scattering in the forward direction becomes dominant which is accounted for by the partial waves of higher orders.[48]

2.1.4.2 Mie-Gans Theory

A considerable drawback of Mie's theory is the assumption of a spherical shape for the particles as has been already pointed out by Gans in his extension of the Mie theory.[46] In his work, he considered rotationally symmetric ellipsoids. Again, as he already stated in his original publication, this limitation to an arbitrarily chosen particle geometry might be objectionable, but necessary in order to keep the mathematics manageable. Nevertheless, his results were in accordance with experimental findings which so far could not have been explained with the original Mie theory.[46] This theoretical work treats the particles as oblate or prolate ellipsoids. Although their physical shape is better described as a cylinder with hemispherical end caps, the results are sufficient in most cases. However, in cases where the shape of the particles has to be exactly modelled, the discrete dipole approximation (DDA) method[86] can be used alternatively. For clusters of arbitrary size and shape, the T-matrix method provides a more general approach.[65, 84, 85] The boundary conditions together with the linearity of Maxwell's equations lead to a linear relationship between the scattered and the incident field. The linear transformation between the two sets of coefficients is the so-called T-matrix. In general, the technique allows to compute numerical results for non-spherical particles.[65]

In any case, replacing a sphere with an ellipsoid considerably complicates the mathematical treatment. The approach Gans used in his work was that of the quasi-static or electrostatic approximation which will be presented in the following.[47, 65]

2.1.4.3 Spheres in the Electrostatic Approximation

The interaction of light with particles depends strongly on the particle properties like their size, shape and material. However, there are some general aspects regarding absorption and scattering of light by small particles. Small in this circumstances shall be understood in comparison to the wavelength. As a consequence, the particles in many cases may be considered as point-like objects.

Under the influence of an electromagnetic wave, the electrons in the metal particles can move while the positively charged ions of the metal grid are assumed to be immobile. The displacement of the electrons gives rise to polarization charges at the particle surface and consequently to a restoring force which determines the frequency of the system. Hence, the conduction electrons oscillate. Although all the electrons in the conduction-band participate in this process, the main effect takes place at the particle surface, therefore leading to the expression of the so-called surface-plasmon (SP). A schematic representation of this process is given in Figure 6.
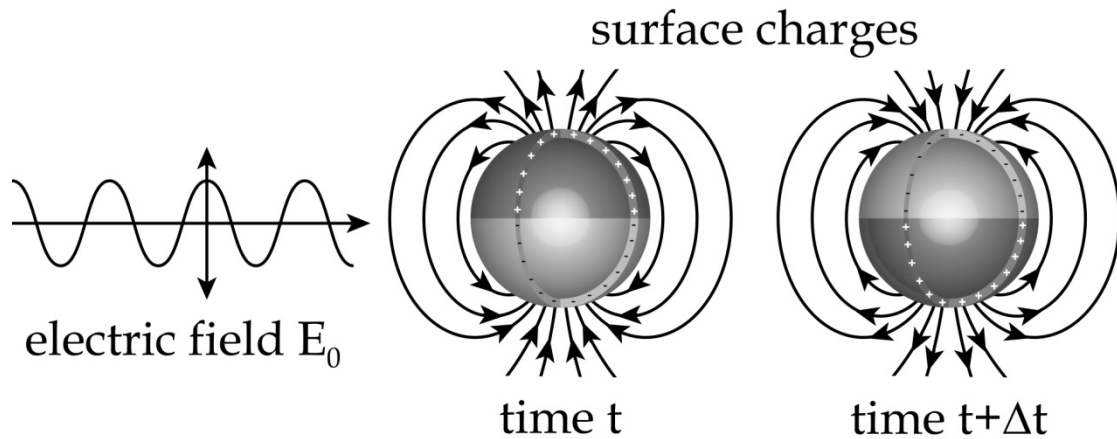
Figure 6: Schematic excitation of a dipolar surface-plasmon (SP) by an incident electric field $\mathbf{E}_0$. The free electrons oscillate under the excitation of the electric field and induce a polarization of the particle, mainly at the surface. The displacement results in a restoring force due to Coulomb interaction with the ion grid which is regarded as immobile.

2.1 Optical Properties of Gold Nanoparticles

However, since the physical dimensions of the particle might not always coincide with the area which interacts with light, the so-called cross-section C is another parameter to measure its "size". The extinction cross-section C_{ext} consists of the sum of the absorption and scattering cross-sections C_{abs} and C_{sca}[47]

$$C_{ext} = C_{abs} + C_{sca}. \tag{2.23}$$

In the electrostatic approximation, where a small sphere is embedded in a uniform and static electric field, the cross-sections can be described as:

$$C_{sca} = \frac{2\pi}{k^2} \sum_{l=1}^{\infty} (2n_p + 1)\left(|a_l|^2 + |b_l|^2\right) \text{ and} \tag{2.24}$$

$$C_{ext} = \frac{2\pi}{k^2} \sum_{l=1}^{\infty} (2n_p + 1)\mathbf{Re}\{a_l + b_l\} \tag{2.25}$$

with the wave vector k and the refractive index of the particle n_p. The scattering coefficients a_l and b_l are expressed with the aid of the Ricatti-Bessel functions $\psi_l(\rho) = \rho j_l(\rho)$ and $\xi_l(\rho) = \rho h_l^{(1)}(\rho)$:

$$a_l = \frac{m\psi_l(mx)\psi_l'(x) - \psi_l(x)\psi_l'(mx)}{m\psi_l(mx)\xi_l'(x) - \xi_l(x)\psi_l'(mx)} \text{ and} \tag{2.26}$$

$$b_l = \frac{\psi_l(mx)\psi_l'(x) - m\psi_l(x)\psi_l'(mx)}{\psi_l(mx)\xi_l'(x) - m\xi_l(x)\psi_l'(mx)} \tag{2.27}$$

where $m = n_p/n_m$ is the relative refractive index and $x = k\frac{d}{2} = \frac{\pi n_m d}{\lambda}$ is the size parameter (refractive index of the medium n_m, wavelength λ). The index l gives the order of the partial electric or magnetic wave, $l = 1$ corresponds to a dipolar field, $l = 2$ to a quadrupolar one and so on. Finally, the cross-sections result as:

$$C_{sca} = \frac{2\pi d^2 x^4}{3}\left|\frac{\varepsilon_p - \varepsilon_m}{\varepsilon_p + 2\varepsilon_m}\right|^2 \text{ and} \tag{2.28}$$

$$C_{ext} = \pi d^2 x \, \mathbf{Im}\left\{\frac{\varepsilon_p - \varepsilon_m}{\varepsilon_p + 2\varepsilon_m}\right\} \tag{2.29}$$

with the dielectric constant $\varepsilon_{p,m}$ of the particle and the medium, respectively.

Following eq. 2.28 and 2.29, for the case of $\varepsilon_p(\omega) = -2\varepsilon_m$, resonances result for the cross-sections C_i and consequently are to be expected in the particle spectra. Setting the cross-sections into relation with the real particle's cross-sectional area $A = \pi d^2/4$, projected onto a plane perpendicular to the incident light, one can calculate the efficiencies Q_i of the interaction between light and particle

$$Q_i = \frac{C_i}{A}$$

(2.30)

with $i = ext, abs, sca$. The absorption and scattering efficiencies $Q_{abs,sca}$ can be obtained in the electrostatic approximation as:[47]

$$Q_{abs} = 4x\,\mathbf{Im}\,\frac{\varepsilon_p - \varepsilon_m}{\varepsilon_p + 2\varepsilon_m} \text{ and } Q_{sca} = \frac{8}{3}x^4 \left| \frac{\varepsilon_p - \varepsilon_m}{\varepsilon_p + 2\varepsilon_m} \right|^2.$$

(2.31)

Depending on the polarizability α of the sphere, the incident field causes an induced dipole moment $\boldsymbol{\mu}$:

$$\boldsymbol{\mu} = \varepsilon_m \alpha \mathbf{E}_0, \ \alpha = \pi \frac{d^3}{2} \frac{\varepsilon_p - \varepsilon_m}{\varepsilon_p + 2\varepsilon_m}.$$

(2.32)

Thus, the particle acts as an ideal dipole of dipole moment $\boldsymbol{\mu}$.[65]

The electrostatic approximation does only hold for particles with sizes between 10 and 100 nm, since the field cannot be considered to be homogeneous any longer throughout the particle for larger sizes. In contrast, the field experiences a retardation across the particle which leads to so-called extrinsic size effects. As a consequence, the multipole modes come into play which lead to a red shift of the resonances expected from the simple condition $\varepsilon_p(\omega) = -2\varepsilon_m$.

2.1.4.4 Ellipsoids in the Electrostatic Approximation

In the case of an ellipsoid, the polarizability is anisotropic due to the anisotropic shape of the particle. Throughout this work, only prolate spheroids with two equal short axis ($a > b = c$), as sketched in Figure 7 were used.
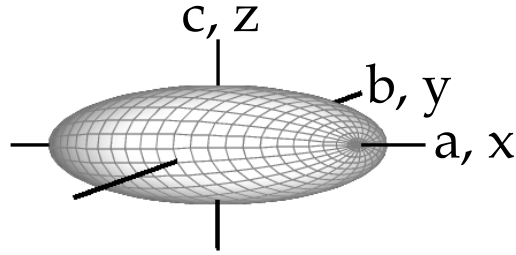
Figure 7:   Schematic of a prolate spheroid with a long semi axis *a* and two short but equal ones *b* and *c* ($a > b = c$). The three Cartesian axes are indicated as well.

The geometrical factors L_i for prolate spheroids with two equal short semi axes become:[47]

$$L_x = \frac{1-e^2}{e^2}\left(-1+\frac{1}{2e}\ln\frac{1+e}{1-e}\right) \text{ and } L_y = L_z = \frac{1-L_x}{2} \tag{2.33}$$

with the eccentricity $e = \sqrt{1-\frac{b^2}{a^2}}$.

Since the sum of the three shape dependent geometrical factors equals unity, $L = 1/3$ results for a spherical particle.

Although the real shape of gold nanorods is not resembled, for mathematical reasons they are usually modelled as prolate spheroids. In more precise calculations, they are approximated as cylinders with hemispherical end caps. However, in most cases, the results from the more simple approach are sufficient.

For the applied field being parallel to one of the Cartesian axes given by the particle's semi axes, the polarizability results to be:

$$\alpha_i = 4\pi abc \frac{\varepsilon_p - \varepsilon_m}{3\varepsilon_m + 3L_i\left(\varepsilon_p - \varepsilon_m\right)}. \tag{2.34}$$

2.1.5 Photoluminescence of Gold Nanoparticles

Photoluminescence (PL) from gold has been first reported by Mooradian in 1969.[13] In this study, a bulk sample was used, while PL has been reported later also from gold nanoparticles.[2-12] The luminescence from the small particles is much more efficient, while the underlying mechanisms appear to be rather similar and consequently, the observed spectra are pretty comparable.

After optical excitation of gold with either an argon laser ($\lambda = 488$, 514 nm) or a Hg lamp ($\lambda = 300$-400 nm), Mooradian found luminescence peaking around 530 nm, in the very energy range where absorption occurs. The radiative emission was explained as a recombination of conduction-band electrons below the Fermi-level with holes in the d-band. The observed quantum efficiency Φ for bulk gold was extremely weak with $\Phi_{bulk-Au} = 10^{-10}$ [13] (typical values for dye molecules are about nine orders of magnitude higher). Consequently, there have to be very efficient non-radiative relaxation channels since only one electron-hole pair out of 10^{10} undergoes radiative recombination. Examples of such alternative channels are Coulomb scattering or carrier-phonon scattering.[2] Since interband transitions hold responsible for the emission spectrum of gold (and similarly for other metals), the PL has been intensely studied to gain insight in the metal's band structure.[3, 4]

The first PL from gold nanoparticles was demonstrated for small nanospheres with sizes around or below 5 nm.[5] Although the observed spectral features slightly differed from those of bulk gold, the emission was attributed to the same underlying processes. Mainly, a strong blue shift in the luminescence to 440 nm accompanied with special absorbance features in the UV was found. In addition, a much stronger quantum efficiency of $\Phi_{Au-NP} = 10^{-4} - 10^{-5}$ was reported. This was attributed to an electrostatic enhancement mechanism as it is also observed in surface-enhanced Raman scattering (SERS). The corresponding values for an amplification of about five to six orders of magnitude are fairly consistent.[5]

2.1 Optical Properties of Gold Nanoparticles

A weak PL has been observed from larger spherical particles (d = 25 nm).[6] In this case, the emission spectra closely matched the absorption plasmon band. Therefore, the authors assumed the PL being due to the conversion of SPs rather than the recombination of electron-hole pairs.[6] However, the observed emission at 530 nm also perfectly matches the PL energy from bulk gold which might as well be more than pure coincidence. Another study of the PL of gold nanospheres was presented by Dulkeith and co-authors who found a quantum efficiency $\Phi_{Au-NP}=10^{-6}$ almost independent of the particle size (d = 2-30 nm).[2] In addition, perfect overlapping of the peak positions for the absorption and emission spectra were reported for all the particles. Because of this overlap, a strong influence of the SP is suggested in the publication. Since the excitation wavelength (λ = 375 nm) did not match the SP frequencies, the authors refrained from justifying the huge gain in PL of four orders of magnitude compared to the bulk gold with a local field enhancement from the (not even excited) SPs. However, they propose the non-radiative relaxation of d-band holes under the emission of plasmons which in turn cause the PL.[2] Therefore, the involvement of SPs in their model is rather indirect and independent from the primary excitation process since it consists of three steps. First, an electron-hole pair is formed which in a second step recombines and creates a SP. In the third step, the SP decays under emission of luminescent light. Moreover, for gold nanorods, a higher quantum efficiency of up to two orders of magnitude was suggested.[2]

Such a quantum efficiency of $\Phi_{Au-NR}=10^{-4}-10^{-3}$ from gold nanorods was indeed reported by Mohamed and coworkers where the emission wavelength maximum increased linearly with the particle length (b = 20 nm, R = 2, 2.6, 3.3, 4.3 and 5.4).[7] In addition, the Φ_{Au-NR} was found to linearly depend on the squared particle length. For an excitation wavelength in the range of the transversal plasmon band at 480 nm, the emission occurred from 548 to 588 nm. Since the longitudinal SP absorption is further red shifted, the observed emission cannot be assigned to this relaxation process. Therefore, the authors attributed it to the recombination of sp-electrons with holes in

the *d*-band, hence the very mechanism for the emission in bulk gold.[7] The same group also showed PL from longer gold nanorods together with a refined theoretical treatment. Although the emission from the longer particles is weaker, it does not totally vanish as it seems to be the case for spherical particles. This effect is attributed to a coupling between the longitudinal SP and the interband transition upon excitation at 480 nm. However, the red shift of the emission wavelength was found to come to a stop around 600 nm at a certain aspect ratio.[8]

Comparing the PL from gold nanospheres (*d* = 25 nm) and gold nanorods (*R* = 1.8 and 2.7), Varnavski *et al.* found that the quantum efficiency of the nanorods exceeded the one of spherical particles by a factor of up to 10.[9, 10] The authors found good agreement of this value with the model of plasmon-mediated field enhancement in metal nanostructures. In addition, the PL decayed very fast (≤ 50 fs) for all investigated particles and was depolarized. Since the spectra also did not change with the excitation energy, the visible PL was again attributed to electron-hole recombination.[9, 10] The observed enhanced emission in gold nanoparticles could be satisfactorily explained with the local field enhancement theory.[9, 10]

Two-photon induced PL of a single gold nanorod has been observed in a scanning near-field optical microscope (SNOM). The spectrum featured two emission maxima near 550 and 650 nm.[11, 12] Being close to the theoretically predicted energies for the recombination of electron-hole pairs from states close to the X- and L-symmetry points in the first Brillouin zone, the authors attributed the optical transitions to be due to this process. The spectra of individual particles were similar regarding peak positions but differed in the relative intensities of the two observed bands. These variations were explained with differences in the local density of states. Since they should be correlated to the SP modes of the respective nanoparticles, they result directly to be mainly a function of particle size and shape.[11, 12]

In general, the different observations of PL in bulk gold as well as gold nanoparticles have been mainly attributed to the recombination of conduction-band

2.1 Optical Properties of Gold Nanoparticles

electrons with holes in the *d*-band close to the X- and L-symmetry points in the Brillouin zone, since the density of states at these points is especially high. Therefore, the PL is closely related to the metal's band structure and should not primarily depend on the particle's shape and size. This is in overall accordance with the spectra from the literature which show no or only weak dependence on the SP resonances. However, coupling to the SP may occur nevertheless in terms of field enhancement effects, as can be recognized from the increased quantum efficiencies for gold nanoparticles which are up to six[2] and seven[7] orders of magnitude higher for nano-spheres and nanorods compared to bulk gold[13], respectively. Additionally, the coupling to the plasmon resonances might also induce changes in the observed band intensities.[11, 12] Nevertheless, for gold nanorods a dependency of the emission wavelength on the aspect ratio has been observed under certain circumstances.[7, 8] Yet, the red shift occurs at different wavelengths as in the absorption spectrum.[7, 8] An interesting explanation might be the one given in reference [2], involving the indirect excitation of SPs due to the recombination of electron-hole pairs. Although the PL of gold nanoparticles has attracted some attention over the last years, it appears to be fruitful to study the topic in more detail. In particular, the excitation wavelength might play an important role in this process as well as the shape and size of the individual particle.

3 Experimental Methods

3.1 Confocal Microscopy

Light microscopy techniques provide insight in the fascinating world of the micro- and nanocosmos which is not directly accessible to the human eye. In conventional wide-field microscopy, the entire specimen is illuminated and the magnified image can be directly recognized by eye or projected onto a screen, film or similar image capturing device. In confocal microscopy, however, the sample is illuminated with tightly focused light. Both the illumination and detection occurs point by point and consequently, the image has to be composed computationally. A pinhole in the detection path blocks light and blur from out-of-focus regions providing a better optical resolution and higher image contrast. A wealth of experimental configurations can be realized. Here, a sample-scanning microscope in reflection mode was used, as schematically shown in Figure 8. The same objective both focuses the light onto the sample and to collects the light for detection.
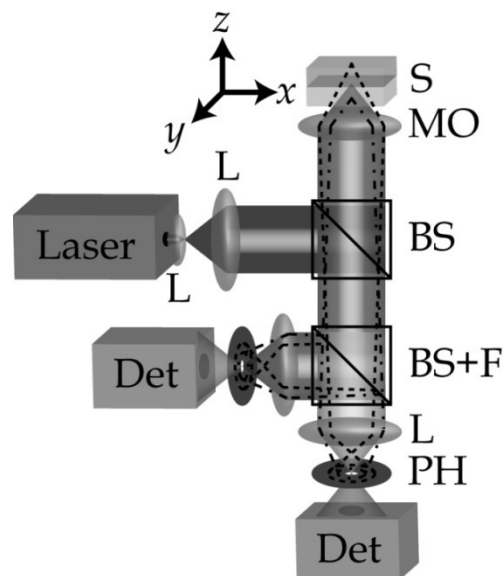
Figure 8:   Schematic of a confocal setup in reflection mode as used here. The light from the laser which acts as a point-like excitation source is collimated by a lens (L) and sent to the sample (S) by a beam splitter (BS). Focussing is achieved by a microscope objective (MO) which also collects the light for detection. A second BS allows detection on two channels in combination with appropriate filters (F). Pinholes (PHs) in front of the detectors (Dets) block out-of-focus light (as indicated by the dotted lines) to enable confocal imaging. Scanning of the sample is provided by moving the sample with a scanning stage.

3.1 Confocal Microscopy

A laser is used to illuminate the sample and acts as a point-like source. After collimation with a telescope (consisting of two lenses L), a beam splitter (BS) or dichroic mirror directs the light to the microscope objective (MO) to focus on the sample (S). The same objective collects the light for detection. Further splitting of the light enables two- or multi-channel detection (Det) in combination with appropriate filters (F). Blocking out-of-focus light with a pinhole (PH) in the detection path allows for confocal imaging. A variety of detectors can be used, *e.g.* photomultiplier tubes (PMT), (Avalanche) photo diodes ((A)PD) or charged coupled device (CCD) cameras.

Due to the use of lasers as excitation sources in confocal microscopy, there are various possibilities at hand to exploit the magnificent characteristics of laser radiation. Almost any imaginable state of polarization can be realized nowadays and laser pulses of different shape and ever shorter time duration have been especially useful for spectroscopic experiments. In this work, a special class of higher order laser modes (HOLMs) with particular polarization properties, so-called radially and azimuthally polarized doughnut modes (RPDM/APDM) have been used in combination with confocal microscopy. Their polarization properties upon tight focusing make these modes extremely appealing for microscopic applications as they offer access to information which is usually hidden below the diffraction limit. In more detail, they offer different orientations of the polarization. For the azimuthally polarized mode, the electric field polarization solely lies in the sample plane, while the radially polarized mode also offers a strong component which is polarized along the optical axis. Consequently, there is a grand variety of experiments one can think of. As an example, the orientation of single molecules or nanoparticles can be determined with high accuracy or differently shaped nanoparticles can be distinguished.[35, 36, 39, 87]

The size of the excitation volume in focus is referred to as the point spread function (PSF), describing the intensity pattern of a point-like object observed in the focal plane for a circular aperture. In the focal plane, it results as a circular spot with concentric surrounding rings, the Airy disk of diameter Δx_{Airy}:[88, 89]

$$\Delta x_{Airy} = 1.22 \frac{\lambda}{n \cdot \sin \alpha} = 1.22 \frac{\lambda}{NA} \qquad (3.35)$$

with the wavelength λ, the refractive index n, the half-angle of the angular aperture α and the numerical aperture NA. In confocal microscopy, the image formation is determined by the PSFs of the illumination system and the detection path. In reflection mode, the same objective is used for both illumination and collection of the detected light. If the size of the pinhole is chosen appropriately, the PSF of most confocal systems therefore results as the squared PSF of the microscope objective and the lateral resolution Δx_{conf} as:[88, 89]

$$\Delta x_{conf} = 0.88 \frac{\lambda}{n \cdot \sin \alpha} = 0.88 \frac{\lambda}{NA} . \qquad (3.36)$$

An important benefit of confocal microscopy is the increased axial resolution Δz_{conf}:

$$\Delta z_{conf} = 1.5 \frac{\lambda}{n \cdot \sin^2 \alpha} = 1.5 \frac{n \cdot \lambda}{NA^2} . \qquad (3.37)$$

For transparent samples, images from different planes can thus be acquired allowing to measure 3D data stacks of the specimen which can be assembled computationally to form a 3D image. This non-invasive way to examine transparent samples has made confocal microscopy an extremely powerful tool for life sciences. In many cases, the sample is stained with fluorescent dyes allowing *e.g.* to detect specific tissue in biological samples. Besides applications in life sciences, due to the high sensitivity of confocal microscopy, single nanoemitters or –scatterers like molecules, quantum dots or nanoparticles can be imaged. The combination with sensitive spectroscopic detection opens up a variety of opportunities to study their optical properties in great detail.

3.1 Confocal Microscopy

Besides numerical values for the size of the PSF, two point-like objects only appear separated when their distance is large enough to discern a dip in-between the two peaks. Such a separation is arbitrary by definition, but a widely accepted criterion was suggested by Rayleigh: the distance of two intensity maxima has to be at least equal to the distance from one maximum to the first minimum in the diffraction pattern.[62] This standard results in a dip of about 26 %.[90] One could argue that a smaller indentation between two maxima would be already sufficient, however, in reality, noise is always an issue. Additionally, the two objects might not be of equal intensity. In the end, the Rayleigh criterion should not be considered to be set in stone but it has proven to be very useful as a first reference point. Generally, it is all about image contrast. Confocal microscopy offers enhanced contrast by blocking out-of-focus light with the confocal pinhole. The degree of blocking is chosen by the aperture size. In addition, the side maxima in the confocal PSF (see eq. 3.36) are suppressed as compared to wide-field microscopy, considerably improving image contrast. Consequently, especially dim objects can be better resolved even when close to bright signals.

Considerable efforts have been undertaken to improve or circumvent the optical diffraction limit and to provide optical alternatives to high resolution techniques like electron microscopy (EM), *e.g.* scanning near-field optical microscopy (SNOM)[15, 16], stimulated emission depletion microscopy (STED)[26], photoactivated localization microscopy (PALM) or stochastic optical reconstruction microscopy (STORM)[91]. However, these methods are highly sophisticated and elaborated. Therefore, it would be appreciable to have access to information hidden below the resolution limit without having to break or circumvent it, as will be shown throughout this work.

3.2 Confocal Scattering Microscopy with Doughnut Modes

The implementation of higher order laser modes, namely APDMs and RPDMs, opens up a variety of possibilities for microscopic applications of which a few shall be introduced in this chapter.

Individual gold nanoparticles down to a diameter of 10 nm can be easily detected with confocal microscopy by their elastically scattered light.[39, 87] The special polarization properties of the DMs further allow to distinguish particles of different shapes (nanospheres, –rods and –triangles).[36, 39, 41, 87] In the case of metal nanorods, the particles' orientations are directly visualized in the image and can be precisely determined (with an accuracy of about 1 °).[35] Moreover, the signal sign and the signal-to-background ratio are highly sensitive to the refractive properties at the sample interface.[40] Thus, the dielectric interface itself can be sensed. In liquid environments, also the spontaneous rotation of an individual nanorod can be followed even if not combined with a lateral translation of the particle. Finally, the technique allows to detect the full 3D orientation of particles embedded in a polymer film with high accuracy.[38] Since gold nanoparticles also show a strong PL, alternatively to the detection of the elastically scattered light, also the red shifted emission can be used for the image acquisition.[38] Due to the different image formation process, the information regarding the sample interface varies. However, the information about the particle itself is greatly unaffected. The shape of the scattering and luminescence pattern are essentially the same and consequently, the information regarding shape and orientation are equivalently provided.

3.2 Confocal Scattering Microscopy with Doughnut Modes

3.2.1 Image Acquisition Process

In the scattering mode, the light directly reflected at the sample interface combines with the light scattered from the particles:[36]

$$I_{\mathbf{det}} \propto \left| \mathbf{E}_{ref} + \mathbf{E}_{sca} \right|^2 = \left| \mathbf{E}_{ref} \right|^2 + \left| \mathbf{E}_{sca} \right|^2 + 2 \left| \mathbf{E}_{ref} \right| \left| \mathbf{E}_{sca} \right| \cos \varphi \qquad (3.38)$$

with the detected intensity $I_{\mathbf{det}}$, the reflected and scattered fields $\mathbf{E}_{ref}$ and $\mathbf{E}_{sca}$ and the phase relation φ between the two fields. The first term on the right side of eq. 3.38, $|\mathbf{E}_{ref}|^2$ represents the background (BG) intensity caused by reflection at the sample interface. The second term corresponds to the light which the particles directly scatter. $|\mathbf{E}_{sca}|^2$ scales with the squared particle volume, thus, for nanoparticles as treated here, the signal might be too weak for direct detection. The last term of eq. 3.38, however, describes the interference of the two involved fields and allows for detection of single particles even with weak scattering signals. The sign of the interference and hence of the image contrast is determined by the phase relation φ, therefore, the image contrast can be either negative (dark signal on brighter BG) or positive (bright signal on darker BG). As can be recognized throughout this work, the experimental image contrast results to be negative in most cases. Special optical properties at the sample interface, however, sparsely lead to a positive image contrast. Depending on the dielectric interface, the interplay of the three terms in eq. 3.38 changes. For a specific nanoparticle, interface and excitation wavelength, more complex approaches can be necessary (see *e.g.* chapter 5.1, p. 101). In general, the phase relation φ depends on the involved SPs, *i.e.* on the material, size and shape of the particles. In addition, it is influenced by the optical properties of the interface and the objective's *NA*. The impact of the dielectric interface is so strong that even slight variations in the refractive index n_m of the embedding medium can switch the sign of the image contrast.

Alternatively to detecting the elastically scattered light, a notch filter can be inserted in the detection path to remove light of the laser wavelength. The strong luminescence of gold nanoparticles allows to detect single particles in the PL mode as well. Naturally, the observed image contrast is always positive.

3.2.2 Determination of the 2D Orientation of Gold Nanorods

The polarizability of gold nanorods is highly anisotropic due to the splitting of the plasmon resonance in a longitudinal and a transversal mode, corresponding to electron oscillations along the length a and the width b of the particle, respectively. The transversal plasmon resonance is located around 520 nm while the longitudinal one is red shifted. With increasing particle length, the longitudinal plasmon mode shifts to longer wavelengths. Surprisingly, the absolute particle size only slightly influences the extinction spectra or the resonance of the SPs. The key parameter is the aspect ratio R, that is the ratio of the particle's length over its width.[92-94] Hence, excitation of the particles with red light at 633 nm mainly concerns the longitudinal plasmon resonance. This directed polarization induces a dipole moment which mimics the orientation of the long particle axis. The interaction between light and a dipole moment critically depends on their relative orientation. For parallel orientation, the interaction is maximized while a deviation from this optimal alignment reduces the efficiency, finally ceasing for a perpendicular orientation.

Upon excitation with azimuthally or radially polarized light, any direction of excitation polarization in the xy-plane is provided in focus. For an APDM, the whole polarization lies in the sample plane. When a RPDM is focused with an objective of high $NA > 1$, however, a considerable amount of the polarization is oriented parallel to the optical axis, with a weaker transversal component which is polarized in the xy-plane. At 633 nm, the interaction between the excitation light and a single gold nanorod is now governed by the orientation of the induced dipole moment and hence, the particle's long axis. Therefore, only the part of the excitation light providing a suitable polarization direction interacts with the particle producing a characteristic two-lobed pattern with its orientation directly visualizing the 2D alignment of the particle. This has been verified by *in situ* topography measurements with atomic force microscopy (AFM, see Figure 9).[36, 41] The long particle axis has indeed been found to coincide with the orientation of the acquired scattering pattern.[36, 41]

3.2 Confocal Scattering Microscopy with Doughnut Modes

 An experimental scattering pattern of a single gold nanorod upon excitation with an APDM at 633 nm is shown in Figure 9 a, with the corresponding *in situ* AFM data in b.
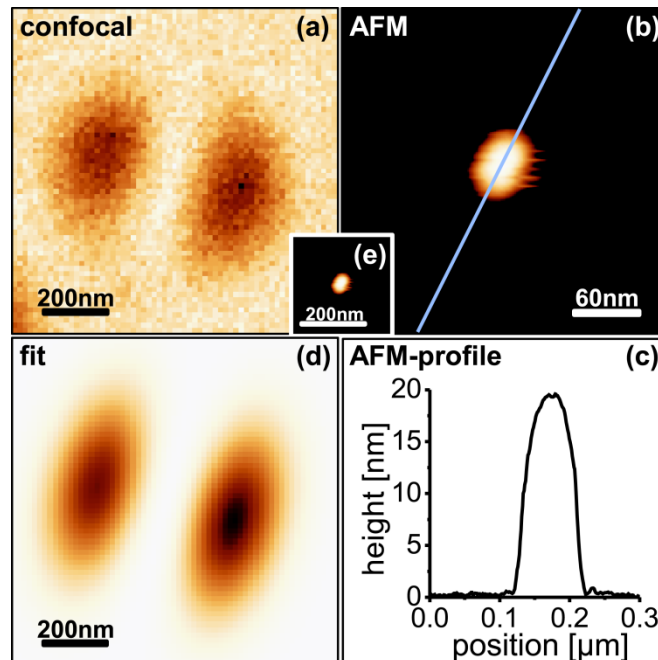
Figure 9: (a) Confocal scattering image of a single gold nanorod (APDM at 633 nm) and (b) *in situ* AFM measurement with (c) the corresponding height profile as indicated by the line. (d) Shows a reproduction of the experimental scattering image with a fit function.[35] The characteristic two-lobed scattering pattern directly maps the particle's orientation. For an APDM, the line connecting the lobes is oriented perpendicularly to the long axis. (e) Shows the AFM data in scale with the confocal image. Similar patterns are found upon excitation with a RPDM but turned by 90 °. Figure taken from reference [41].

The line connecting the two lobes of the scattering patterns is found to be perpendicular to the rod's long axis. The AFM cross-section taken along the line shown in Figure 9 c gives the particle's height (or short axis) with about 20 nm in good agreement with values from the literature.[95] Figure 9 d presents a reproduction of the acquired pattern with a fit algorithm[4] which is used to automatically extract the orientational information.[35] In Figure 9 e, the AFM data is shown in scale with the confocal image in a. This underscores that the diffraction

---

[4] The 2D fit algorithm was developed by Dr. Antonio Virgilio Failla using a Matlab® code.

limited pattern reveals sub-resolution information from the nanoscale. Similar scattering patterns are found upon excitation with a RPDM. The two lobes are turned by 90 ° compared to excitation with an APDM because of the different polarization properties of the two modes. Hence, the connecting line is oriented in parallel with the long particle axis. In any case, the orientation of individual nanorods is directly visualized and can be recognized from a single image. For a precise analysis, the resulting patterns can be fitted with a 2D model function to extract the orientation with an accuracy of about 1 °.[35] Each lobe is fitted separately with a Gaussian function to allow the reproduction of asymmetric patterns. The whole pattern is enveloped by a third function (first order Hermite-Gauß), centered on the pattern's median point.[35] Additionally, the particles can be localized with sub-pixel precision. The optical pattern is mimicked with a mathematical function not correctly describing it, comparable to the approach to determine the accurate position of nanoobjects by fitting the PSF with a Gaussian function.[96] For particles in liquid medium, spontaneous rotations can be followed, as long as the rotation is slower than the timescale of the method.[41] While imaging particles in solution, from time to time, new particles appeared on the glass surface. This is probably due to particles slowly "falling down" from the solution. Such processes can also be monitored.[41]

Since gold nanoparticles not only strongly scatter the light but also show a solid and stable PL, the spectrally red shifted light can be detected alternatively. The shape of the two-lobed patterns stays the same and the orientational information can be extracted from the PL data as well. As an example, Figure 10 shows PL confocal images of the same set of individual gold nanorods upon excitation with both azimuthally and radially polarized light at 633 nm. As in the scattering mode, the characteristic two-lobed patterns are obtained. As revealed from *in situ* topography measurements (cf. Figure 9), the long particle axis is oriented perpendicularly to the line connecting the lobes when an APDM is used for excitation. For the RPDM, the long particle axis connects the lobes, that is, the pattern is turned by 90 ° compared to the case of the APDM.

3.2 Confocal Scattering Microscopy with Doughnut Modes

In Figure 10 c and d, close-ups of the areas marked by the grey dashed lines are shown, which have been acquired as separate images. The particle in the upper left corner in d spontaneously rotated during the image acquisition (the particles are spin coated on the glass substrate and rarely overcome the dielectric forces which normally immobilize them). Because of the spontaneous rotation by almost 90 °, the patterns of this particle agree in orientation for both excitation modes while all the other patterns are rotated as expected.
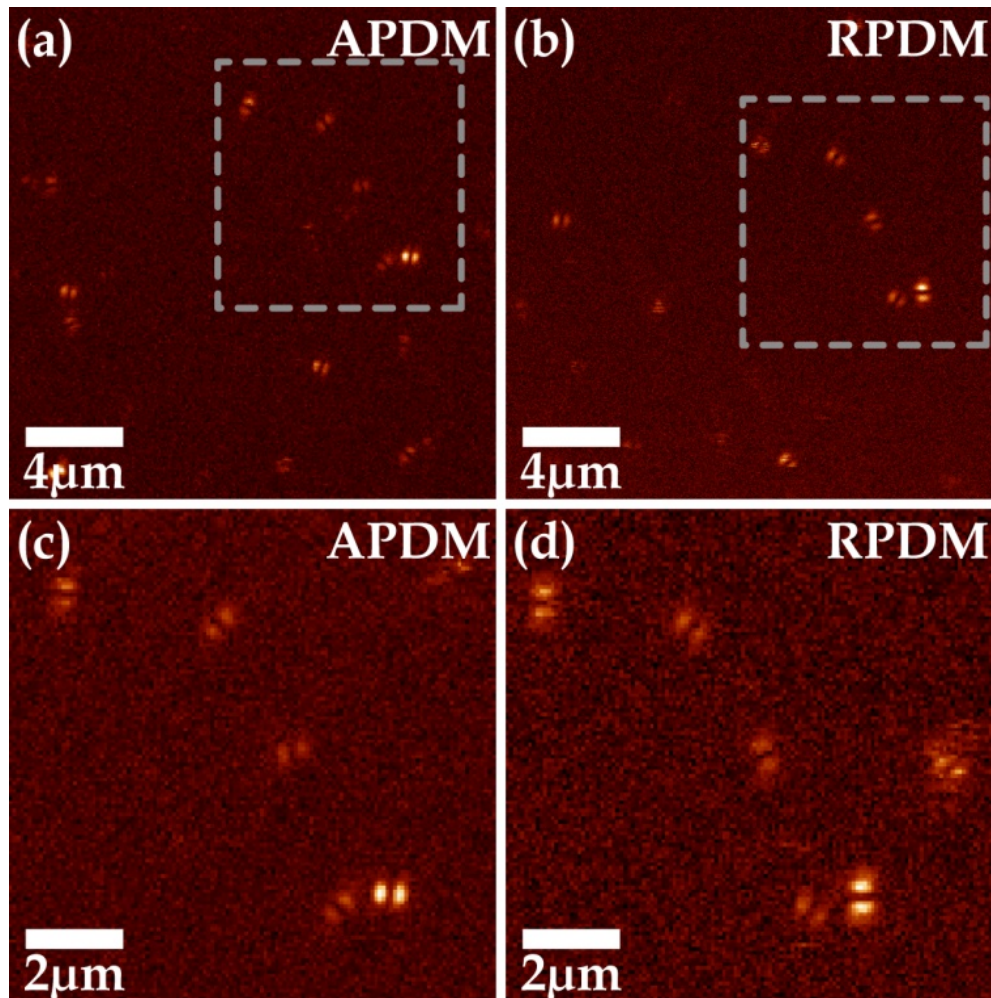
Figure 10: Confocal PL images of the same set of gold nanorods: (a, c) APDM, (b, d) RPDM at 633 nm. Two-lobed patterns revealing the particles' orientations are obtained, while the patterns are turned by 90 ° for the two modes. *In situ* AFM measurements confirm that the long particle axis runs perpendicularly (parallel) to the line connecting the lobes for the APDM (RPDM). (c, d) Close-ups from the areas marked in grey, acquired as separate images. The particle in the upper left corner in (d) spontaneously rotated whilst acquiring the images.

Both the scattering and luminescence mode can be equivalently used to determine the orientation of individual particles. A benefit of detecting the PL light is that the images are almost BG free and the signal-to-noise ratio (SNR) is higher. Compared to the scattering mode, higher laser intensities have to be used. As long as the sample solely consists of gold particles, however, this is hardly an issue. Because the scattering mode is extremely sensitive to the optical properties of the sample interface,[40] the particles can be used to sense this interface. On the other hand, the signal appears to be less dependent on the interface and the direct environment in the PL mode, which can be favourable when the particle properties are of main interest, especially regarding optically inhomogeneous samples.

3.3 Tip-Enhanced Near-Field Optical Microscopy

Scanning near-field optical microscopy (SNOM) is a powerful technique to reach an optical resolution well beyond the diffraction limit. Since its invention in the 1980s,[97, 98] it has found wide application in different fields of science. The early works used an extremely small aperture to realize a resolution in the order of a few tens of nanometres.[97, 98] However, the resolution of this technique is somehow limited since the transmitted light intensity has to be strong enough for detection and consequently, the aperture cannot be reduced infinitely. Thus, the aperture size is confined within tens of nanometres – and therewith is the resolution. Another approach uses sharp metal tips where plasmon resonances in these tips are excited with strong longitudinally polarized electromagnetic fields. Therefore, the technique is referred to as tip-enhanced near-field optical microscopy (TENOM) or apertureless SNOM. With the resolution essentially depending on the size of the tip-apex, values down to 10 nm can be reached.[15, 16] In this work, electrochemically etched gold tips were used under illumination at 633 nm. An oil-immersion objective ($NA = 1.25$) served both for excitation and detection. For a RPDM, the focal field thus includes a longitudinal component, *i.e.* part of the light is polarized along the tip-axis. When the sharp metal tip is brought into the focus, surface-plasmons (SPs) are excited therein and the metal tip hence acts as a small light source. In addition, different enhancement effects can occur at the presence of a nanometre sized metal tip. One is the lightning rod effect, which happens at any pointed or defined structure as long as the curvature is smaller than the wavelength and enhances the electric field due to a confinement of the field lines. In addition, the electric field can be enhanced through SPs at certain wavelengths. Finally, the tip also acts as an antenna where the enhancement strongly depends on its shape. All these enhancement effects strongly depend on the tip's metal, its shape and size, and especially on the characteristics of the tip-apex.[15, 16, 99] Although this enhancement often allows to observe near-field effects, one should keep in mind that a huge far-field background is also detected when the near-field microscope is based on a confocal setup.

In addition to the optical information, the topography is simultaneously acquired during scanning the tip over the sample. The tip-sample distance is typically kept within a few nanometres, and therefore, the technique is basically limited to the study of surfaces. In principle, different feedback mechanisms are possible, but in this work, shear-force was used to control the z position as it is frequently encountered in TENOM. The shear-force feedback mechanism is different than the ones commonly used in AFM, hence the data is not directly comparable, but very similar. The image contrast is not only depending on the tip shape and therefore, it is not only AFM data together with optical information, but the acquired data is more complex. Since the tip is not in direct contact with the sample but held at a close but unknown distance, it is not possible to determine the absolute tip-sample displacement. A change in the z position, however, can be precisely determined.

In many cases, phenomena such as tip-enhanced luminescence or fluorescence (TEF) or tip-enhanced Raman scattering (TERS)[100, 101] can be observed, which promise to drastically increase the sensitivity and detection limit in spectroscopy. The field enhancement is normally given comparing the field with and without the tip in focus. The excitation rate enhancement scales quadratically with the field enhancement due to the Purcell effect[102] and can be described with Fermi's golden rule in the weak coupling range.[99] For the case of Raman scattering, both the excitation and radiation have to be taken into account for the enhancement and consequently, the product of the two enters the equation. Hence, the signal enhancement scales with the fourth power of the field enhancement, as long as the enhancement of the tip does not noticeably depend on the concerned wavelengths.[103] In the more general case of SERS, the highest enhancement factors are found for particle aggregates - up to 11 orders of magnitude have been predicted under fortunate geometrical conditions[104]. More complex enhancement mechanisms might be involved than in the case of a sharp metal tip since the particle surface and inter-particle spacing also have to be considered. For fluorescence enhancement, the energy transfer between molecules and metal interfaces is relatively well

understood,[105] which is not necessarily the case for metal particles and tips, or more generally speaking, nanometre sized objects.[106-122] Two counteracting processes which quench and enhance the fluorescence and strongly depend on different parameters have to be taken into account. One crucial parameter is the distance between the metal object and the molecule, but also the relative orientation plays a key role. Excitation wavelength, the spectral properties of the molecule, the SPRs of the metal structure and consequently its size and material are important as well.[105, 106, 111, 112] One should also keep in mind that the particle induced field enhancement can substantially influence the emission, both spatially and spectrally. Since the selection rules might change and standard dipole approximations not necessarily hold anymore, the near-field spectra can considerably vary from their far-field counterparts.[123-125]

3.4 Experimental Setup

3.4.1 Confocal Setup

In the confocal scanning microscope, a laser source (HeNe at 633 nm) is used for excitation of the sample. A schematic of the home-built experimental setup[87] is shown in Figure 11. The linearly polarized Gaussian mode (LPGM) provided from the laser source passes through a mode converter (MC) which generates the DMs (APDM or RPDM). The main part of the MC is a $\lambda/2$ wave plate (WP) consisting of four quadrants. In each quadrant, the incoming polarization is rotated appropriately to generate either radially or azimuthally polarized light. For mode cleaning, a spatial filter consisting of two lenses (L) and a pinhole (PH) is implemented. Wavelength cleaning is achieved with a laser line filter (LLF). The non-polarizing beam splitter (BS) directs the excitation light to the microscope objective (MO, oil-immersion CP-Achromat 100x, *NA* = 1.25, Carl Zeiss AG, Jena, Germany) which focuses the light on the sample (S). Raster scanning is provided by a *xy*-scanning stage (SC, P-517.3CL, PhysikInstrumente, Karlsruhe, Germany). The same objective is used to collect the light. For detection, either an avalanche photodiode (APD, SPCM-AQR-14, Perkin Elmer, Waltham/MA, USA) or a charge coupled device (CCD) camera in

combination with a spectrometer (SP) was utilized. A flip mirror (FM) allows to switch between the two detectors. Either the elastically scattered light can be detected (scattering mode) or a notch filter (NF) can be inserted in the detection path for exclusive detection of the luminescent light (fluorescence mode). Alternatively, two APDs can be used for parallel detection of both the scattered and luminescent light. To monitor the manual movement of the sample into the focus with a stepper motor, a mirror can be inserted in the optical path to reflect the light into an eyepiece (see Figure 11).
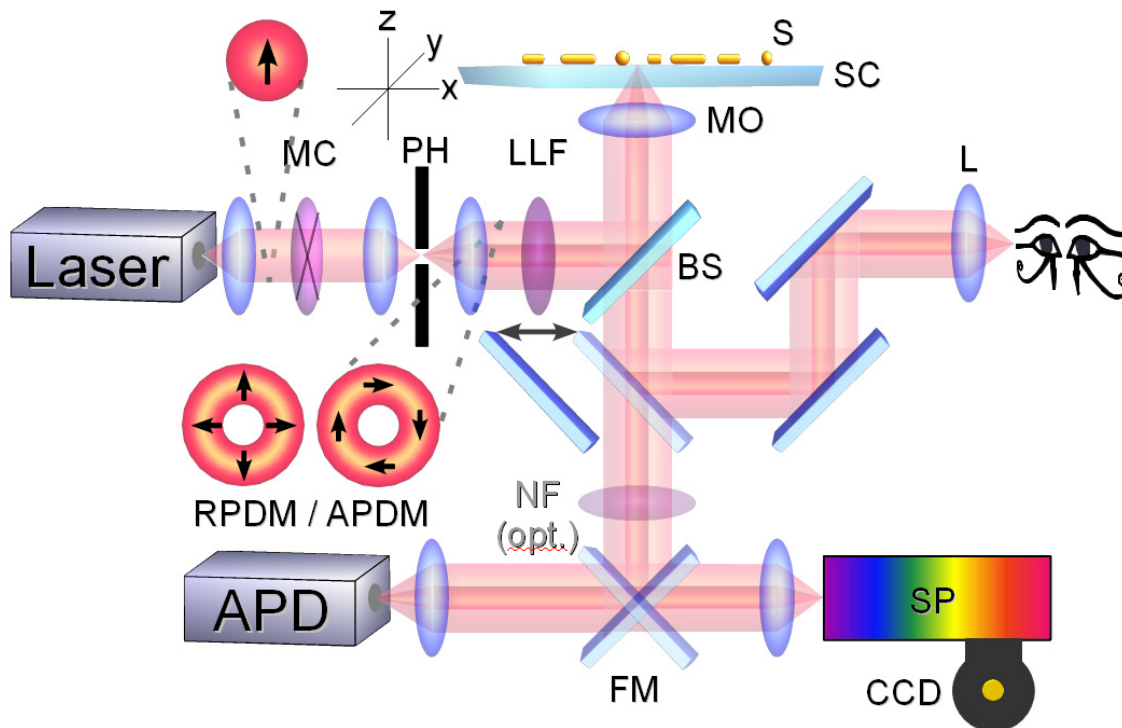
Figure 11: Schematic of the home-built experimental setup of the confocal laser scanning microscope. The mode converter (MC) transforms the linearly polarized Gaussian mode into a RPDM/APDM. The microscope objective (MO) both illuminates the sample and collects the light for detection on an avalanche photodiode (APD) or on a CCD camera after passing through a spectrometer (SP). PH: pinhole, LLF: laser line filter, BS: beam splitter, SC: scanning stage, S: sample, L: lens, NF: notch filter (optional), FM: flip mirror.

For data analysis and visualization from the home-built microscope as well as for AFM data, the freely available software WSxM[126, 127] proved to be very useful.

3.4.2 Experimental Generation of Doughnut Modes

Various experimental techniques have been developed to produce DMs of different polarization. Here, only radial and azimuthal polarization will be considered because of their significant importance regarding this thesis. Many different methods have been published to produce a DM with appropriate polarization.[34, 51, 59, 63, 128-150] Here, for convenience, only the applied strategy shall be introduced.

DMs have been created using a segmented $\lambda/2$ wave plate (WP).[59, 144] In this work, a four-segment WP rotates the polarization of the linearly polarized Gaussian mode (LPGM) selectively in each quadrant to create an almost radially or azimuthally polarized mode (see Figure 12).[59, 87]
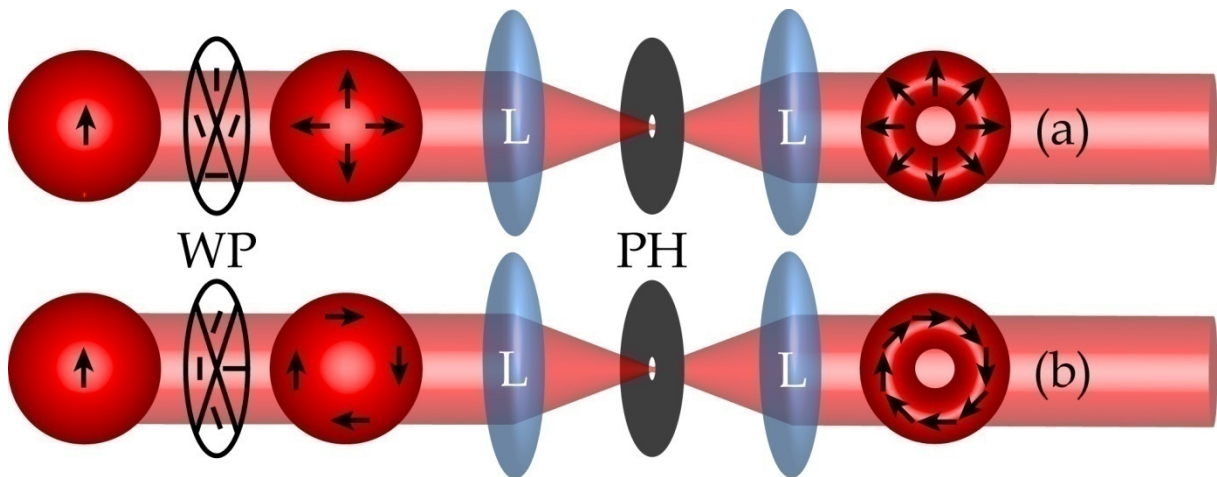
Figure 12: Schematic of the experimental realization of the mode conversion (MC) setup with a segmented $\lambda/2$ wave plate (WP). The linearly polarized Gaussian mode (LPGM) passes through the segmented WP which locally turns the polarization of the beam. After spatial filtering through a pinhole (PH) mediated with two lenses (L), either the radially (a) or azimuthally (b) polarized doughnut mode (RPDM/APDM) results, depending on the orientation of the WP. The arrows indicate the orientation of the polarization vectors in the beam cross-section.

Turning the WP by 90° allows to switch from one mode to the other. Additional mode-cleaning is achieved with a spatial filter consisting of two lenses (L) and a pinhole (PH).[16] The mode-cleaning is necessary to obtain a doughnut shape in the beam cross-section which is otherwise ruined by higher order contributions and disturbances introduced mainly by reflection from the bonding areas of the WP. A slightly higher mode quality can be achieved with a 8-sector $\lambda/2$ WP.[144]

3.4.3 *In situ* AFM Measurements

In order to support the confocal data with *in situ* AFM measurements, a commercial AFM (easyScan 2, Nanosurf AG, Liestal, Switzerland) can be operated directly on top of the optical microscope. To align the AFM in focus, it is supported by a home-built holder which can be moved in the sample plane with piezo actuators. With the AFM probe in focus, topographic information can be obtained from the same area as the optical data. For convenience, the scanning directions of the optical setup and the AFM are set to be approximately parallel, although perfect alignment is difficult since the scanning is not synchronized. However, comparing larger scan areas in both imaging modes, relative rotations can be accounted for. In principle, the acquired data could be similarly obtained with the near-field head (see chapter 3.4.4, p. 47). However, as long as only the topography is of interest, an AFM is often advantageous. The main reason is that AFM probes are commercially available and thus they provide guaranteed high quality both in terms of sharpness and symmetry in combination with higher robustness since silicon probes are not nearly as delicate as gold tips. In addition, for the AFM employed in this experiments, the same sample area can be quickly readdressed after changing the tip since its position is precisely determined.

3.4.4 Near-Field Setup

For near-field measurements, the same setup was used as for the confocal experiments. A home-built near-field head is attached to the microscope for these measurements. It consists of two assembled parts, one of which can be moved over the sample in x and y direction while the other holds the sharp metal tip. In the following, the first one will be called (near-field) head for convenience. The second one is used to finely move the tip in x, y and z direction and will thus be revered to as a slider. The whole device is sketched in Figure 13. The movement over the sample is necessary for precise alignment of the tip in focus. The first coarse alignment is realized with shear piezo stacks which are manually controlled while the head itself moves on ruby spheres.
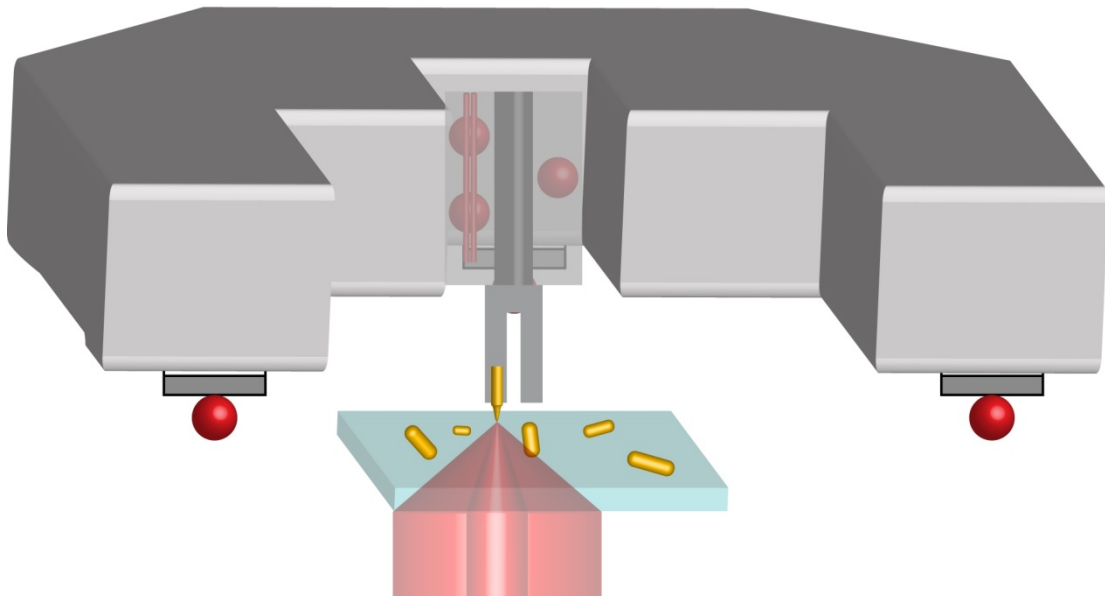
Figure 13: Schematic (not to scale) of the near-field head and the attached slider on a sample of gold nanorods. A sharp gold tip attached to a quartz tuning fork is raster scanned over the sample. To control the close distance between tip and sample, a shear-force feedback mechanisms is used. The whole device can be moved in x and y direction with piezo elements while the tip can be adjusted in x, y and z direction via piezo control as well. The gold probe is brought into the focus of a RPDM to excite surface-plasmons along the tip-axis.

The sharp gold tip is glued to a quartz tuning fork. The tuning fork is excited close to its resonance with a piezo tube which is enclosed in a ceramic housing. This whole device can be moved in x, y and z direction, again using shear piezos. Two ruby

spheres allow directed sliding between two ruby cylinders while a third sphere provides stability (see Figure 13). To prevent the whole slider to slip due to gravity, it is held with a magnet mounted on a screw allowing to adjust the restoring force.

During scanning, the probe-sample distance has to be carefully controlled in the nanometre range. In this work, a shear-force feedback was used for this purpose. The probe is mounted on a tuning fork which oscillates close to its resonance frequency. As soon as the probe comes close to the sample, this frequency changes because of on-setting interaction forces between the probe and the sample, the so-called shear-forces. Under ambient conditions, this effect is generally assigned to a surface humidity layer on the sample, but since shear-force can also be applied in high vacuum, different interaction mechanisms have to be involved as well.[16] Regardless of the exact mechanisms involved, the occurring forces sensitively depend on the probe-sample separation and therefore the gap can be precisely stabilized via feedback-control. At first glance, this seems to be rather comparable to AFM, however, different feedback mechanisms are usually involved. Another aspect is that in AFM, the force between probe and sample is the main topic of interest while it is used as an auxiliary signal in SNOM. As a consequence, one has to be cautious with artefacts which can be easily introduced when the probe-sample distance is changed by the feedback mechanisms. Since the near-field optical signal also sensitively depends on this distance, such variations might lead to the introduction of artificial features.

One crucial parameter is the so-called quality factor (*QF*) which describes the damping of the oscillation. It is defined as the ratio of the resonance frequency over the full width of the resonance frequency at its half maximum peak:[16]

$$QF = f_0 / \Delta f .$$ (3.39)

The *QF* is a measure for the energy loss associated with the damping in relation to the energy retained in the oscillation. The higher the *QF*, the slower the damping occurs (the reciprocal of the *QF* gives the damping factor). As a consequence, a high

3.4 Experimental Setup

QF is required for a high sensitivity, however, it severely limits the scanning speed due to the increased response time of the system. Therefore, a compromise has to be found between the sensitivity, that is between a reasonable *QF* and the scanning speed. In practise, under ambient conditions, *QF*s in the order of 10^3-10^4 are usually applicable for near-field measurements, depending on the sample properties, especially regarding the tolerated interaction forces (soft or delicate samples require higher *QF*s resulting in longer acquisition times).[16]

Gold tips were electrochemically etched for SNOM measurements. After etching, the probes were characterized with SEM[5] (see Figure 14).
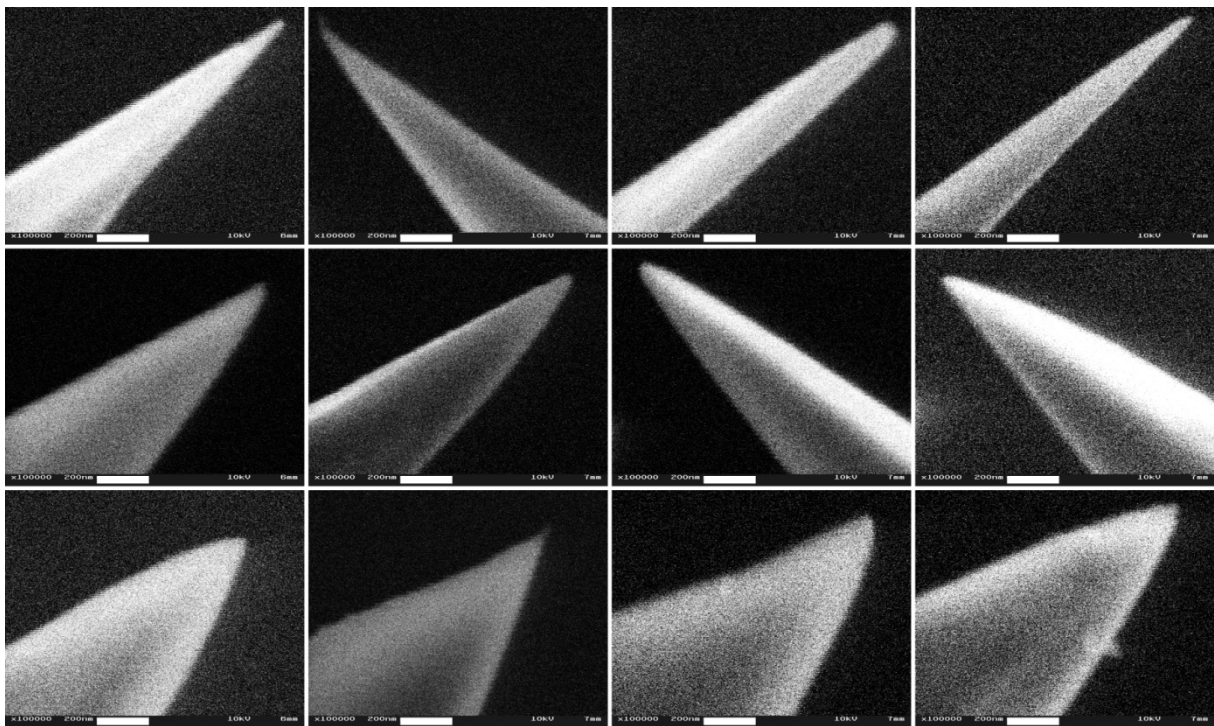
Figure 14:   SEM micrographs[5] (x 100000, scalebar 200 nm) of electrochemically etched gold tips revealing different tip shapes. For SNOM measurements, thin tips with a sharp apex in the order of 10-20 nm were used (cf. upper row).

Only sharp probes with a size of the tip-apex in the order of 10-20 nm were used. According to SEM images, primarily tips with a thin apex were selected (cf. Figure 14, upper row).

---

[5] SEM measurements were kindly performed by Elke Nadler with a Zeiss DSM 962.

3.5 Synthesis and Characterization of Gold Nanoparticles

Gold Nanospheres

Gold nanospheres of various diameter were purchased from BBInternational (Cardiff, UK) and Sigma-Aldrich Chemie GmbH (Steinheim, Germany). The size variation from the nominal diameter is given by the manufacturer with 15 %.

Gold Nanorods

Gold nanorods of different aspect ratio R were synthesized following a wet chemical procedure published by Nikoobakht and El-Sayed.[95] The synthesis resulted in particles with values for R ranging from 1.5 to 4.7.[87] Throughout all experiments, triple distilled water was used. Other chemicals were purchased from Sigma-Aldrich Chemie GmbH (Steinheim, Germany) and used without further purification.

For the synthesis of gold nanorods, the surfactant hexadecyltrimethylammonium bromide (cetyltrimethylammonium bromide, CTAB) is used. It is only soluble in water above 25 °C, thus, throughout the synthesis, the temperature has to be maintained between 25 and 30 °C, *e.g.* with a water bath. In addition, the yield sensitively depends on the reaction temperature. The synthesis uses seed and growth solutions which are prepared separately, all solutions are aqueous.

Seed solution: Solutions of CTAB (V = 5 ml, c = 0.20 M) and of hydrogen tetrachloroaurate(III) trihydrate ($HAuCl_4 \cdot 3H_2O$, V = 5 ml, c = 0.50 mM) were mixed in a plastic tube. The resulting solution was yellow-orange in colour. Under thorough stirring, 0.6 ml of ice-cold sodium borohydride solution ($NaBH_4$, c = 0.010 M) were added. As a result, the colour changed to a brownish yellow. Stirring was continued for another 2 min. Afterwards, the solution was kept at 25 °C and used after 5 min. The borohydride reduces the gold(III) ions to elementary gold, leading to the formation of very small particles, the so-called seed.

3.5 Synthesis and Characterization of Gold Nanoparticles

Growth solution: Equivalents of 5 ml of CTAB solution (c = 0.20 M) were added to different amounts of silver nitrate solutions (AgNO$_3$, V = 0.050, 0.10, 0.15, 0.20 and 0.25 ml, c = 0.0040 M). Afterwards, 5 ml of HAuCl$_4$ solution (c = 0.0010 M) were added to each mixture. Dissolved ascorbic acid (V = 70 µl, c = 0.0788 M) was added after gentle mixing. As a result, the coloured solutions become clear and uncoloured since the gold ions are mildly reduced by the acid. Finally, a small amount of seed solution (V = 12 µl) is added to each batch at 27-30 °C. The different amount of silver ions in the five mixtures leads to particles of different **R**. Depending on the particle size, the colours of the solutions gradually develop within 10-20 minutes. After one day, the reaction is completed. The synthesis procedure results in particles with a width of 10-20 nm as measured with transmission electron microscopy (TEM, data not shown).

During the synthesis, also a small amount of spherical particles is formed. The gold nanorods can be purified by centrifugation which also reduces the surfactant concentration and removes undesired ions. If the CTAB concentration was not reduced, crystallization could damage the nanoparticles. For purification, the solution was centrifuged twice, first 10 min at 21000 g and second for another 10 min at 9500 g (Mini Spin Plus, Eppendorf AG, Hamburg, Germany). Each time, the supernatant was discarded and replaced with fresh water. This procedure also allows to adjust the final particle concentration, depending on the achieved yield.

From extinction spectra, **R** can be determined by fitting theoretically predicted data to the experimental one. Moreover, the spectra allow to judge the quality of the particle solutions. For very inhomogeneous samples, more than two plasmon bands occur or the bands are broadened. The presence of many spherical particles results in an increased intensity of the plasmon band around 520 nm. Thus, a qualitative judgement is directly possible while precise analysis has to include simulated data.

Gold nanotriangles

Triangular gold nanoplates[6] were produced by a wet chemical synthesis.[87, 151] An aqueous solution of trisodium citrate ($Na_3C_6H_5O_7$, V = 15 ml, c = 1.67 mM) was heated to 68 °C under reflux and an aqueous solution of tetrachloroaurate(III) trihydrate ($HAuCl_4 \cdot 3H_2O$, V = 10 ml, c = 1.25 mM) and CTAB (c = 7.5 mM) added, which was preheated to 50 °C. Upon further heating to 82 °C, the orange solution turned colourless and finally light blue within about five min. Reaching the final reaction temperature, the heating was stopped and the flask cooled. The nanoparticles were isolated by centrifugation (15 min, 3000 g) to remove excess surfactant. The synthesis also produces hexagonal and a few pentagonal nanoplates as byproducts. Triangular nanoplates with an average edge length of 85 ± 25 nm and a height of 6-17 nm are to be expected as specified in the literature.[151] These values seem to correspond fairly well with the results from SEM and AFM measurements. Most particles found are about 100 nm wide, although smaller and larger triangles are present in the sample as well as a few hexagonal particles. The optical extinction spectrum (see Figure 17, p. 56) is in good agreement with the one from the literature[151], while the plasmon band is slightly broader, indicating a more inhomogeneous sample.

---

[6] Gold nanotriangles were synthesized by Inga Olliges.

3.5 Synthesis and Characterization of Gold Nanoparticles

3.5.1 Scattering and Absorption of Gold Nanoparticles

Due to the excitation of SPs, *i.e.* collective electron oscillations, by light at optical frequencies, gold nanoparticles strongly interact with light. The strong absorption and scattering results in vivid colours of the aqueous dispersions of the particles with the colour depending on their size and shape. For particles ranging up to 30 nm in size, absorption mainly determines the optical properties while the impact of scattering increases with size and becomes dominating with approximately 100 nm.[45]

Gold nanospheres

Spherical gold nanoparticles strongly absorb and scatter the light in the green region of the electromagnetic spectrum around 520 nm. Depending on the particle size, the wavelength is slightly red shifted (to roughly 550 nm for a diameter of 80 nm). The experimental extinction spectra for diameters *d* = 5 to 80 nm are shown in Figure 15.
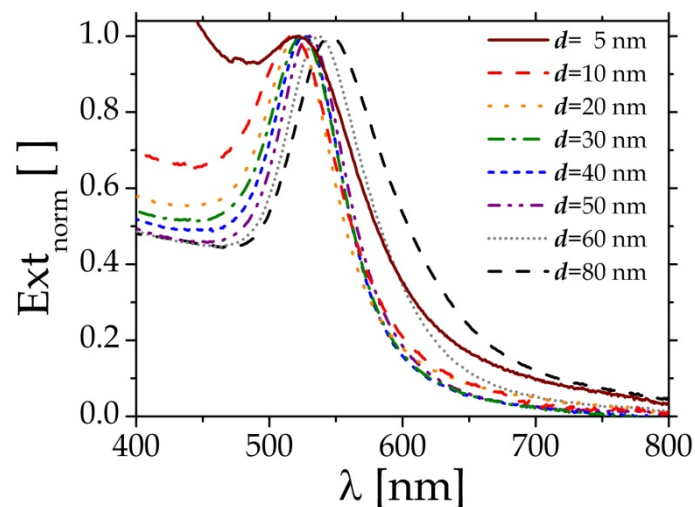
Figure 15: Experimental extinction spectra of aqueous solutions of gold nanospheres for various diameters *d*. The extinction maximum slightly shifts with the particle size. The plasmon resonances are summarized in Table 3. The shape of the spectra is comparable, only for sizes below 10 nm a different shape is found due to a change in the particles' electronic properties.

The plasmon resonance slightly shifts to the red with increasing particle size. For particles with sizes below 10 nm, the shape of the spectrum changes (see Figure 15), because of the different electronic properties of very small particles, towards a stronger absorption below 500 nm. The extinction maxima **Ext**$_{max}$ are summarized in Table 3.

Table 3:   Extinction maxima **Ext**$_{max}$ of gold nanospheres for various *d*, taken from the experimental spectra shown in Figure 15. **Ext**$_{max}$ were determined by fitting a Lorentzian function to the experimental spectra. The plasmon band slightly red shifts with increasing particle size while the spectral shape dramatically changes for sizes below 10 nm.

d [nm]	5	10	20	30	40	50	60	80
Ext$_{max}$ [nm]	518	515	519	523	526	529	538	547

Aqueous solutions of gold nanospheres as treated here show a clear, red colour. For solutions with a high particle concentration, also the scattered green light can be observed.

Gold nanorods

The optical properties of gold nanorods strongly differ from the ones of spherical particles. Throughout this work, only prolate particles have been used. These particles are characterised by one long (*a*) and two short axes of the same length (*b* = *c*). According to the two main axes of the particles, the plasmon resonance splits in a transversal and a longitudinal mode with different energies. Therefore, the extinction spectra show two plasmon bands. The first, corresponding to the short particle axis *b* is comparable to the one from spherical particles and is situated around 520 nm with only little dependence on the particle length *a*. The second plasmon band for *a* is red shifted with increasing particle length or aspect ratio *R* = *a/b* (see Figure 16).

3.5 Synthesis and Characterization of Gold Nanoparticles
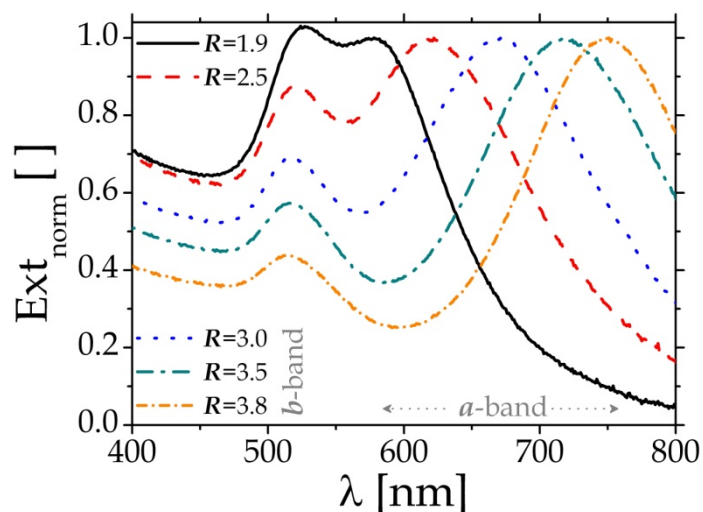
Figure 16: Experimental extinction spectra of aqueous solutions of gold nanorods with various aspect ratios R, the spectra were normalized to the intensity of the longitudinal plasmon band. The plasmon resonance splits in a transversal and a longitudinal mode (b- and a–band) corresponding to electron oscillations along the two main particle axes with different energies. While the b-band around 520 nm is only slightly influenced, the a-band dramatically red shifts with increasing particle length. See Table 4 for numerical values of the resonance wavelengths.

Thus, the optical properties of gold nanorods can be adjusted by tuning R. Modern synthesis techniques allow to finely control the particle size also in the wet chemical approach.[93-95, 152-155] The plasmon resonances from the experimental spectra are summarized in Table 4. The transversal plasmon resonance (b-band) shows a slight blue shift with increasing R, while the longitudinal plasmon peak (a-band) dramatically moves further to the red with increasing particle length.

Table 4: Extinction maxima for the transversal and longitudinal plasmon band of gold nanorods for various R, taken from the experimental spectra shown in Figure 16. The extinction maxima were determined by fitting a Lorentzian function to the experimental spectra. While the b-band only slightly blue shifts, the a-band is strongly red shifted with increasing R.

R [ ]	1.9	2.5	3.0	3.5	3.8
Ext_{trans} [nm]	528	522	519	517	515
Ext_{long} [nm]	574	618	668	720	752

The a-band can be shifted further to the (near) infrared for particles of large R,[153, 155-158] even nanowires with micrometre lengths have been synthesized wet chemically.[157, 159, 160]

Gold nanotriangles

The aqueous solution of gold nanotriangles used throughout this work is of light blue colour, hazel brown in reflection. The experimental extinction spectrum shows a broad plasmon band centred at 620 nm (see Figure 17).
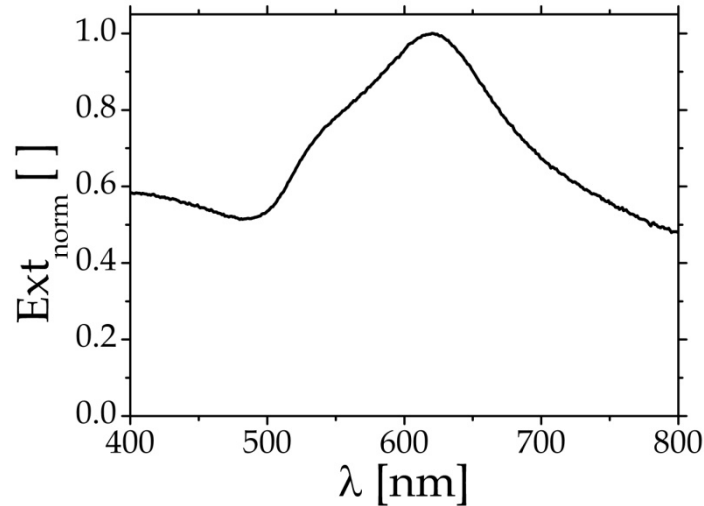
Figure 17: Experimental extinction spectrum of gold nanotriangles. The data is in good agreement with the literature[151], although the band is broadened, indicating a more heterogeneous sample. According to SEM and AFM data, most particles have an edge length of approximately 100 nm, while also smaller and larger triangles were present, as well as hexagonal particles.[87]

AFM and SEM measurements of the gold nanotriangles (see Figure 28, p. 76) confirmed an edge length of approximately 100 nm for most particles as expected from the literature[151]. Also smaller (~60 nm) and larger triangles (~200 nm and 500 nm) were found as well as hexagonal particles (edge length ~270 nm).[87] This size variation probably accounts for the slightly broader plasmon band in the extinction spectrum as compared to the literature.

3.6 Sample Preparation

Samples of gold nanoparticles were prepared on glass cover slips as sample substrate after cleaning with acetone and methanol of spectroscopy grade (Uvasol®, Merck KGaA, Darmstadt, Germany). Afterwards, properly diluted aqueous particle solutions were spin coated. Parameters were carefully adjusted to produce samples with single, spatially isolated particles (50 µl, 1500-2000 rpm after 5 min).[87] Most samples were studied as prepared, *i.e.* the gold particles were exposed to air.

In some cases, however, the particles were covered with a droplet of water or immersion oil to adjust the refractive properties of the embedding medium and the sample interface. For this purpose, the lower piece of a pipette tip was fixed on top of the sample with nail polish. Alternatively, highly diluted particle solutions were sealed in-between two cover slips. The edges of the upper, smaller cover slip were sealed with nail polish to prevent evaporation of the water. This resulted in a distance of a few micrometres between the two glass plates. The distances were measured by successive focusing on the two interfaces with the scanning stage where the resulting voltages can be directly converted into defined distances.

Other samples were prepared with gold nanorods embedded in a polymer film of polyvinyl alcohol (PVA, Mowiol® 40-88, Sigma-Aldrich Chemie GmbH, Steinheim, Germany). The polymer was dissolved in triple distilled water under continuous stirring and heating to 90 °C in a water bath for several hours. After cooling, the aqueous solution of the polymer (8 %, 300 µl) was mixed with the particle solution (100 µl). Spin coating of the solution (50 µl, 1500-2000 rpm) on cleaned cover slips produced smooth films with embedded particles and arbitrary 3D orientation.[87]

The polymer films were characterized with ellipsometry and AFM. [7] The film thickness was found to be around 450 nm and the AFM data confirmed smooth film surfaces with a roughness of 2-3 nm. The refractive index of the PVA was measured as 1.508 at 633 nm by ellipsometry (data not shown).

---

[7] AFM on the PVA films was performed by Frank Wackenhut, ellipsometry was measured by Ute Heinemeyer in the group of Prof. Dr. Frank Schreiber (Institut für Angewandte Physik, Eberhard Karls Universität Tübingen, Germany).

4 Confocal and *in situ* AFM Imaging of Single Gold Nanoparticles

4.1 2D Orientation of Single Gold Nanorods in Luminescence Mode

The orientation of individual, spatially isolated metal nanorods can be directly imaged and precisely determined with confocal microscopy in combination with DMs. As shown above (see chapter 3.2.2, p. 36),[35, 36, 39-41] the elastically scattered light is well suited for this purpose. However, gold nanoparticles also show a strong and stable photoluminescence (PL), which can be detected alternatively. Either a notch or a long-pass filter are to be implemented in the detection path to allow for proper spectral detection (alternatively, a dichroic mirror could be used). The PL images result to be almost BG free and therefore usually offer a better signal-to-background ratio than the scattering data. In most cases, a higher laser excitation power is necessary to stimulate sufficient PL. In the following, different images of gold nanorods acquired in both modes upon excitation with an APDM at 633 nm are shown and compared. For better visibility, the contrast was adjusted and inverted for the scattering image. A one-colour intensity scale was used (scattering: red, PL: green). Merging the images of both modes results in a yellow intensity scale, mapping their overlap.

The overall shape of the pattern and the orientational information remains unaffected of the detection mode, as can be recognized from Figure 18.
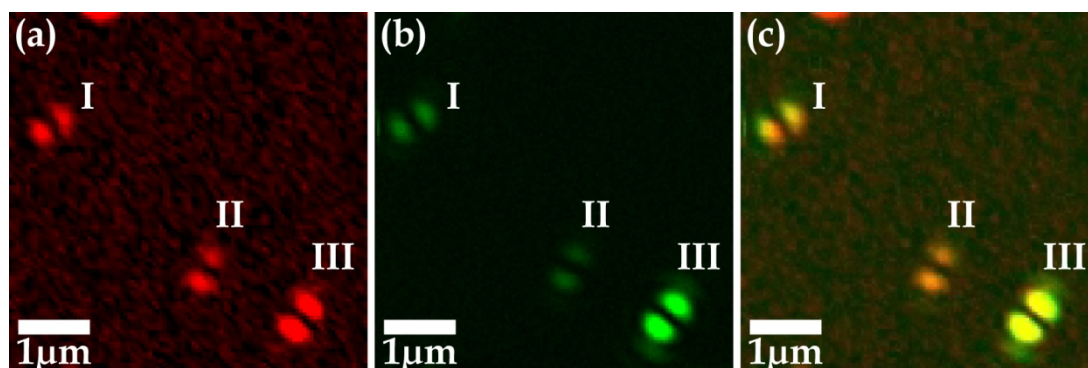
Figure 18: (a) Scattering and (b) PL images of the same set of individual gold nanorods (APDM at 633 nm) with adjusted contrast and inverted scattering image. Both images are merged in (c) resulting in a yellow intensity scale mapping the perfect matching of the two modes.

4.1 2D Orientation of Single Gold Nanorods in Luminescence Mode

The figure shows three gold nanorods in both modes (Figure 18 a, b) as well as an overlay of the two images (Figure 18 c). Since the scattering (red) and PL (green) pattern perfectly match in shape, the resulting overlaid patterns are all yellow, with slight variations due to different intensities.

A larger scan area comparing the scattering and luminescence mode is shown in Figure 19. Despite the obvious similarity, there are also some discrepancies which can be recognized from the overlay in Figure 19 c.
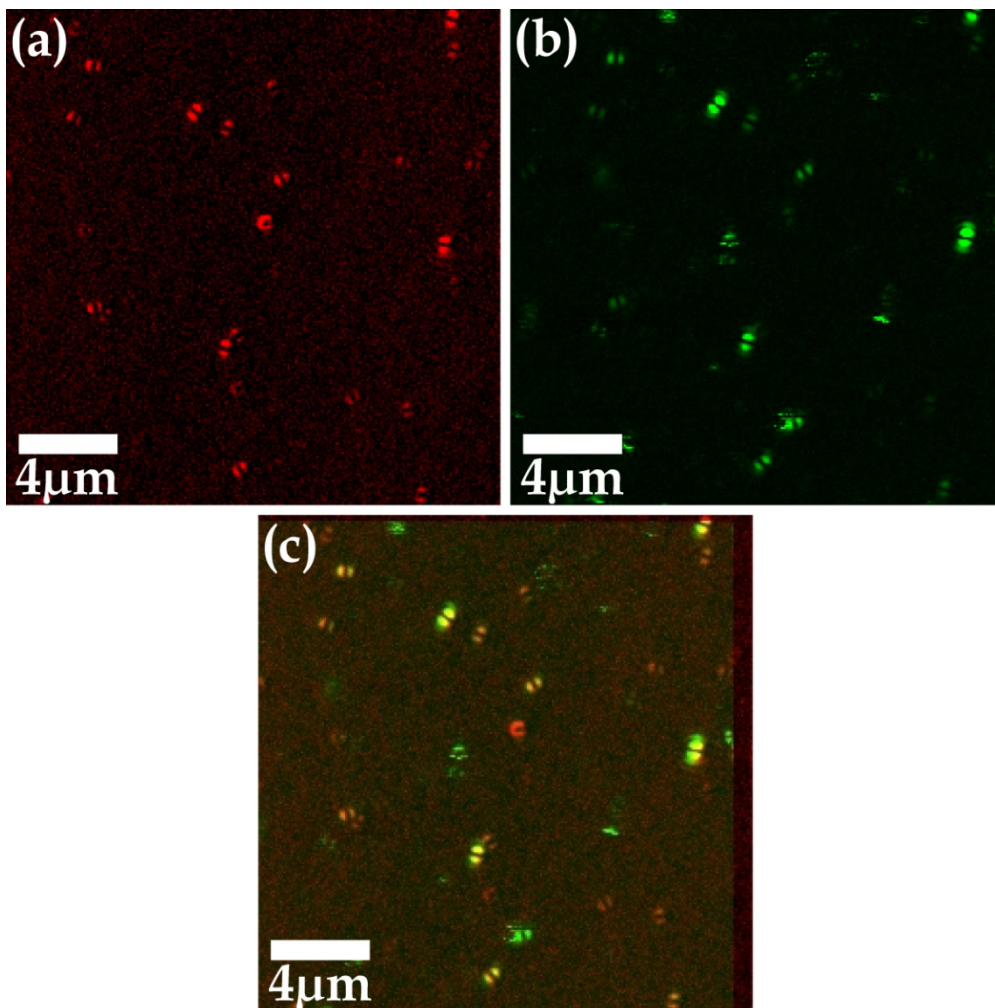
Figure 19: (a) Scattering and (b) PL images of the same set of individual gold nanorods (APDM at 633 nm) with adjusted contrast and inverted scattering image. Both images are merged in (c) resulting in a yellow intensity scale mapping the almost perfect matching of the two modes. Some patterns are only visible in PL mode. For scattering, the signal can be safely attributed to gold nanorods. The partly unstable PL emission (blinking and bleaching) suggests some molecular fluorescence being involved.

In addition, there are several patterns only appearing in the luminescence image, which are therefore green in the overlay. All these patterns show signs of an unstable emission, that is either blinking or bleaching. However, most of them are of a two-lobed shape and some are surprisingly intense. Because of the unstable emission, these patterns can partly be attributed to molecular fluorescence emission (especially when bleaching is observed). Two-lobed patterns can as well be caused by linear dipole moments of single fluorescent molecules. However, when an ensemble of molecules is observed, it is highly unlikely that the molecular dipole moments are oriented a priori. Hence, fluorescent patterns should be ring-shaped because of the arbitrary distribution of molecular dipole moments. Therefore, such two-lobed patterns, if due to fluorescence, have to be caused by single molecules. Consequently, frequent blinking is expected as well as fast bleaching.[161] Both phenomena are observed in the experimental data.

Another sample area is imaged in Figure 20. First, it can be recognized that the image contrast is improved in the luminescence mode, that is, the particles are better visible than in the scattering data. Moreover, there are more two-lobed patterns, as can be clearly recognized from the several green patterns in Figure 20 c.

4.1 2D Orientation of Single Gold Nanorods in Luminescence Mode
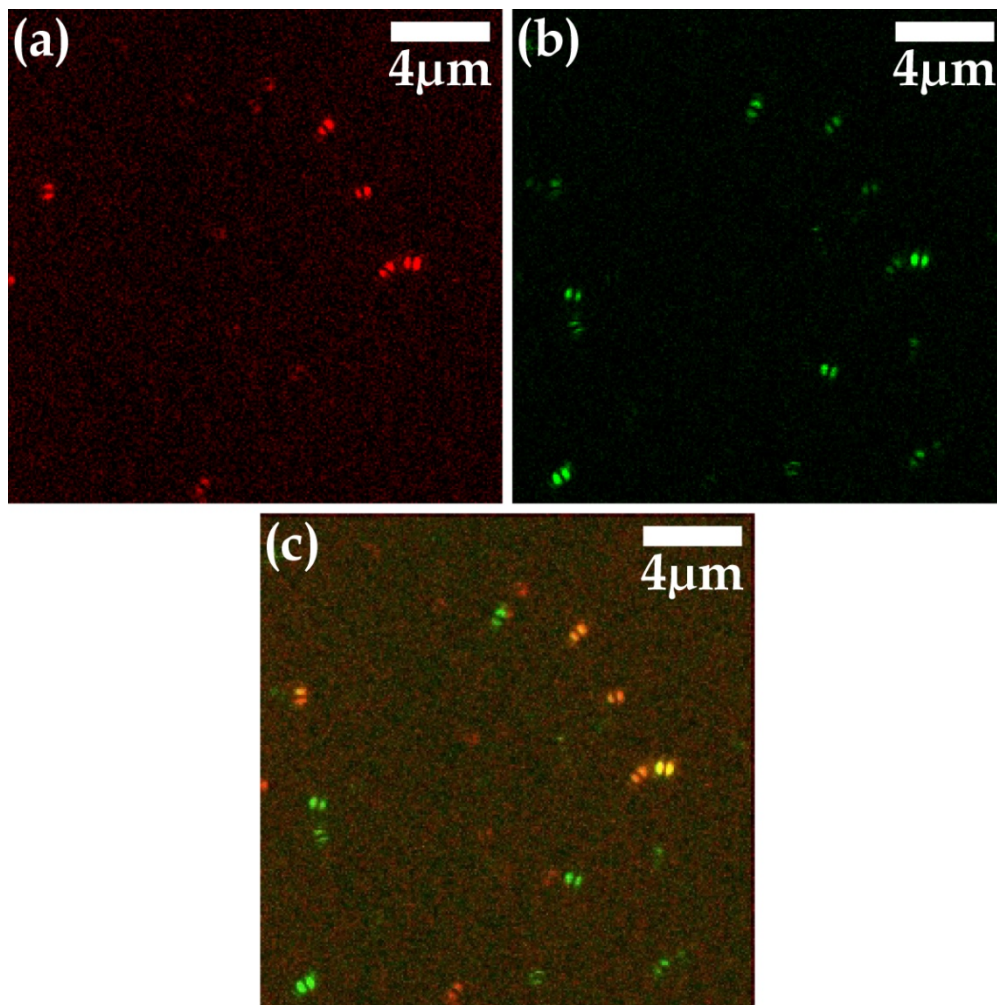
Figure 20: (a) Scattering and (b) PL images of the same set of individual gold nanorods (APDM at 633 nm) with adjusted contrast and inverted scattering image. Both images are merged in (c) resulting in a yellow intensity scale mapping the almost perfect matching of the two modes. Some two-lobed patterns are only visible in either scattering or PL mode. Since the PL emission is mostly very stable here, it can safely be attributed to gold particles, which are not detected in the scattering mode but show a sufficiently strong PL for detection.

This time, the luminescence patterns are stable, neither blinking nor bleaching are observed. Hence, the intense PL probably has to be attributed to gold nanorods. However, there are also some particles which only appear in the scattering mode (red in the overlay). Additionally, it emphasizes that the influence of the excitation intensity and wavelength is different for the two imaging modes. For the scattering, the influence of the individual particle's SP frequency and hence its size is not as important as for the PL. For the PL, the respective individual SP resonance in relation to the excitation wavelength is crucial and even small size variations might lead to

strong differences in the absorption efficiencies. To excite the plasmon-mediated PL of single gold nanoparticles, the incident laser intensities have to be approximately one order of magnitude higher than in the scattering mode. Therefore, the excitation intensity might be too low to excite PL for all particles, while it is still sufficient to detect the scattered light. Additionally, differences in the local environment of the particle might also sensitively influence the respective scattering and luminescence efficiencies. On the other hand, the image contrast in the scattering mode is governed by interference and the phase relation between the reflected and the scattered field is critical (see eq. 3.38, p. 35). For $\varphi = \pi/2$, the interference term becomes zero and with it does the whole signal. Since the phase is influenced by a number of different parameters (*e.g.* the particle size, its direct environment, the objective's *NA* or the refractive properties of the sample interface), it is not quantitatively predictable. Consequently, it might as well prevent the detection of some particles in the scattering mode which are easily detectable by their PL emission.

To further compare the scattering and PL mode, several areas with gold nanorods are shown in Figure 21. For this sample, the concentration of the particles was considerably higher than usual, resulting in partial clustering of the particles and therefore leading to some patterns which are not two-lobed but more ring-shaped. In most cases, however, the particles are still separated and the characteristic two-lobed patterns are observed. Most particles are visible in both modes and the patterns perfectly coincide in terms of shape, orientation and localization. Again, several particles are only visible either in the scattering or the PL mode. However, most of these particles are solely detected by their luminescence and are invisible in the scattering data. As discussed above, this might be due to the influence of the phase term in the scattering signal as well as caused by slight variations in the particle size or in the immediate particles' environment.

4.1 2D Orientation of Single Gold Nanorods in Luminescence Mode
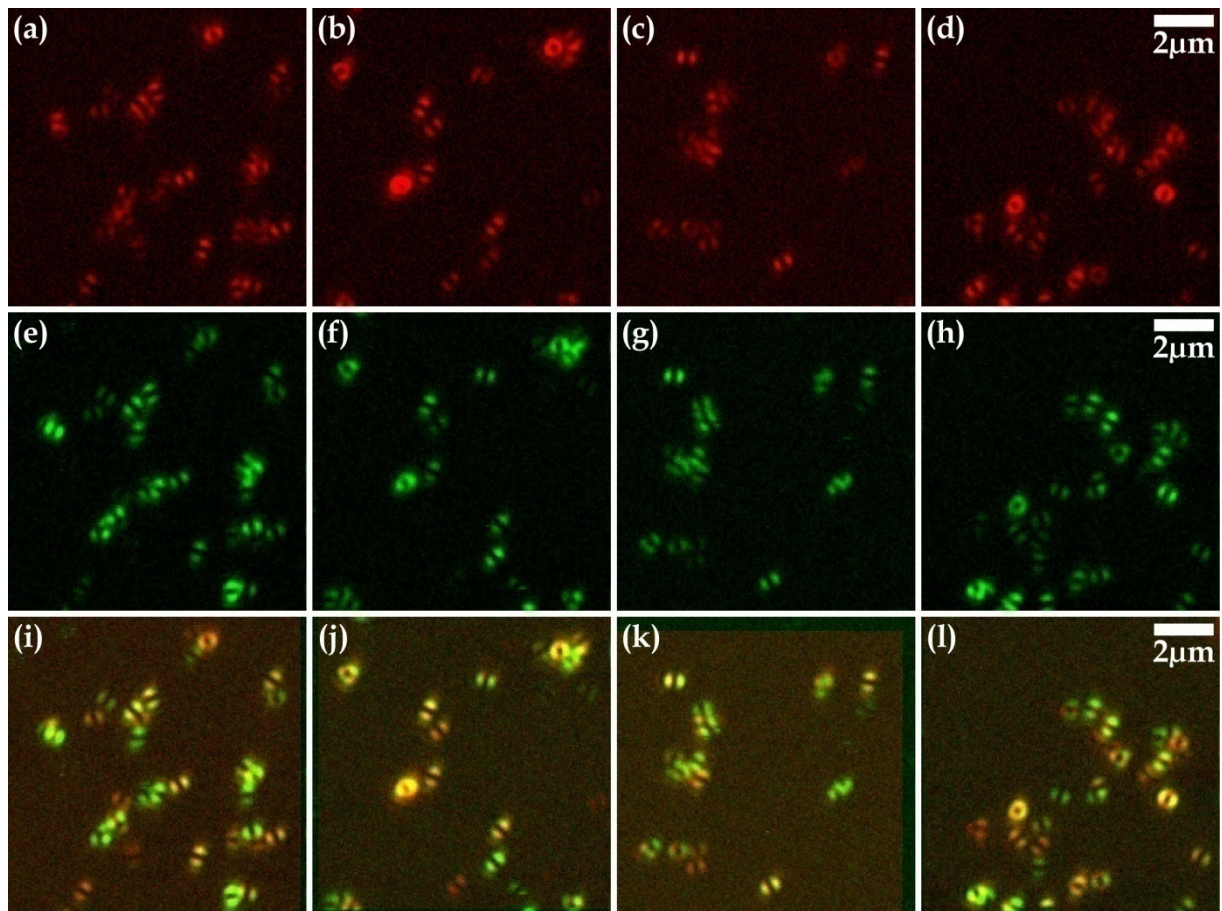
Figure 21: Different areas of gold nanorods in (a-d) scattering and (e-h) luminescence mode (APDM at 633 nm). The contrast was adjusted for better visibility and inverted for the scattering image. For comparison, the images have been overlaid in (i-l), resulting in a yellow intensity scale mapping the overlap (due to intensity differences some particles appear orange or greenish). While most particles are visible in both modes, some can be solely detected in either scattering or luminescence mode (red or green in the overlay).

At first sight, the particles are clearly visible in both imaging modes. However, the image contrast appears to be higher in the PL data. To quantitatively examine this impression, the SNR is determined for the images shown in Figure 21. Since individual particles considerably differ in their intensity, the span of the overall intensity scale was chosen to determine the values for the signal S. To determine the noise N, profiles through (signal-free) background areas were taken, perpendicularly to the scanning direction to correct for eventual drifts in the images.

The standard deviation of these data was considered as the average noise of the background. The numerical values are summarized in Table 5. It can be recognized that the SNR is indeed higher for the PL data.

Table 5: Determination of the SNR for the images shown in Figure 21 comparing the scattering and luminescence mode. The signal S was determined as the total span of the overall intensity scale of each image. To determine the noise N, profiles were measured through background (*i.e.* signal-free) areas, perpendicularly to the scanning direction. The standard deviation of these values was considered as the noise level. The PL data results in higher SNR values as already expected from the qualitative visual impression.

Figure 21	scattering			luminescence		
	S [kHz]	N [kHz]	SNR [ ]	S [kHz]	N [kHz]	SNR [ ]
a, e, i	140	7.5	19	40	1.05	38
b, f, j	220	10.5	21	33	1.03	32
c, g, k	140	6.8	20	31	1.10	28
d, h, l	180	7.9	23	36	1.04	34
mean value	170 ± 33	8.2 ± 1.4	**21 ± 1**	35 ± 3	1.06 ± 0.03	**33 ± 4**

For both detection schemes, the numerical values for individual particles showed considerable variations in the signal intensity. This is to be expected since the scattering and luminescence efficiency sensitively depends on a number of parameters as *e.g.* the size of the particle and its direct environment. In the luminescence mode, the background is much lower and so is the noise level resulting in a better SNR. While for the scattering mode a SNR ≈ 20 is found, a mean value SNR ≈ 30 is observed for the PL mode (see Table 5). A benefit of the PL data is certainly that it is almost background free. Therefore, the image contrast and quality is usually better compared to the scattering mode as also confirmed by the higher SNR. Since the signal only consists of the luminescence light and does not involve an interference term, information about the sample interface is not included. However, both the information about the particle shape (cf. chapter 0, p. 67) and the orientation of metal nanorods is preserved. Therefore, the luminescence mode can be preferable when information about the optical properties of the sample interface are not crucial.

4.1 2D Orientation of Single Gold Nanorods in Luminescence Mode

Because of the higher excitation powers one has to be careful with light-sensitive samples. Working in aqueous or index matching environments can be beneficial to reduce the excitation powers in general.

In addition, luminescence spectra of individual gold nanorods upon excitation at 633 nm were acquired. The PL maximum was found to vary for different particles,
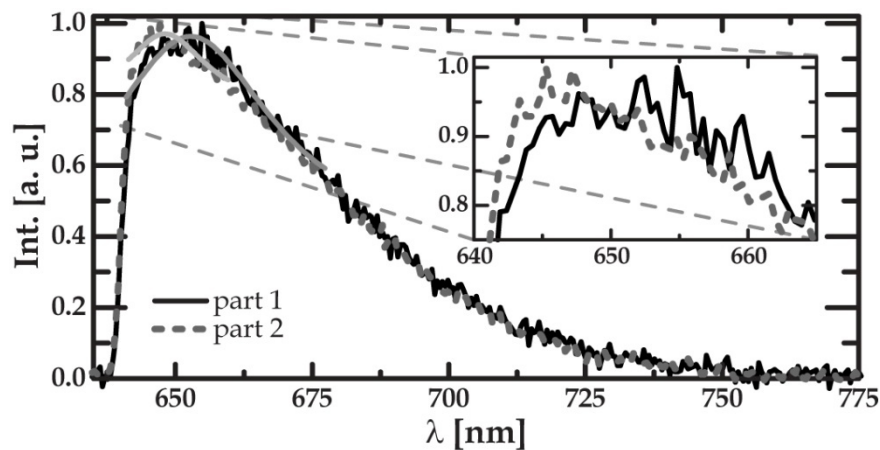
presumably depending on the respective particle's aspect ratio **R** (see Figure 22).

Figure 22: PL spectra of two individual gold nanorods with different PL maxima (APDM at 633 nm). The light grey lines represent Lorentzian fits to the experimental data. A zoom-in of the maxima of the spectra is also provided. The fitting resulted in values for $\lambda_{max,1}$=648 nm and $\lambda_{max,2}$=653 nm.

The luminescence spectra for the two particles shown in Figure 22 slightly vary in their PL maximum. The spectra were fitted with a Lorentzian function resulting in values of $\lambda_{max,1}$ = 648 nm and $\lambda_{max,2}$ = 653 nm, respectively. This PL occurs in a totally different spectral range than the luminescence usually observed in rough (that is nanostructured) gold films or nanoparticles which is reported in the literature and peaks around 530 nm. Such PL is usually explained with interband electron-hole recombination (see chapter 2.1.5, p. 26).[2, 7, 9, 10] For this process, excitation with green or blue light is necessary to provide enough energy. Here, the red light used to excite the gold nanoparticles has not sufficient energy to create electron-hole pairs. However, it strongly interacts with the SPs of the particles being almost in resonance with the longitudinal SP resonance frequency. It has been proposed that PL can also

occur due to the radiative decay of SPs.[2] Considering the energy of the excitation wavelengths and the strong coupling to the particle's SPs, this mechanism appears to be highly probable in this case. In addition, electron-hole recombination cannot explain different spectral properties of individual particles since the PL in this case should solely depend on the electronic band structure of gold. Even the relatively small difference in the maxima of 5 nm (see Figure 22) cannot be easily explained with electron-hole recombination as the underlying process of the PL. Although this might appear a small change at first sight, it corresponds to almost 250 eV which is certainly not negligible for electron-hole recombination. In contrast, the radiative decay of SPs as the underlying process for the PL should directly reflect in different spectra for each nanoparticle depending on its plasmonic properties and hence its size or aspect ratio R. In addition, the size influence should be crucial in this case, therefore even slight variations would easily explain shifts about a few nanometres.

4.2   *In situ* AFM Measurements of Gold Nanorods

The polarizability of the gold particle in the focus of an APDM or a RPDM plays a key role in the image acquisition process. For different particle shapes, the polarizability varies which can be exploited to distinguish between differently shaped particles through their scattering patterns acquired with azimuthally and radially polarized light.[36, 39, 87]

As has been shown above, the highly directed dipole moment induced in gold nanorods renders characteristic two-lobed patterns: when red light at 633 nm is used for the excitation of a gold nanorod, the longitudinal SPs are mainly excited and the particle is polarized along the rod length. Hence, the induced dipole moment follows this direction and two-lobed patterns are observed since the dipole moment can only interact with light which is polarized parallel to the dipolar orientation (see chapter 3.2.1, p. 35).

To further investigate this effect and to prove that the physical orientation of the particles is indeed imaged, *in situ* AFM measurements were carried out. For this purpose, a commercial AFM was implemented on top of the confocal microscope. A home-built device allowed to position the AFM precisely over the sample and into the focus of the optical microscope (see chapter 3.4.3, p. 46). The measurements were taken consecutively but on the same sample area, which could also be verified through the eyepiece of the confocal microscope. Since the scanning directions of the two setups are not synchronized, the images had to be corrected for an eventual rotation afterwards. This can be done comparing larger scan areas with several particles and overlaying the images (see Figure 23). Usually, only slight corrections of 2-3 ° were necessary.
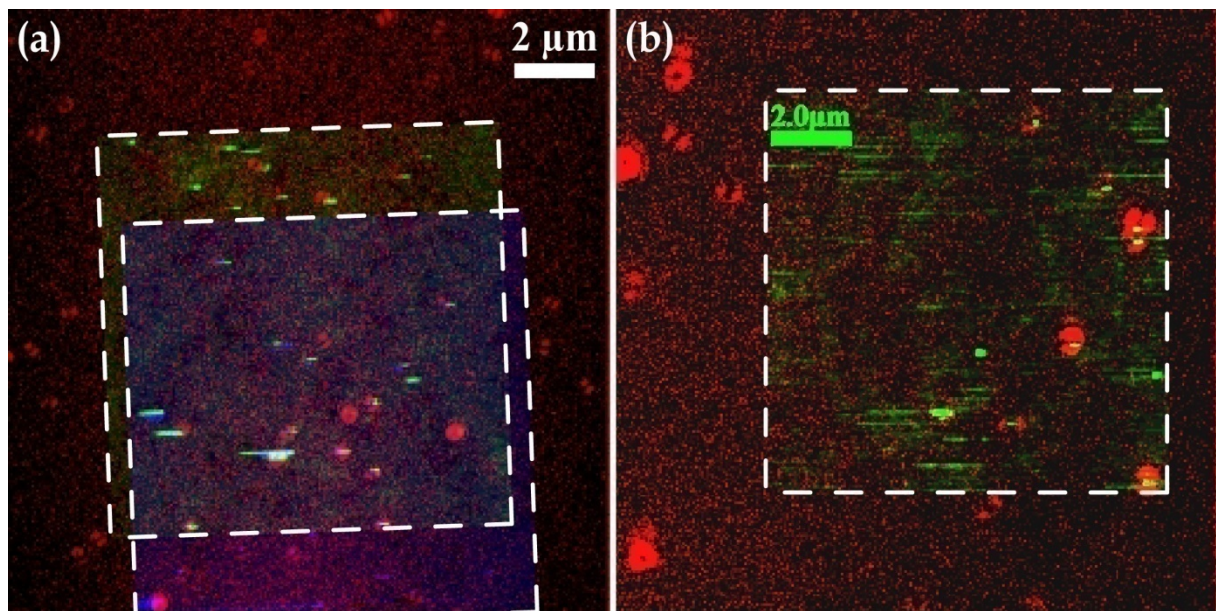
Figure 23: Overlay of confocal (red) and *in situ* AFM (green, blue) data of individual gold nanorods. To correct for eventual rotations of the unsynchronized scanning directions, larger scan areas with several particles were imaged. In (a), the AFM data was rotated by 2 ° counter clockwise to reach an almost perfect matching while in (b) such a correction was not necessary. The white dashed lines map the outlines of the AFM scan areas.

Figure 23 shows a combination of the confocal (red) and AFM (green, blue) images of larger scan areas with individual gold particles which were used to control the agreement of the scanning directions of the two microscopes. Each image was converted to a one-colour intensity scale and the intensity of the scattering data was inverted to provide a positive image contrast. The white dashed lines give the limits of the AFM scanning regions. This way, the rotation of the AFM data is also directly visualized in Figure 23 a. The colours eventually add up to yellow (red and green), purple (red and blue), cyan (green and blue) or white (red, green and blue), depending on their overlap. However, since the two-lobed scattering patterns have a dark "backbone" in their centre, the AFM data may keep its original colour despite a good overlap. Although the scanning piezo electronics of the AFM microscope are not feedback-controlled as the ones for the optical microscope, the data could be overlapped surprisingly well. Typically, topographic images of $10 \cdot 10 \ \mu m^2$ were used for this purpose, providing a reasonable number of particles. To determine the

4.2 In situ AFM Measurements of Gold Nanorods

orientation of individual gold nanorods, smaller areas were scanned, imaging one particle at a time with high resolution.

Since the particles are only spin coated on the glass surface, they can be easily moved or at least rotated by the scanning tip when the scanning parameters are not perfectly adjusted (see Figure 24).
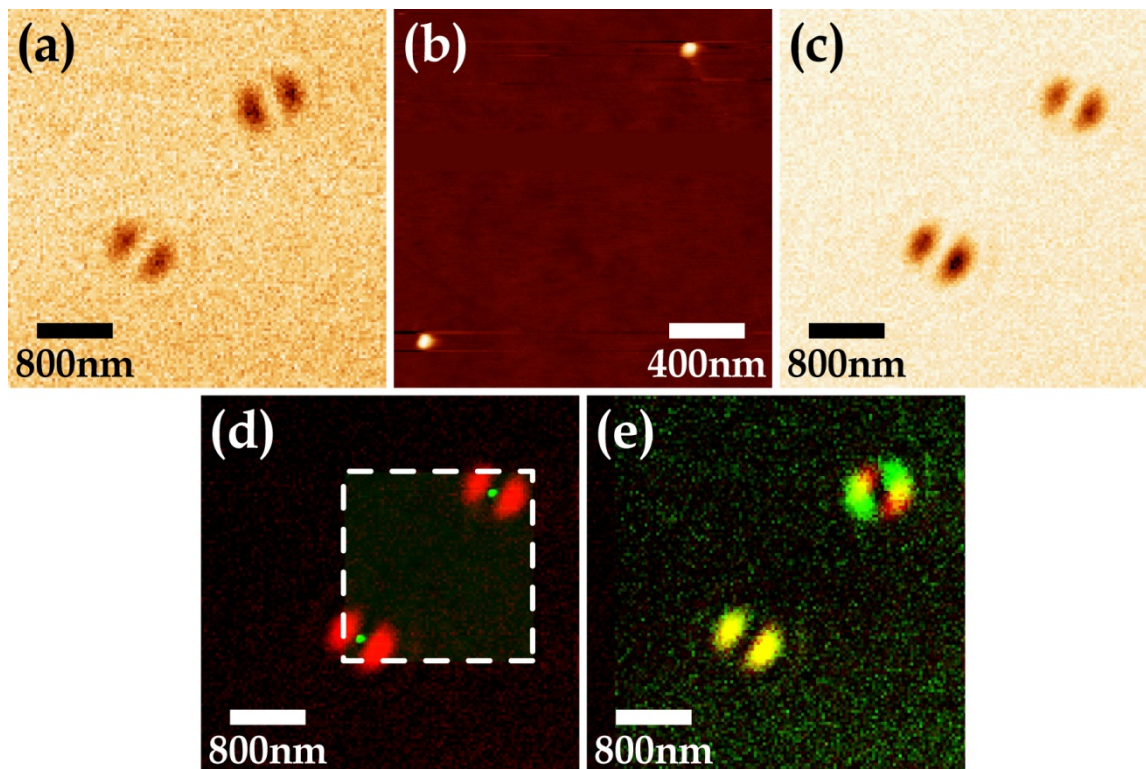
Figure 24: (a, c) Confocal (APDM, 633 nm) and (b) AFM data of two individual gold nanorods. The images were acquired consecutively from (a-c). While the confocal patterns in (a) show a different orientation for the two particles, their orientation is almost identical in the AFM data (b). Therefore, a second optical image was acquired (c), confirming a rotation of the upper right particle by the AFM tip. (d) Shows an overlay of the optical (red) and AFM image (green) illustrating the matching orientation and localization. (e) Overlay comparing the two optical images (a: green, c: red), further illustrating the rotation. For the overlay, the images were converted to a one-colour intensity scale and the scattering data was inverted to provide positive image contrast.

While the confocal patterns in Figure 24 a suggested a considerably different orientation for the two imaged gold nanorods, this is not the case in the corresponding AFM data (see Figure 24 b). Therefore, another optical image of the sample area was acquired, confirming a rotation of one particle by the AFM tip

scanning over the sample (Figure 24 c). The corresponding optical and topographic data is shown as an overlay in Figure 24 d. Both images were converted to a one-colour intensity scale. The scattering data is depicted in red, while the AFM image is shown in green (with the white dashed line giving the outlines of the AFM scan area). In addition, the scattering data was inverted to provide a positive image contrast. The overlay confirms a perfect match of the *in situ* AFM data with the optical image, both concerning the particles' orientation and localization. Upon excitation with an APDM at 633 nm, the long particle axis runs parallel to the two lobes, creating a "butterfly" pattern in the overlay. In other words, the long particle axis is oriented perpendicularly to the line connecting the two lobes. In Figure 24 e, the two confocal images are shown as an overlay (first optical image (a): green, second optical image (c): red) to further illustrate the rotation of the particle by the AFM tip. Please note that the particle's position remains unchanged, solely its orientation changes. Such a rotation would not be detectable with standard confocal microscopy but is easily recognized with DMs.

In Figure 25, overlays of confocal images (APDM at 633 nm) and the corresponding *in situ* AFM data for several individual gold nanorods are shown. Again, all images were converted to one-colour intensity scales and the scattering data was inverted to provide positive image contrast. The optical image is shown in red, while the AFM data is depicted in green.

4.2 In situ AFM Measurements of Gold Nanorods
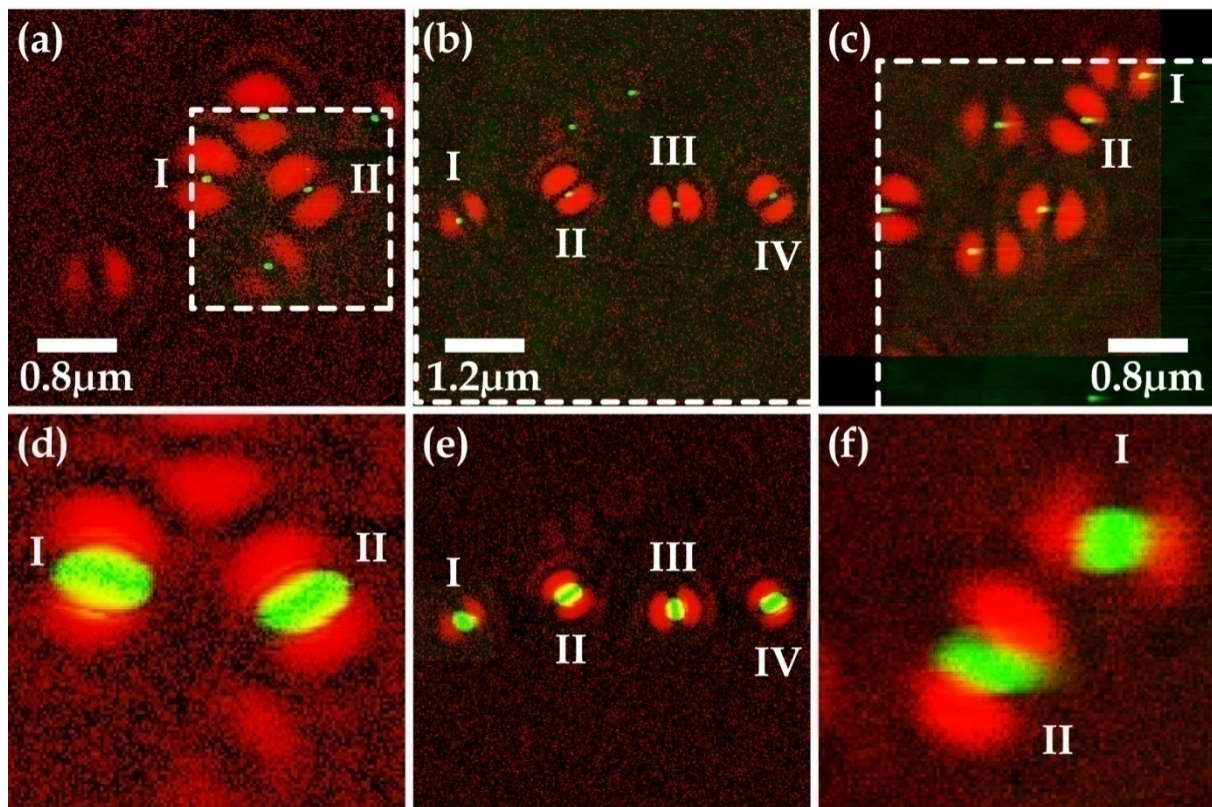
Figure 25: Overlay of confocal (red, APDM at 633 nm) and AFM (green) images of individual gold nanorods. In the upper row (a-c), the AFM data is in scale with the optical image. In the lower row (d-f), high resolution AFM data is provided not in scale with the confocal image for better visualization of the particles' orientations. The optical and topographic data nicely agree in terms of localization and especially orientation of the particles. The white dashed lines give the outlines of the AFM scanning areas.

The upper row in Figure 25 a-c shows the topographic data in scale with the confocal image. Additionally, high resolution AFM images are given in the lower row (d-f) to illustrate the particle orientation in more detail. For better visualization, this data is not in scale with the optical images. As expected, the physical particles' orientation is directly reflected in the scattering patterns, resulting in "butterfly" shaped patterns in the overlay with the AFM data forming the "body" and the two lobes of the optical pattern representing the "wings". Again, the white dashed lines in Figure 25 give the outlines of the AFM scanning areas.

The particle size and aspect ratio R can be extracted from the AFM images. In total, 32 particles were analyzed and for each particle both the forward and the backward scan image was used. The FWHMs from profiles of the AFM data revealed

an average height $h = 22.6$ nm. The particle axes were measured as $a = 77.2$ nm and $b = 51.0$ nm in average (see Table 6). Since these values for the particles' axes are convoluted with the AFM tip, they have to be corrected for the tip size. In this case, h was considered as an estimate of b and a was corrected for accordingly. The data resulted in a mean aspect ratio $R = 2.2 \pm 0.5$ in fair agreement with the UV/Vis spectrum of the particle solution with an extinction maximum at 631 nm. This maximum corresponds to a value of $R = 2.5$ according to a theoretical fit function.[162] Table 6 summarizes the numerical mean values from the AFM measurements while Figure 26 gives the size distribution for the analyzed particles.

Table 6: Mean values of the particle dimensions for individual gold nanorods as measured by *in situ* AFM on a total number of 32 particles. The values given for a and b were measured as FWHMs of profiles from the AFM images. The particle height h was considered as a measure for b to estimate the tip size and correct the values accordingly. The obtained R is in fair agreement with the UV/Vis spectrum of the particle solution ($\lambda_{max} = 631$ nm and $R = 2.5$)[162]. The distribution of R is given in Figure 26.

values as measured by AFM			corrected values		aspect ratio R [ ]
long axis a [nm]	short axis b [nm]	height h [nm]	tip size [nm]	long axis a_{corr} [nm]	
77.2	51.0	22.6	30.3	47.2	2.2
± 12.6	± 12.4	± 2.4	± 12.2	± 13.4	± 0.5

4.2 In situ AFM Measurements of Gold Nanorods

The distribution of the aspect ratio R which was found in the AFM measurements is plotted in Figure 26. Most particles, that is 55 % of the sampling, was found with R ranging between 1.8 and 2.2 and therefore were slightly shorter than expected from the UV/Vis spectrum.
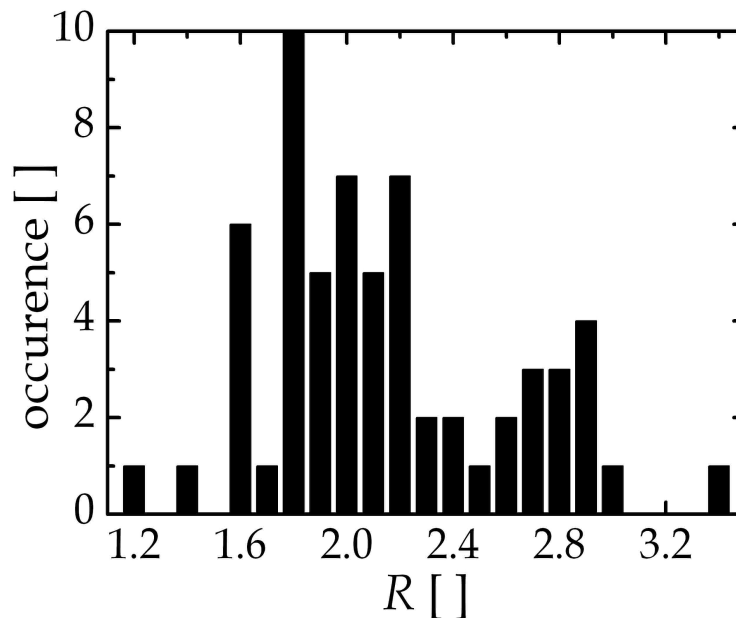
Figure 26: Distribution of the aspect ratio R extracted from the AFM data as summarized in Table 6. Values of 1.8-2.2 are most prominent in the sampling. Due to the impact of higher values, the average value is shifted to $R = 2.2 \pm 0.5$. Very few (almost) spherical particles were found which can be explained with the *in situ* imaging method which was controlled by optical microscopy.

Very few (almost) spherical particles were found which can be attributed to the *in situ* imaging. Since the AFM measurements were controlled by confocal microscopy, only particles were imaged, which were clearly identified as gold nanorods by their two-lobed scattering patterns.

4.3   Confocal and *in situ* AFM Imaging of Single Gold Nanotriangles

Beside the orientational information, also information about the particle shape is included in the optical pattern.[36, 39, 87] However, the excitation wavelength has to be chosen carefully when such information is to be detected. Since it is directly coupled to the SPs of the particles, electron oscillation has to be excited mainly along one axis. In practice, it is convenient to exploit the longitudinal plasmon oscillation of gold nanorods with red light. Using green light for excitation results in excitation of both the longitudinal and the transversal SPs leading to a ring-shaped (or doughnut-like) pattern.[39, 87] Consequently, any information about the particle's orientation is lost and likewise is the shape information.

For an isotropic point-like scatterer, the PSF of the excitation light is imaged. Such an isotropic scatterer is realized with a gold nanosphere. Consequently, when an APDM is used for excitation, the resulting pattern resembles a ring, while a spot-like pattern is found in the case of a RPDM (see Figure 27 a, d).[39, 87] In contrast, gold nanorods represent a class of highly anisotropic scatterers, as mentioned before and produce totally different scattering patterns (see Figure 27 b, e). Therefore, these two classes of particles can be easily distinguished from each other.[36] A more complex particle shape is realized for the case of gold nanotriangles, *i.e.* relatively flat plates with the shape of an equilateral triangle. These particles rendered distorted rings as compared to spheres when excited with an APDM or almost spot-like scattering patterns in the case of a RPDM (see Figure 27 c, f).[39, 87] Even within a single confocal image, the position of the distortion varied from particle to particle. Consequently, it indicates the 2D particle's orientation and is not related to an irregularity of the excitation beam, which would have to be homogeneous for the whole image.

4.3 Confocal and in situ AFM Imaging of Single Gold Nanotriangles
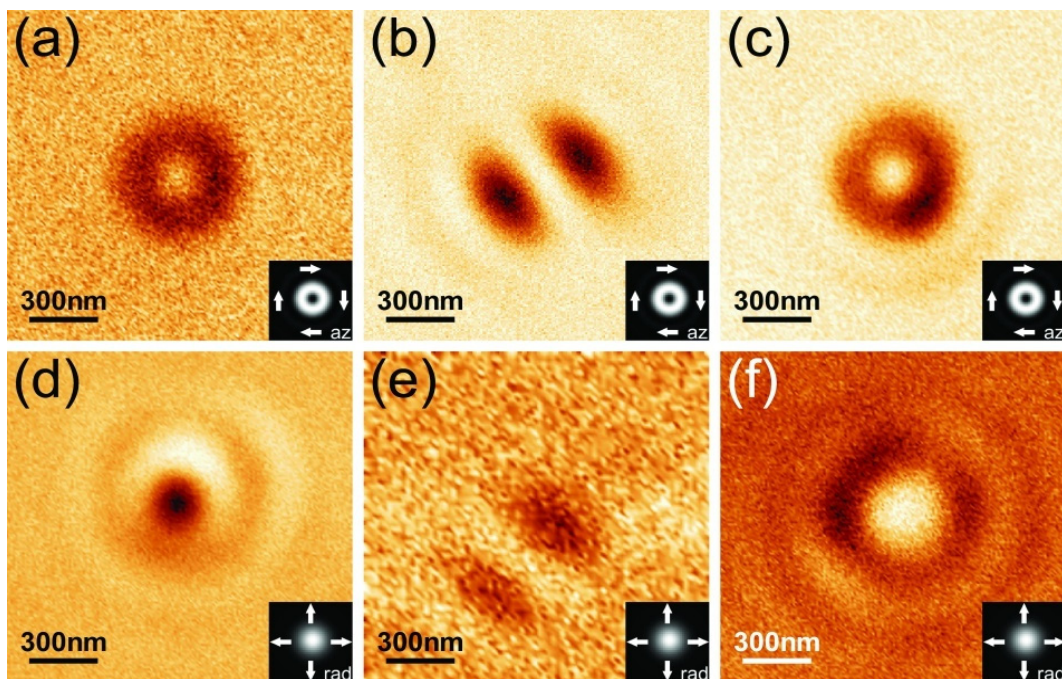
Figure 27: Scattering images of differently shaped gold nanoparticles (a, d: sphere, b, e: rods, c, f: triangle), excited with an APDM (upper row) and a RPDM (lower row). The particles can be clearly distinguished by their varying patterns. While an isotropic scatterer as a gold nanosphere probes the PSF of the excitation beam in focus, the highly directed induced dipole moment of a gold nanorod maps the long axis of the particle and hence visualizes its orientation. Triangular gold nanoplates render distorted rings or spot-like patterns as compared to spheres upon excitation with an APDM or RPDM, respectively. The position of the distortion varies from particle to particle probably indicating the particle's orientation and is not related to irregularities of the excitation beam. Figure taken from reference [39].

The gold nanotriangles were synthesized following a wet chemical approach (see chapter 3.5, p. 52).[151] Most triangular plates showed an edge length of about 100 nm as confirmed with SEM (see Figure 28 a). However, the sample also contained larger triangles with sizes of approximately 500 nm (see Figure 28 b) as well as smaller ones of about 60 nm in size and a few hexagonal particles with an edge length of approximately 270 nm.[87] The thickness of the triangular plates is given with 6-17 nm in the literature.[151] The AFM measurements carried out in this work are within this range, although in the upper region.
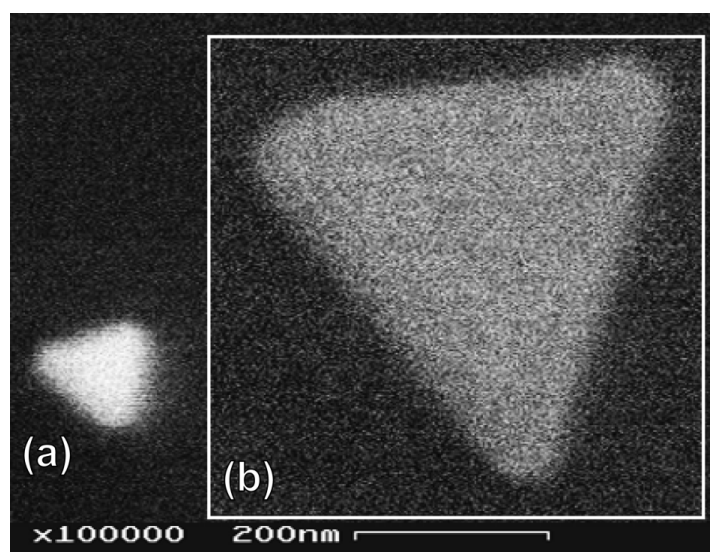
Figure 28: SEM micrographs[8] of triangular gold nanoplates with an edge length of about 100 nm (a) and 500 nm (inset b). Both images are of the same magnification (x100000). The height of the smaller particles is about 10-17 nm as confirmed by AFM measurements (data not shown). The sample contained mostly triangles as shown in (a). In addition, also smaller triangles of about 60 nm were found as well as very few hexagonal particles with an edge length of about 270 nm. Figure taken from reference [39].

The experimental scattering patterns of the triangular nanoplates were not homogenous in their shape (see Figure 29). The size variation in the sample probably holds responsible for these variations. Nevertheless, all the experimental patterns clearly differed from the ones observed for gold nanospheres or -rods. In most cases, distorted rings or spots occurred for azimuthally or radially polarized light, respectively. Taking into account the amount of particles with a size of 100 nm as determined by SEM measurements[8] and the occurrence of the most characteristic patterns, it appears to be fairly convincing to assign these patterns to particles in this size range. As mentioned above, the observed distortion appears to indicate the particle's orientation. Because scattering is expected to be stronger at the triangle's tips, a possible orientation is shown in the overlay in Figure 29 a, b.[39, 87] Additionally, also scattering patterns of triangular shape themselves were observed which were larger than the diffraction limited focal spot (see Figure 29 c, d). This

---

[8] SEM measurements were kindly performed by Elke Nadler with a Zeiss DSM 962.

indicates that the scattering object can no longer be considered as point-like. However, this could certainly be expected for a triangle with an edge length of 500 nm. Consequently, such larger particles render images much closer related to their actual physical topology.[39, 87]
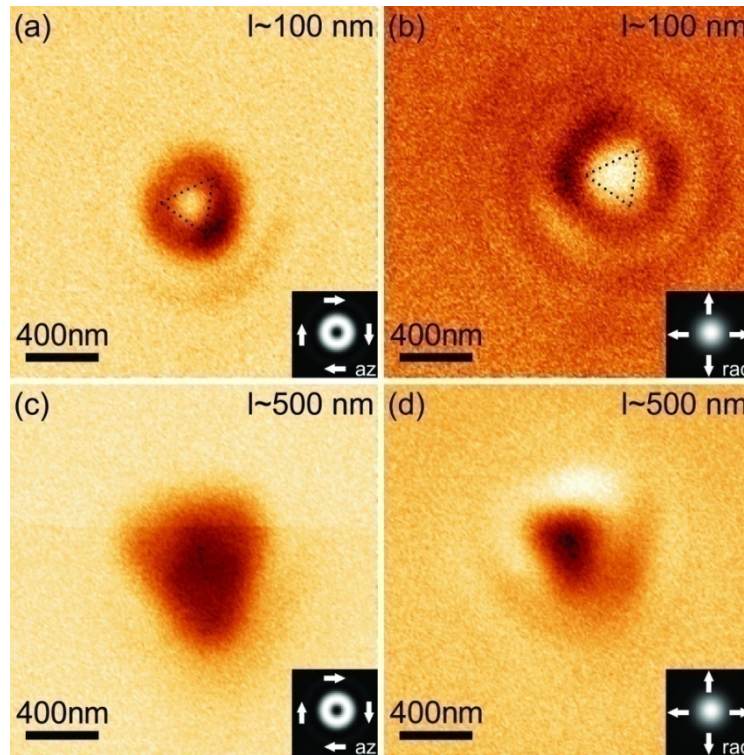
Figure 29: Scattering images of triangular gold nanoplates of two different sizes (APDM: left, RPDM: right at 514 nm. For the smaller particles, the observed patterns are highly distorted and qualitatively reveal the particle's displacement (probable orientation shown in the overlay). Larger particles render images closer to their topology. Figure taken from reference [39].

Confocal images of gold nanotriangles were also acquired collecting both the scattering and the PL signal of the particles, as shown in Figure 30 and Figure 31. Occasionally, large patterns were observed, showing a high, threefold symmetry when excited with azimuthally or radially polarized light, as can be recognized from Figure 30. This symmetry was especially pronounced for an APDM or in the luminescence mode of the RPDM (see Figure 30). Also striking is the somehow contrary intensity distribution in the luminescence patterns of the APDM and RPDM, respectively (cf. Figure 30 b, d). Surprisingly, the scattering patterns of the two modes do not show such a close resemblance (cf. Figure 30 a, c). The patterns

acquired in the conventional, linearly polarized Gaussian mode (LPGM) closer resemble a triangle and hence the particle shape, which might be expected for a large particle. The assumed particle orientation is given by the grey dotted triangle in Figure 30. Since these patterns show a FWHM of 615 nm in the LPGM, the physical dimensions are likely to be in this range as well. However, comparing the patterns shown in Figure 30, it seems convincing that the DMs image the SPs in the particle while the Gaussian beam rather visualizes the particle itself.
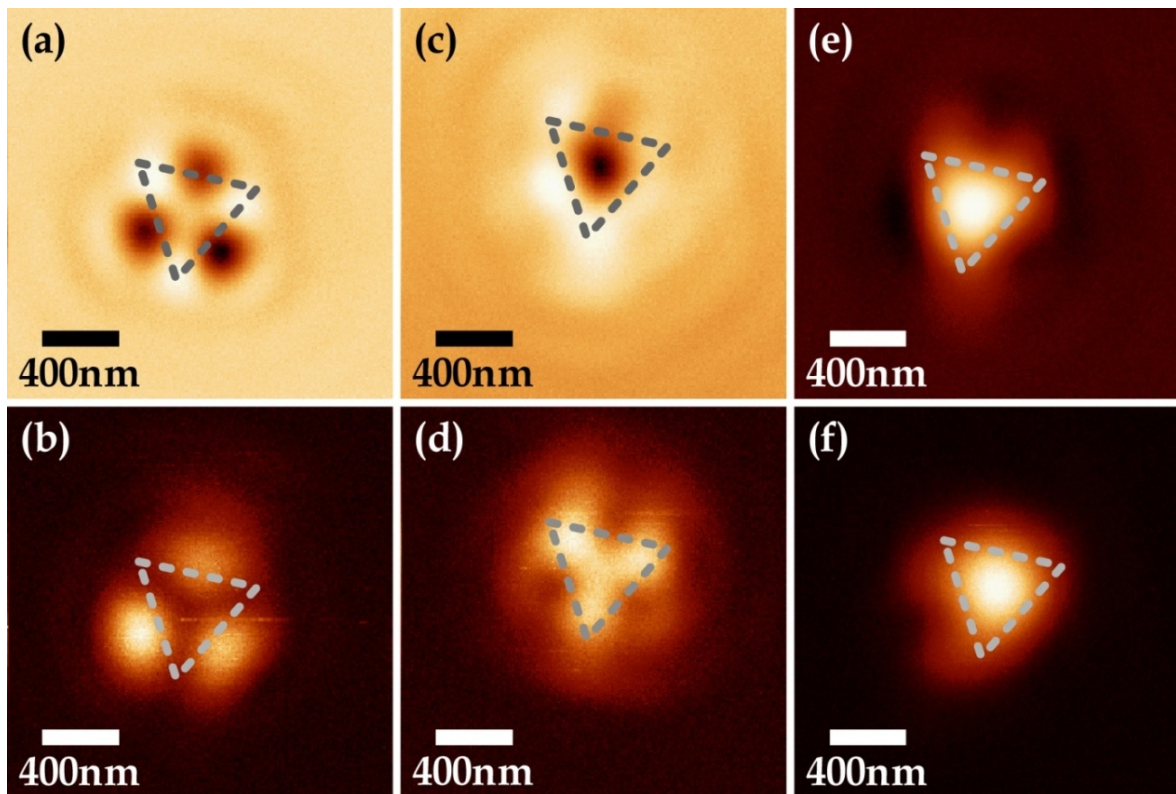
Figure 30: Confocal scattering (upper row) and PL (lower row) images of a single gold nanotriangle ((a, b) APDM, (c, d) RPDM, (e, f) LPGM at 633 nm). The probable particle orientation is indicated by the grey dashed lines. Please note that while the scattering patterns of the two DMs are remarkably different (a, c), the PL patterns (b, d) are somehow contrary in their intensity distribution. The different shape as compared to Figure 29 c, d suggests a larger particle size, supported by the $FWHM_{LPGM}$ of approx. 615 nm.

Additionally, *in situ* AFM measurements were undertaken in combination with the confocal measurements. Therefore, a Nanosurf® AFM (easyScan 2, Nanosurf AG, Liestal, Switzerland) was positioned on top of the confocal microscope. The alignment of the two microscopes is provided by a homebuilt piezo device as

described in chapter 3.4.3 (p. 46). An example is shown in Figure 31. The particle orientation cannot be determined with high accuracy since the scanning directions of the confocal microscope and the AFM are independent from each other. Nevertheless, the general scanning direction is the same, and the orientation can be measured although there might be a slight deviation. Such variations can be corrected for by comparing larger scan areas showing several particles in both the confocal and AFM data, however, in this case, it was not possible to acquire suitable AFM images. Nevertheless, as has been shown above, the approach is in general feasible.

Both the confocal scattering and PL data in Figure 31 show a pronounced asymmetry, that is, a clear deviation from the ring-shaped patterns found for spherical particles upon excitation with an APDM at 633 nm. As expected, comparing this asymmetry with the *in situ* AFM data, the particle orientation is directly imaged. For better visualization, the particle orientation is given by the grey dashed lines. The FWHM of the particle's edge length is 365 nm as measured with AFM, while the height is approximately 17 nm.
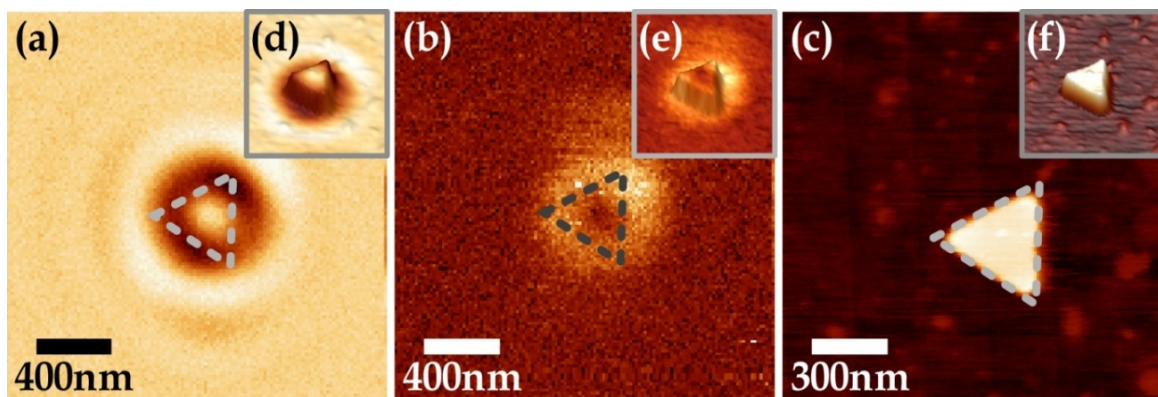
Figure 31: Confocal (a) scattering and (b) PL images of an individual gold nanotriangle (APDM at 633 nm) as well as corresponding (c) *in situ* AFM data (please note the slightly different scaling in c). The insets (d-f) show the AFM data as 3D representation with the optical data as colour code in d, e, showing the particle orientation which can also be recognized from the asymmetry in the optical patterns. The particle orientation is also indicated by the grey dashed lines. The FWHM of the triangle's edge length is 365 nm as measured by AFM, the particle height is 17 nm.

The insets in Figure 31 d-f give the AFM data as a 3D representation with the optical information as colour code in d, e. It can be clearly recognized that both the scattering and the luminescence is strongest at one tip of the particle. Comparing the scattering (and PL) images from the different triangular particles shown in Figure 29-Figure 31, the particle size seems to play a key role for the pattern shape. Obviously, the symmetry of the optical pattern dramatically depends on this measure, even in the relatively narrow size range between 100-600 nm when DMs are used for imaging. Therefore, it seems to be highly convincing that SPs are excited in the particles and mainly hold responsible for the image contrast.

In Figure 32, different confocal images of gold nanotriangles are shown. All particles were imaged upon excitation with an APDM (left), a RPDM (centre) and a LPGM (right) at 633 nm. Both the elastically scattered (upper rows) and the PL light (lower rows) was detected. Certain similarities in the patterns indicate that the particle size influences their shape. For example, the patterns in each row of Figure 32 are pretty comparable. Please also note that excitation with a LPGM, especially in PL, exclusively leads to spot-like patterns. Also in scattering, there is only little variation in the patterns' shape for a LPGM.

In general, the signal and image contrast were stronger and more stable in the scattering mode. The asymmetries observed in the patterns created upon excitation with an APDM should allow to determine the particle orientation as shown in Figure 31. Consequently, an APDM is an optimal choice to image the orientation of gold nanotriangles. Since a RPDM produces smaller patterns, it can be used to precisely localize the particles.

4.3 Confocal and in situ AFM Imaging of Single Gold Nanotriangles

APDM RPDM LPGM   APDM RPDM LPGM   APDM RPDM LPGM
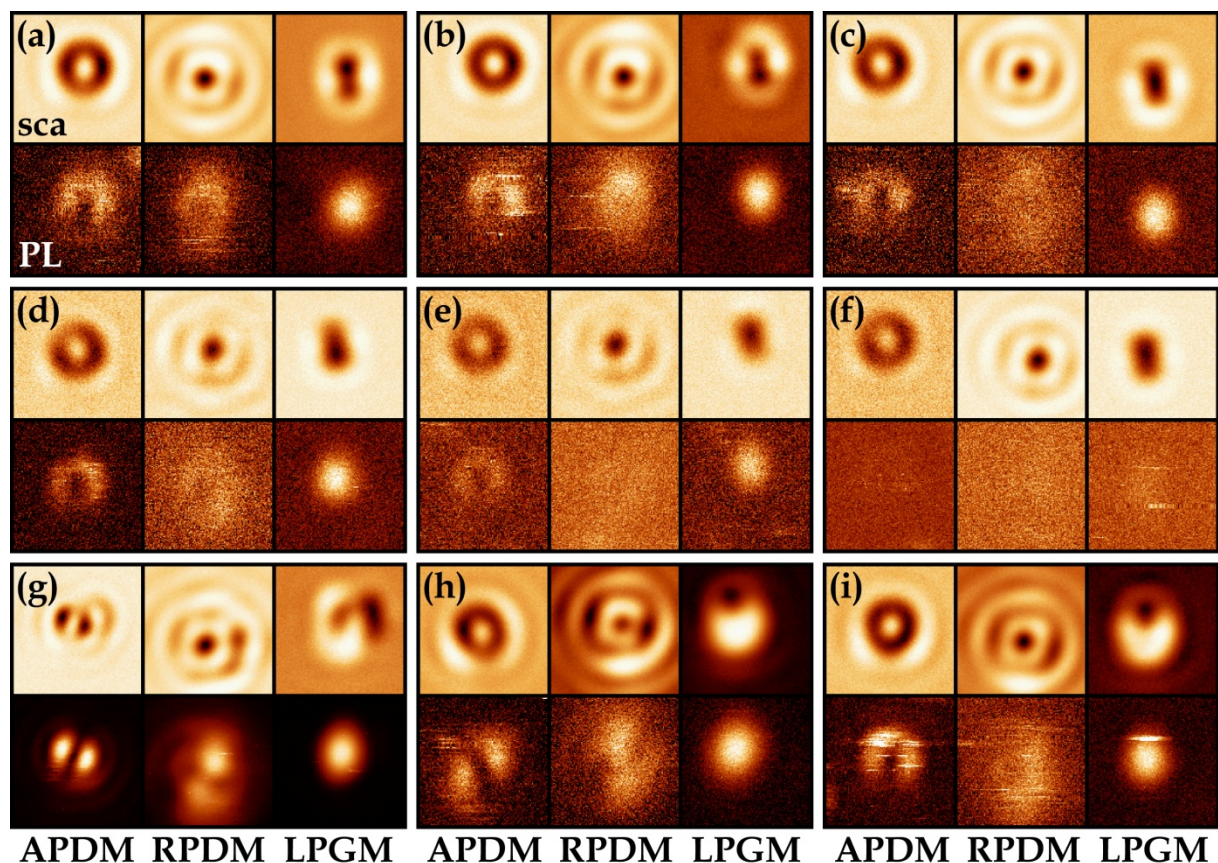
Figure 32: Confocal images of gold nanotriangles (APDM: left, RPDM: centre, LPGM: right at 633 nm), both in scattering (upper rows) and PL mode (lower rows). Similar patterns are sorted in rows, suggesting a strong particle size dependence. In most cases, scattering is much stronger than PL, provides a more stable signal and better image contrast. For a LPGM, the shape does not remarkably vary, especially for PL. The image size is $1.5 \cdot 1.5 \ \mu m^2$ in all cases.

In general, differently shaped particles can be distinguished by their varying scattering as well as PL patterns and the particle orientation is directly imaged for metallic nanorods and triangles as confirmed by *in situ* AFM measurements. In addition, for large gold nanotriangles, the special polarization properties of the DMs allow to visualize the SPs in the particles, which is not possible with a LPGM. This underlines that the presented technique offers a new gateway to additional information not directly accessible with standard confocal microscopy.

4.4 3D Orientation of Single Gold Nanorods in Scattering Mode

The 2D orientation of gold and silver nanorods can be determined with extraordinary high accuracy through the implementation of APDMs and RPDMs in confocal microscopy (cf. chapter 3.2.2, p. 36).[35, 36] In addition, also dynamic reorientations of the particles can be followed.[41] However, the splitting of the radial mode into both a transversal and a longitudinal polarization component upon focusing with a high *NA* microscope objective creates a 3D electric field distribution in focus. It has been shown that this special field distribution allows to determine the 3D orientation of single molecules.[163] Similar patterns are expected when a parabolic mirror is used as focusing element.[164] Since the field distribution is different to the one obtained with a microscope objective with comparable *NA*, the resulting emission patterns of the single fluorescent molecules also vary slightly. However, the 3D molecular orientation can be determined in both cases. Coming back to the 2D case, the resulting patterns for single fluorescent molecules and metal nanorods are pretty comparable in shape. For molecules, a linear dipole moment results in a two-lobed fluorescent pattern, while in the case of a metal nanorod the excitation of SPs along one particle axis leads to an anisotropic polarization of the particle. As a consequence, an induced dipole moment creates again a two-lobed pattern. For the 3D case, things are a little bit different, since the polarizability tensor comes into play,[37, 38] which is not any more directly comparable to the 2D dipole moment of a single molecule. However, it should still be possible to probe the 3D orientation of the particle, although the resulting patterns might be more complex than in the case of single dipoles.[87]

It is difficult to cross check the 3D orientation of the particles with a second technique, since there are not many methods available which allow to measure an arbitrary orientation of a nanoparticle in space. However, the 2D experimental scattering patterns of gold nanoparticles can be well simulated.[35, 36, 39, 40] Therefore,

the scattering patterns for different particle orientations were simulated, applying a simulation method developed from the pure 2D case.[9] The nice agreement between the experimental and simulated patterns allowed to infer the experimental 3D particle orientation from the simulated data. This applies for the data using both azimuthally and radially polarized light.

To obtain gold nanorods with an arbitrary 3D orientation, the particles were embedded in a spin coated polymer film of polyvinylalcohol (PVA) as described in chapter 0 (p. 57). A schematic of the sample is shown in Figure 33 a (not to scale). In order to determine the 3D orientation of a nanoobject, one can define two different angles, as shown in Figure 33 b while the Cartesian coordinate system is usually given by the sample plane (x, y) and the optical axis (z). The first angle ϕ gives the in-plane component, which lies in the sample plane. The second component determines the out-of-plane angle θ between the object and the optical axis z.
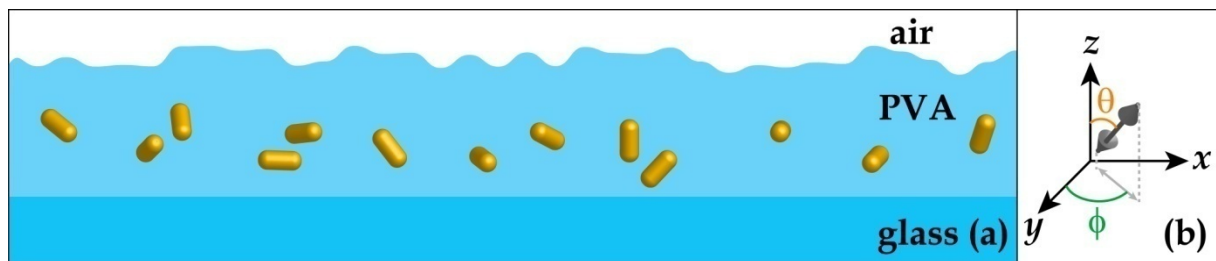
Figure 33: (a) Schematic of gold nanorods embedded in a polymer film of polyvinyl alcohol (PVA) with random 3D orientation (not to scale). The gold particles were spin coated from an aqueous polymer solution on glass cover slips (see chapter 0, p. **Fehler! Textmarke nicht definiert.**). (b) To define the 3D orientation of nanoobjects, two angles can be defined, the in-plane angle ϕ being parallel to the sample xy-plane and the out-of-plane angle θ between the object and the optical axis z.

It might be worth to shortly think about the patterns one would expect from gold nanorods with different orientations. For particles being parallel to the sample plane ($\theta = 90°$), two-lobed patterns are expected since their orientation is purely 2D. Another relatively easy to predict case are particles which are oriented parallel to the optical axis ($\theta = 0°$). When excited with an APDM, only their short axes can be

---

[9] All simulations were carried out by Dr. Antonio Virgilio Failla.

probed. Since the two transversal axes are equivalent for the gold nanorods, the particles are expected to behave similar to spherical particles, which also corresponds to their projection in the sample plane. Consequently, a doughnut-shaped pattern is to be expected. The radial mode, however, offers both a transversal and a longitudinal polarization component of different intensities. Since these two polarization components are oriented along the direction of the transversal and the longitudinal particle axes, they should allow to excite SPs along both directions. The resulting patterns should correspondingly feature a central spot with a surrounding ring with weaker intensity. One should also take into account that the excitation efficiency of the transversal SP at 633 nm is considerably lower than that of the longitudinal one.

4.4.1 Variety of Observed Scattering Patterns

Experimentally, different shapes of scattering patterns are indeed observed.[37, 38, 87] Apart from two-lobed patterns and rings, additional new types of patterns emerge (see Figure 34). Surprisingly, patterns of both negative and positive image contrast are found at the same time. As they are repeatedly observed in one and the same image, this phenomenon cannot be attributed to a focussing effect in a specific sample plane.
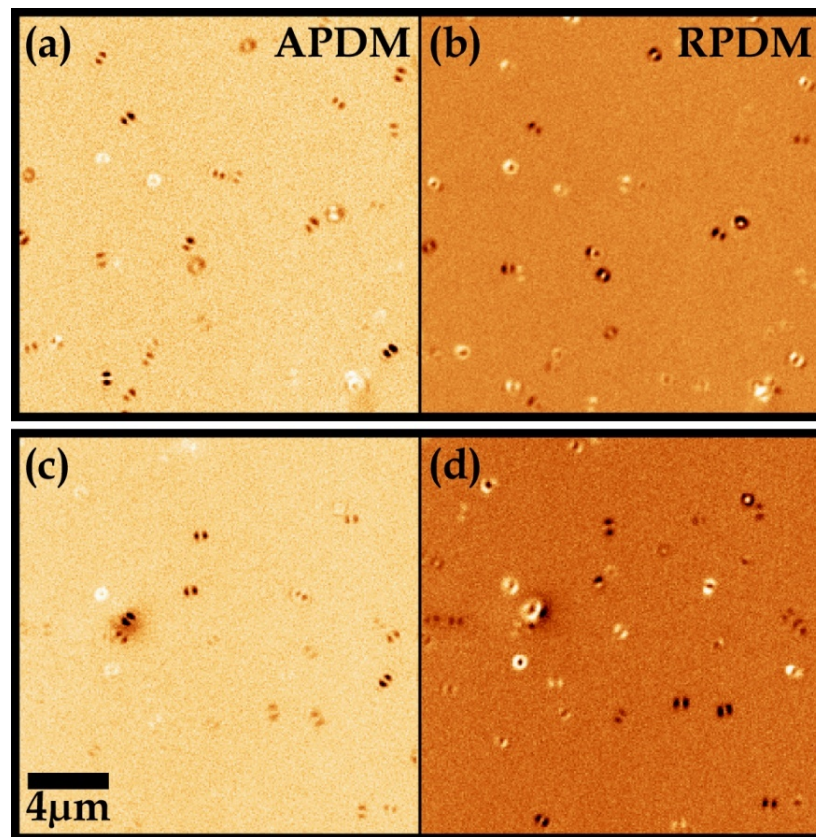
Figure 34: Scattering images (left: APDM, right: RPDM at 633 nm) of gold nanorods with random 3D orientation in a polyvinyl alcohol (PVA) film with adjusted image contrast. Differently shaped patterns are found, covering a range from two-lobed to ring-shaped. Additionally, both a negative and a positive image contrast is observed in one and the same image for different particles.

As can be recognized from Figure 34, patterns of negative and positive image contrast are observed upon excitation with both azimuthally and radially polarized light. For better visualization, the image contrast was slightly adjusted. Mostly, negative image contrast in both modes is found. Some particles experience a sign

inversion of the image contrast for either or both of the two modes. Generally, a positive image contrast is more often encountered when a RPDM is used for excitation. In more details, there are a number of particles which show a positive contrast in both modes as well as particles with a negative contrast in the azimuthal mode and a positive one in the radial mode. However, a positive contrast upon excitation with an APDM together with a negative contrast upon excitation with a RPDM was extremely rarely found.

Some more examples of both negative and positive contrast within one image are presented in Figure 35. Again, each sample area is shown upon excitation with azimuthally and radially polarized light, so for each case, a pair of two images results.
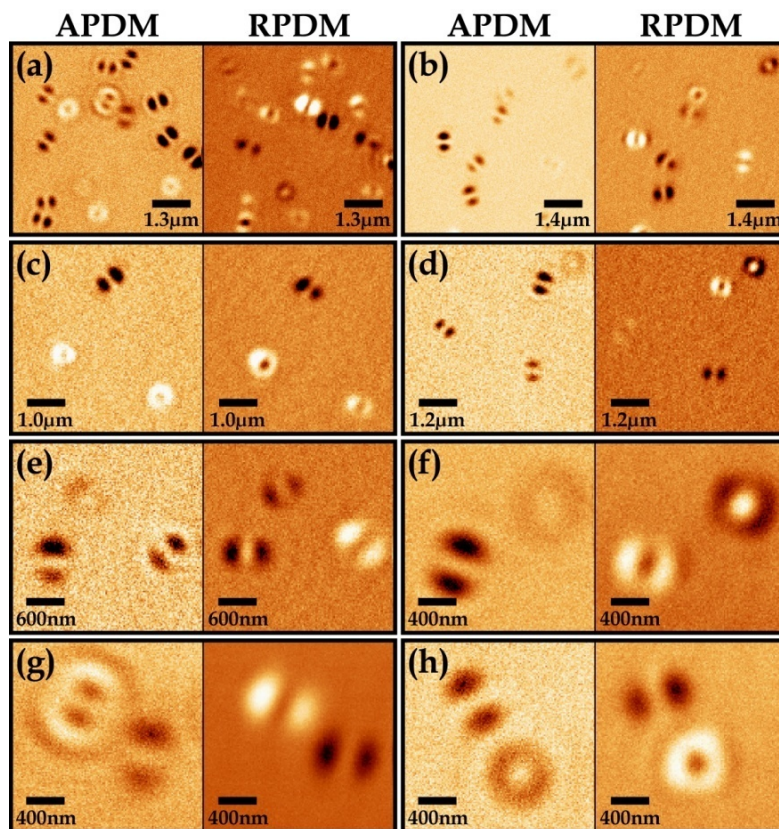
Figure 35: Scattering images (left: APDM, right: RPDM at 633 nm) of gold nanorods with random 3D orientation in a PVA film with adjusted image contrast. Differently shaped patterns are found, covering a range from two-lobed to ring-shaped. Both negative and positive contrast is observed in one and the same image for different particles.

4.4 3D Orientation of Single Gold Nanorods in Scattering Mode

Despite the remarkable differences in the patterns resulting for the two excitation modes, corresponding sample areas are still easily recognizable. However, in some cases, the shape of the patterns considerably changes for the two modes (see *e.g.* Figure 35 a, b). In addition, different contrast behaviours are found: negative contrast in both modes, positive contrast in both modes as well as negative contrast in azimuthal mode and positive contrast in radial mode. In order to analyze the different pattern shapes observed, the experimentally measured scattering patterns are presented in different categories according to the observed image contrast in the following. Since variations occur in either or both excitation modes, pairs of the experimentally found patterns are considered.

4.4.2 Negative Image Contrast in Both Modes

Examining the different scattering pattern pairs in more detail, frequently, a negative image contrast is observed in both modes as presented in Figure 36. Depending on the observed differences in either or both modes as compared to the pure 2D case, frequently encountered pattern pairs were sorted into sub-categories with increasing deviations from the 2D case (cf. Figure 36 a-d).
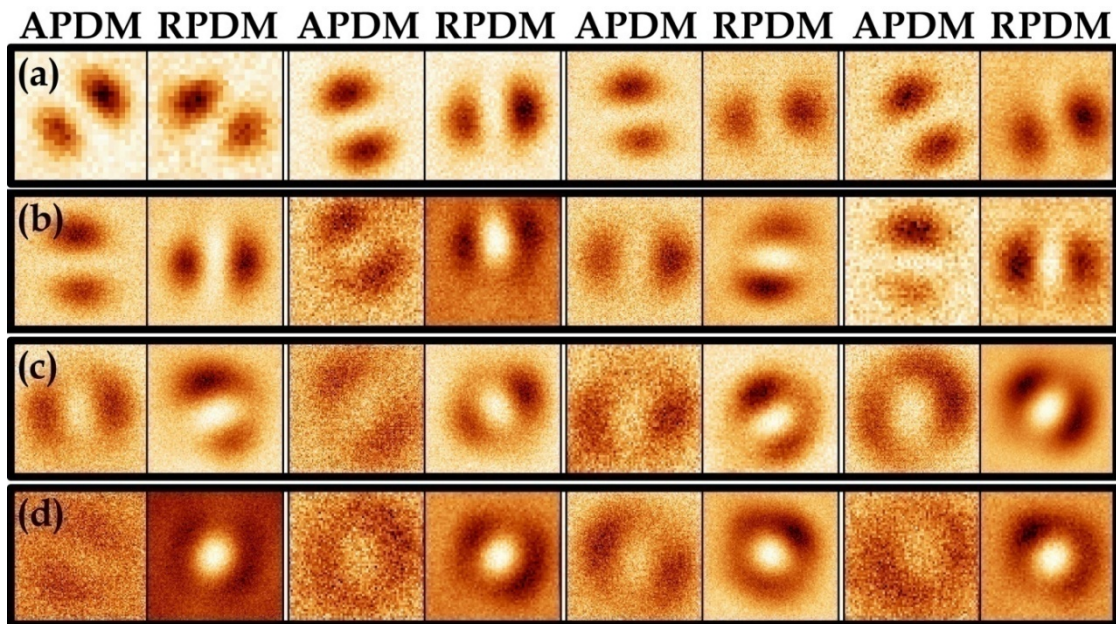
Figure 36: Scattering images (APDM and RPDM at 633 nm, image size $1 \cdot 1$ µm²) of gold nanorods with random 3D orientation in a PVA film. Negative image contrast was encountered in both modes. Due to variations in the pattern pairs, four different sub-categories are identified: (a) Patterns comparable to the pure 2D case, (b) additional bright central spots (RPDM), (c) elongated lobes (APDM, RPDM) with bright central spots (RPDM), (d) further elongated lobes forming almost ring-like patterns (APDM, RPDM) with bright central spots (RPDM).

Pattern pairs comparable to the pure 2D case in both modes are shown in Figure 36 a. For the other three sub-categories, an increasing variation is found: bright central spots upon excitation with a RPDM are observed (see Figure 36 b-d). In addition, the lobes become more and more elongated, finally resulting in ring-like structures. In Figure 36 c, elongation is primarily observed for an APDM, but already noticeable for the RPDM. Further elongation for both modes is depicted in Figure 36 d. In general, the image contrast tends to decrease with lobe elongation upon excitation with an APDM.

4.4.3 Positive Image Contrast in Both Modes

Positive image contrast in both excitation modes was also observed, as presented in Figure 37. Again, elongation of the lobes to more or less ring-like patterns takes place in both modes, allowing to establish sub-categories. In most cases, RPDM patterns feature a dark central spot.
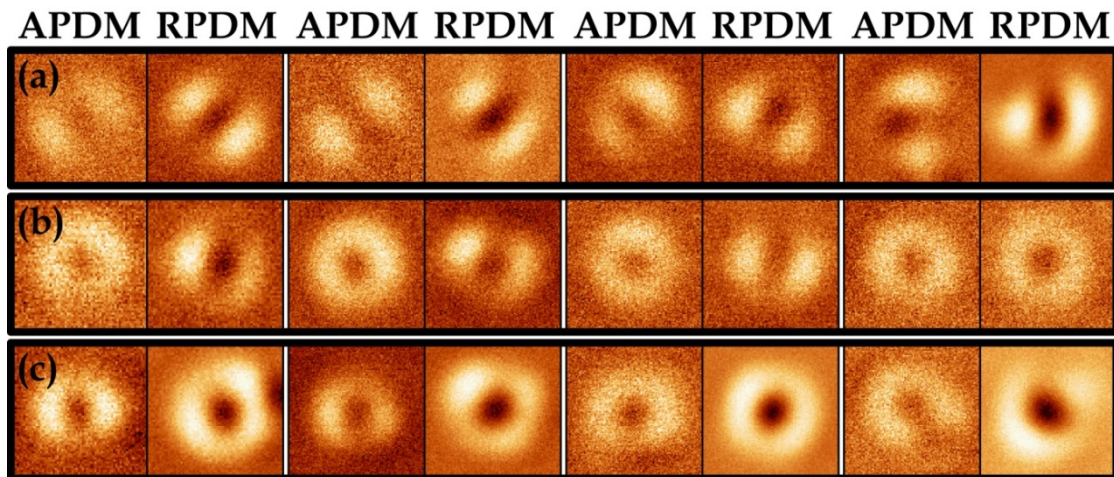
Figure 37: Scattering images (APDM and RPDM at 633 nm, image size $1 \cdot 1$ µm²) of gold nanorods with random 3D orientation in a PVA film. For both excitation modes, a positive image contrast is found with a dark central spot for a RPDM in most cases. Due to variations in the pattern pairs, three different sub-categories are identified: (a) Two-lobed patterns in both modes, (b) elongated lobes (APDM: forming almost ring-like structures), less prominent dark central spots (RPDM), (c) elongated lobes (RPDM: forming almost ring-like structures).

For positive image contrast observed in both modes, the two-lobed shape is less frequently encountered. Mainly, it is accompanied by a dark central spot for a RPDM (see Figure 37 a). Elongation of the lobes to ring-like patterns is found regularly (see Figure 37 b, c). In Figure 37 b, ring-like structures are observed for the APDM while the two-lobed patterns of the RPDM show a less prominent dark central spot. Elongated two-lobed APDM patterns are accompanied by almost ring-like RPDM structures with dark central spots in Figure 37 c.

4.4.4 Negative and Positive Image Contrast

Patterns with different image contrasts in the two modes were also observed (see Figure 38). A negative contrast upon excitation with azimuthally polarized light was found while patterns with a positive image contrast were observed under excitation with a RPDM. Again, variations in the pattern pairs allow sorting into sub-categories (see Figure 38 a-d). Frequent occurrence of a positive contrast for an APDM together with a negative contrast for a RPDM was not found.
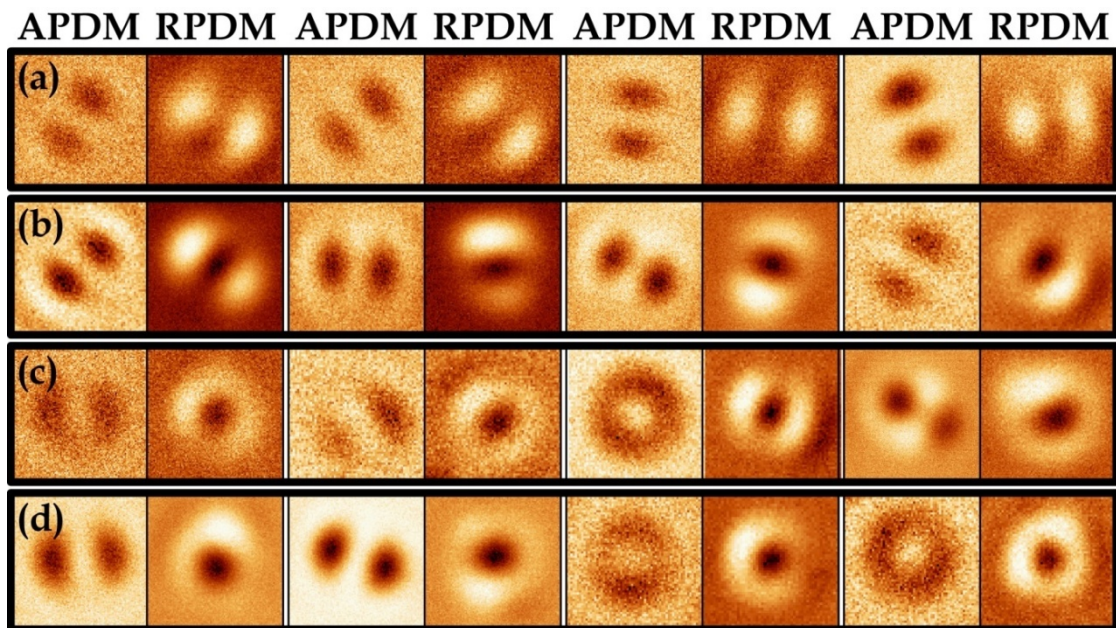
Figure 38: Scattering images (APDM and RPDM at 633 nm, image size $1 \cdot 1$ µm²) of gold nanorods with random 3D orientation in a PVA film. A combination of negative (APDM) and positive (RPDM) contrast is found. Due to variations in the pattern pairs, four different sub-categories are identified: (a) Patterns comparable to the pure 2D case despite contrast inversion (RPDM), (b) two-lobed patterns in both modes with additional bright features (APDM) and dark central spots (RPDM), (c) elongated lobes with dark central spots (RPDM), (d) further elongation forming almost ring-like patterns with dark central spots (RPDM). The APDM patterns vary from clearly two-lobed to ring-like structures in (c, d). Occasionally, a transient pattern resembling a shamrock of mixed contrast is observed for an APDM (cf. last pair in (c)).

For a number of particles, the two-lobed shape in both modes is again comparable to the 2D case. However, upon excitation with a RPDM, the image contrast is inverted (see Figure 38 a). Variations in the pattern contrast are observed in Figure 38 b: for both modes, the two-lobed patterns feature regions of inverted contrast exceeding

4.4 3D Orientation of Single Gold Nanorods in Scattering Mode

the background (APDM: dark lobes with bright features, RPDM: bright lobes with dark central spot) while the overall shape of the lobes is hardly affected. An elongation of the two lobes for a RPDM is frequently found (see Figure 36 c), together with a dark central spot. Further elongation leads to almost ring-like structures (see Figure 36 d). The respective patterns for an APDM in Figure 36 c, d vary from two-lobed to ring-like, occasionally showing a somehow transient pattern resembling a shamrock of mixed contrast (cf. last pair in Figure 36 c). Such variations observed in one mode only might indicate that the two modes differ in their sensitivity on orientational changes in a certain angular range.

Recapitulating the results presented from the particles embedded in a polymer film of PVA with random 3D orientation, a variety of scattering patterns is found. Changes occur both in shape and image contrast. Therefore, pattern pairs were first treated according to image contrast in order to evaluate differences in the shape. Regardless of image contrast, a general shape variation occurs. Starting from two-lobed patterns, an elongation of the lobes finally results in ring-like patterns for both modes and all contrast combinations. Additionally, patterns of mixed contrast are found: for a RPDM, mainly a prominent central spot occurs. Mixed contrasts are less frequently observed for an APDM and are in general less prominent. However, these transitions do not coincide for the two modes which might indicate a different angular sensitivity.

4.4.5 Comparison to Simulated Data

In order to relate such different categories to a 3D particle orientation, the experimental data was compared to simulated scattering patterns. Best agreement was found with simulations for $R = 2.7$ (in fair agreement with the experimentally found $R = 2.6$, see Figure 39).
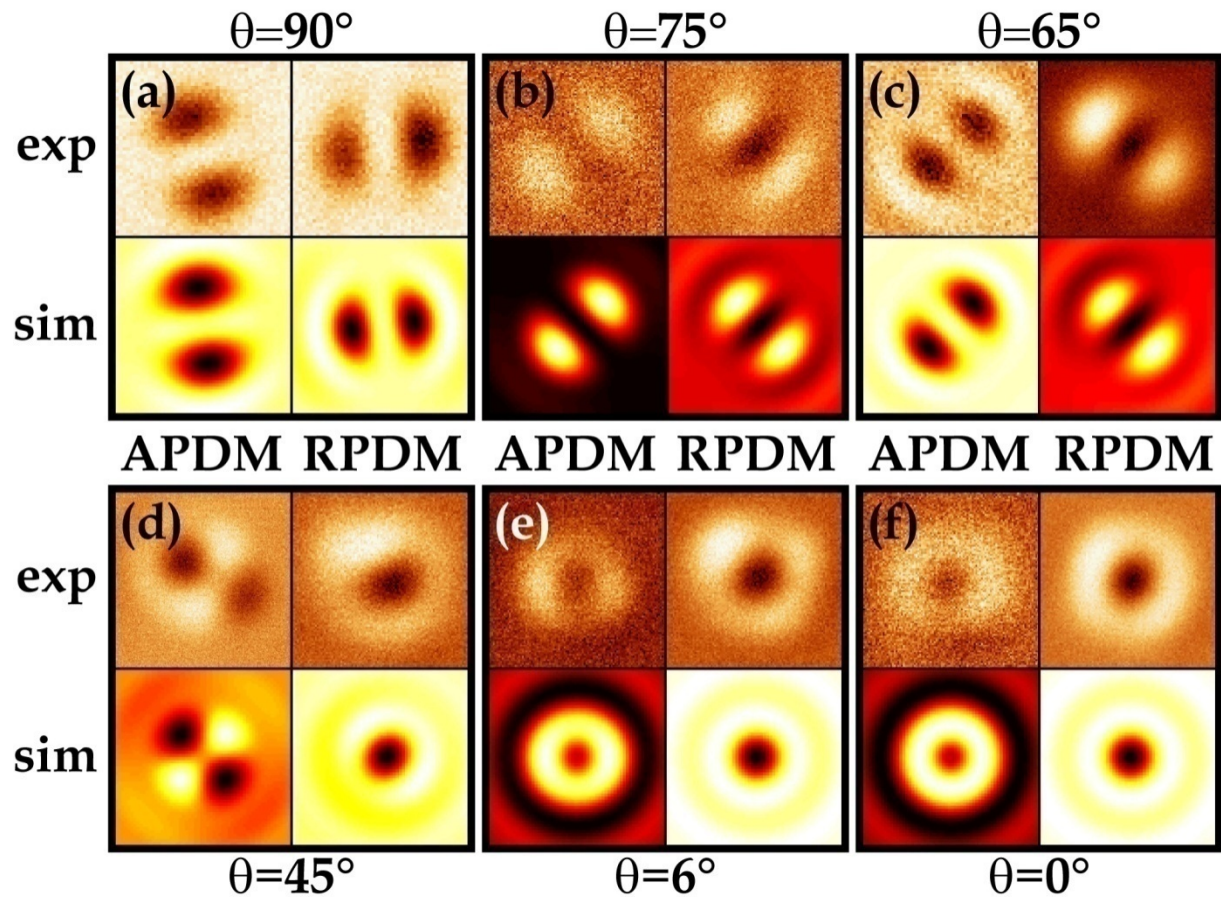
Figure 39: Experimental scattering (upper row) and theoretically predicted (lower row) patterns of gold nanorods with random 3D orientations embedded in a PVA film (APDM, RPDM at 633 nm, image size $1 \cdot 1$ µm²). The values given for the polar angle θ are the parameters from the respective theoretical simulations. In general, a nice agreement between the experimental and the theoretical data[10] is observed. For the simulations, $R = 2.7$ was used as a parameter, in fair agreement with the experimentally found mean value of $R = 2.6$.

4.4 3D Orientation of Single Gold Nanorods in Scattering Mode

In general, the simulations show a sensitive dependence of the scattering patterns on R, mainly regarding image contrast. This explains that not all experimentally found pattern pairs can be reproduced with a single set of simulated data[10]. However, the general feasibility to extract the 3D particle orientation can be easily recognized.

For particles with in-plane orientation ($\theta \approx 90\,°$), two-lobed patterns are observed, as they are found for particles with a purely 2D orientation (see Figure 39 a). With a slight inclination out of the sample plane ($\theta \approx 75\,°$), the two-lobed patterns change: in both modes, the contrast becomes positive and for a RPDM, a dark central spot emerges (see Figure 39 b). For further inclinations ($\theta \approx 65\,°$), the image contrast of the pattern in the azimuthal mode changes back to a negative contrast with surrounding bright areas of positive contrast (see Figure 39 c), while the pattern for a RPDM hardly changes. An intermediate pattern shape is found for an APDM and $\theta \approx 45\,°$, accompanied by a bright ring with a dark central spot in the RPDM (see Figure 39 d). For (almost) upright particles, the patterns become ring-shaped (APDM and RPDM), together with a dark central spot (RPDM, $\theta < 10\,°$, see Figure 39 e, f). The main pattern types and their evolution are also summarized in Table 7.

---

[10] All simulations were carried out by Dr. Antonio Virgilio Failla.

Table 7:   The experimentally found pairs of scattering patterns for particles with a random 3D orientation can be categorized by their shape and their image contrast as shown in Figure 39. The polar angle θ can be determined from the theoretical simulations.

Figure 39	pattern shape		main image contrast		polar angle θ
	APDM	RPDM	APDM	RPDM	from simulations
(a)	two-lobed	two-lobed	negative	negative	90 °
(b)	two-lobed	two-lobed, dark central spot	positive	positive	75 °
(c)	two-lobed	two-lobed, dark central spot	negative	positive	65 °
(d)	shamrock	ring, dark central spot	mixed	positive	45 °
(e)	elongated lobes/ (almost) ring	ring, dark central spot	positive	positive	6 °
(f)	ring	ring, dark central spot	positive	positive	0 °

Through the combination of images upon excitation with azimuthally and radially polarized light, the 3D orientation of gold nanorods can be determined by comparing the experimental scattering data with theoretically simulated patterns, as demonstrated exemplarily in Figure 39. The two modes show a different angular sensitivity which perfectly complement each other. While the APDM appears to be more sensitive for changes of small θ, the RPDM seems to react stronger on changes of large θ. The experimentally observed variations in image contrast may largely be attributed to size variations of the individual particles, as supported by the simulated data. For smaller particles with a SP resonance further shifted from the excitation wavelength, such variations in image contrast was not observed.[37, 38] Hence, the comparison to simulated data is facilitated and further supported by PL data.

Patterns of totally different shape and symmetry than in the pure 2D case were regularly observed. This frequent occurrence of the same type of patterns rules out clusters as the source of these scattering patterns since it is highly unlikely that

several particles would form symmetric and uniform agglomerates reproducibly. In addition, all patterns were diffraction limited and consequently have to be caused by a scatterer which can be considered as point-like compared to the PSF in focus. Taking into account the size of a single gold nanorod of about 15-20 nm · 38-50 nm, clustering, if occurring at all, can only involve a few particles. However, almost all observed patterns showed an extremely high symmetry, indicating that the symmetry of the responsible scatterer has to be high as well. Consequently, if clustering should have occurred, it would have to be highly symmetric like *e.g.* particles sticking together side by side, end-to-end or forming a cross. Although we cannot be absolutely sure about clustering in the polymer film, AFM measurements on 2D samples were undertaken, where the gold nanorods were spin coated on a glass cover slip and exposed to air. For these measurements, even when dramatically increasing the concentration of the particle solution compared to the standard sample preparation for confocal microscopy, particle aggregation was not observed. These results were also confirmed with *in situ* AFM data in direct combination with the confocal measurements.[36, 39] Likewise, only single, spatially isolated particles were found and clustering could not be observed.

5   Sensing with Gold Nanorods

5.1   Particles at Dielectric Interfaces with Different Refractive Properties

The optical properties of the sample interface might play a key role in the image acquisition process. To study this influence, images of gold nanorods at different interfaces were acquired. For better comparison, the same sample area was imaged in each case. First, the particles were examined at a glass-air interface. In a second step, water was deposited on the glass surface, producing a glass-water interface. After evaporation of the water, the glass-air interface was restored and in most cases, images were acquired. Finally, immersion oil was used to reach index matching conditions. Therefore, three different interfaces, glass-air, glass-water and glass-oil, were compared with a decreasing refractive index mismatch. An exponential increase of both the particle's scattering intensity and the signal-to-background ratio is found approaching index matching conditions. While the shape of the pattern remains unchanged, the sign of the image contrast also depends on the refractive properties at the sample interface.[40]

5.1.1 Particles Sensing the Interface

The same set of gold nanorods (upon excitation with an APDM at 633 nm) at three different interfaces is compared in Figure 40. The respective sample configuration is schematically shown at the top. The confocal images were recorded consecutively, first, the particles were imaged at a glass-air interface as shown in Figure 40 a. Afterwards, the sample was covered with water (glass-water interface) and the image in Figure 40 b was recorded. After evaporation of the water, immersion-oil was finally added to create an index matched glass-oil interface (see Figure 40 c).
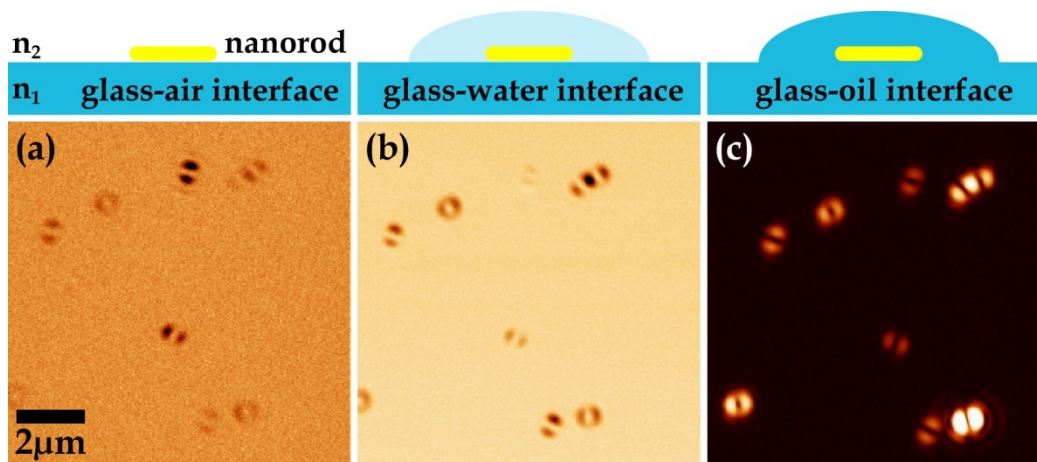
Figure 40: Scattering images of the same set of gold nanorods (APDM at 633 nm) at three different interfaces as indicated schematically at the top (a: glass-air, b: glass-water, c: glass-oil). The different refractive properties of the sample interface dramatically influence the image quality, improving with decreasing refractive index mismatch. Please note that the relatively poor signal-to-background ratio in (a) is already sufficient to determine the orientation with a precision of about 1°, therefore representing the technique's limit. Consequently, working with samples with higher refractive indices, both the acquisition time and the laser power could be reduced without sacrificing accuracy. The contrast inversion in (c) is due to differences in the signal formation process (see eq. 5.41, p. 101).

The most striking difference in Figure 40 is the improvement in the overall image quality or contrast with the changing optical properties of the sample interface. Although the particles are clearly visible in all three images, the contrast or signal-to-background ratio is better under aqueous or index matching conditions. However, the relatively poor image quality at the glass-air interface (see Figure 40 a) is already good enough to determine the orientation with a precision of about 1°,[35] therefore

representing the technique's accuracy limit. Consequently, an improved image contrast is an unnecessary luxury and the acquisition time can be considerably shortened. Additionally, the laser excitation power could also be reduced, which is especially interesting for light-sensitive samples. The contrast inversion for index matching conditions at the glass-oil interface (see Figure 40 c) is due to a change in the signal formation process. This will be discussed in the following in more detail (see also eq. 5.41, p. 101).

To analyse this qualitative impression in more detail and how it is caused by the image acquisition process, scattering images of the same set of gold nanorods at the three different interfaces (glass-air, glass-water and glass-oil) are compared in Figure 41, the respective interface is indicated in the schematics at the top. The refractive index of the sample substrate, n_{glass} = 1.518, remained unchanged. Only the refractive index of the embedding medium varied: for the glass-air interface n_{air} = 1 (see Figure 41, left), the glass-water interface n_{water} = 1.34 (see Figure 41, centre) and the glass-oil interface n_{oil} = 1.518 (see Figure 41, right). A weak remaining reflection still allowed for manual focusing at the sample interface. Depending on the optical properties of the respective interface, the interplay of the reflected field $\mathbf{E}_{ref}$ and the scattered one $\mathbf{E}_{sca}$ changes, as discussed in chapter 3.2.1 (see p. 35), and so does the image contrast.

5.1 Particles at Dielectric Interfaces with Different Refractive Properties
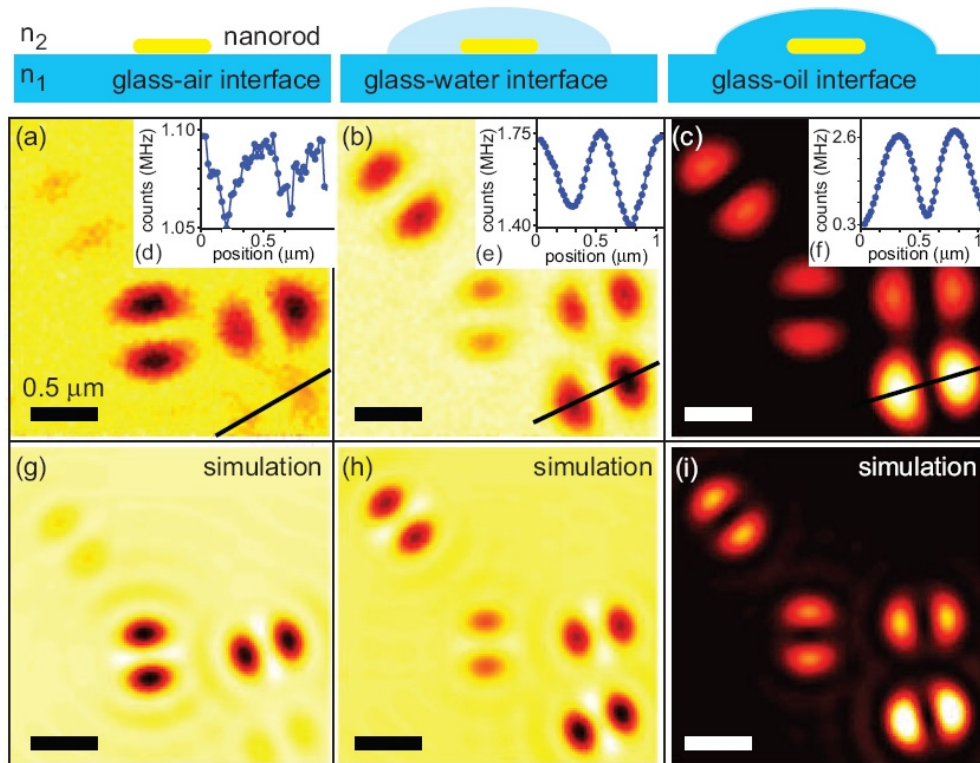
Figure 41: Experimental (a-c) and corresponding simulated (g-i) scattering images of the same set of individual, spatially isolated gold nanorods (aspect ratio R = 2.6, APDM at 633 nm) imaged for three different interfaces as indicated in the schematics at the top. (d-f) Scattering intensity profiles taken along the lines in (a-c), respectively. The simulations account for the contrast of the experimental scattering patterns. Figure taken from reference [40].

The cross-sections taken along the black lines in Figure 41 a-c are depicted in the profiles in Figure 41 d-f and indicate dramatic changes in the signal-to-background ratio for the three different dielectric environments. The strong variations in the image contrast which have been already outlined qualitatively for Figure 40 are also obvious. Approaching index matching conditions, the signal-to-background ratio as well as the image contrast increase with a final sign inversion for the contrast. More generally speaking, this can also be recognized in an improved image quality. Please note that the shape of the patterns remains basically untouched for the different interfaces. The signal amplitude, position and orientation of the single particles as

well as their relative distances were extracted with a 2D fit algorithm[11]. For the orientation, a standard deviation of approximately 1 ° was found. The particle positions could be extracted with nanometre accuracy and relative errors below 1 %. The extracted parameters were used for the theoretical simulations of the scattering patterns as shown in Figure 41 g-i. Both the particles' orientation and their position remained unchanged during the entire experiment within the experimental accuracy.[40]

For the three interfaces discussed here, considerable differences in the image quality can be recognized from Figure 41 since the dielectric interface plays a key role in the image acquisition process. At the glass-air interface, the excitation field is strongly reflected due to the considerable refractive index mismatch and dominates the images acquisition process. Regarding total internal reflection (TIR), the critical angle ϑ_{TIR} can be derived from Fresnel's law:

$$\vartheta_{TIR} = \arcsin \frac{n_2}{n_1},$$
(5.40)

in this case, 41 ° for the glass-air interface and 62 ° for the glass-water interface. The opening angle of the microscope objective used in this work (*NA* = 1.25, immersion oil) equals 55 °. Hence, TIR only occurs at the glass-air interface. As a consequence, comparing the glass-air and the glass-water interface, more light is transmitted at the latter interface and the prominence of $\mathbf{E}_{sca}$ in the signal is enhanced. The lower reflectivity of the glass-water interface also decreases the BG intensity and further increases the impact of $\mathbf{E}_{sca}$ on the signal. The decreased BG intensity allows the use of higher laser powers without damaging the detector, resulting in a better image contrast. Additionally, the acquisition time can be considerably shortened. Alternatively, dealing with light-sensitive samples, aqueous environments allows for lower excitation intensities without sacrificing image quality, sensitivity or accuracy. The enhanced contribution of $\mathbf{E}_{sca}$ in the image acquisition process improves the

---

[11] The 2D fit algorithm was developed by Dr. Antonio Virgilio Failla using a Matlab® code.

image quality at the glass-water interface. At the glass-oil interface, reflection of the incident light is negligible, resulting in the scattered light from the particle governing the detected signal. Consequently, the image acquisition is not any longer formed by interference but almost solely the scattered field is detected. Usually, a negative image contrast was observed at glass-air and glass-water interfaces, while an inversion of the image contrast occurred at the glass-oil interface.[40] However, due to interference, such a positive image contrast might also occur at glass-air and glass-water interfaces. The image quality is further improved for index matching conditions. Hence, either the excitation intensity or the integration time can be further reduced, again without losing image quality, sensitivity or precision. For very week scattering signals, the interferometric nature of the signal under non-index matching conditions might allow a higher sensitivity to detect very weak signals.

In general, the image contrast is given by the interplay of the reflected field $\mathbf{E}_{ref}$ and the scattered one $\mathbf{E}_{sca}$ at the different interfaces and can be described in the following way:[40]

$$I_{nano} = I_{det} - I_{BG} = 2\left|\mathbf{E}_{ref}\right|\left|\mathbf{E}_{sca}\right|\cos\varphi \quad \text{if } \left|\mathbf{E}_{ref}\right| >> \left|\mathbf{E}_{sca}\right| \tag{5.41}$$

$$I_{nano} = \left|\mathbf{E}_{sca}\right|^2 + 2\left|\mathbf{E}_{ref}\right|\left|\mathbf{E}_{sca}\right|\cos\varphi \qquad \text{if } \left|\mathbf{E}_{ref}\right| \approx \left|\mathbf{E}_{sca}\right| \tag{5.42}$$

$$I_{nano} = \left|\mathbf{E}_{sca}\right|^2 \qquad\qquad\qquad \text{if } \left|\mathbf{E}_{ref}\right| << \left|\mathbf{E}_{sca}\right|. \tag{5.43}$$

Equation 5.41 is valid if the reflection at the interface is stronger than the scattering, which is the case at the glass-air interface. In this case, the image contrast is mainly given by the interference term. Reducing the refractive index mismatch, less light is reflected at the interface and hence the intensity of the BG decreases. At the same time, the light scattered by the particles becomes more prominent. As a consequence, both the scattered light and the interference term compete in the image acquisition process, as described in eq. 5.42, which might be applied to the glass-air interface. The signal is still formed by interference, but considerably influenced by the scattered field as can be recognized from the differences between Figure 41 a, b.

Finally, for index matching conditions at the glass-oil interface, the BG and the interference term vanish and only the scattered field is detected (see eq. 5.43). [40]

To further investigate the influence of $\mathbf{E}_{ref}$, the BG intensity was measured for the three discussed interfaces as a function of the laser excitation power as shown in Figure 42.
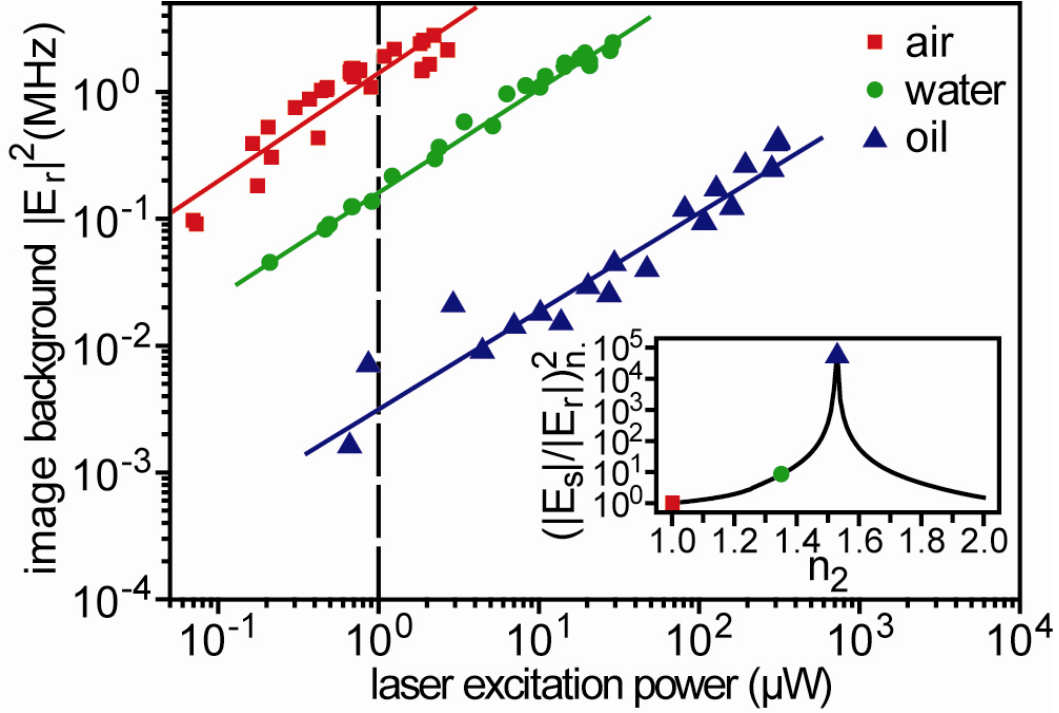
Figure 42: Measured BG intensity $|\mathbf{E}_{ref}|^2$ as a function of the laser excitation power ($\lambda = 633$ nm) for the three different interfaces glass-air (squares), glass-water (circles) and glass-oil (triangles). The lines represent linear fits to the respective data sets. (Inset) Relative nanorod scattering intensity $(|\mathbf{E}_{sca}|/|\mathbf{E}_{ref}|)^2$ (normalized with respect to $(|\mathbf{E}_{sca}|/|\mathbf{E}_{ref}|)^2$ for $n_2 = 1$) as a function of the refractive index n_2. Figure taken from reference [40].

As expected, a linear dependence is found for each interface. For a given laser power (as indicated by the dashed vertical line in Figure 42), the BG intensity reaches a minimum for the glass-oil interface while the values are two (three) orders of magnitude larger for the glass-water (glass-air) interface. The contribution of $\mathbf{E}_{sca}$ to the detected intensity $(|\mathbf{E}_{sca}|/|\mathbf{E}_{ref}|)^2$ increases exponentially over five orders of magnitude from the glass-air to the glass-oil interface. This theoretically calculated dependency is shown in the inset in Figure 42, where the values are normalized to the case of the glass-air interface. As a consequence, the image contrast is expected to

improve while decreasing the refractive index mismatch at the interface. For index matching conditions, the reflection finally vanishes leading to a sign inversion of the image contrast. The experimental results fully coincide with these expectations. [40]

5.1.2 The Interface Sensing the Particles

After having a closer look at gold nanoparticles at different interfaces and the respective changes on their image contrast, it might be interesting to change the perspective and investigate what the interface can tell about the particles.

5.1.2.1 Particle Geometry and Image Contrast

Carefully analyzing the scattering images in Figure 41 reveals variations in the relative signal amplitudes of the four particles at the three interfaces: while clear differences in the intensities are found at the glass-air interface, they become more balanced at the glass-water and glass-oil interface where only the particle in the lower right corner shows a different intensity. For index matching conditions, the image contrast results almost exclusively from E_{sca}. As a consequence, the pattern intensity mainly depends on the respective particle's plasmonic properties and therefore its size or aspect ratio R. To further visualize this dependency, the calculated integrated scattering intensity is shown as a function of R in Figure 43. [40]
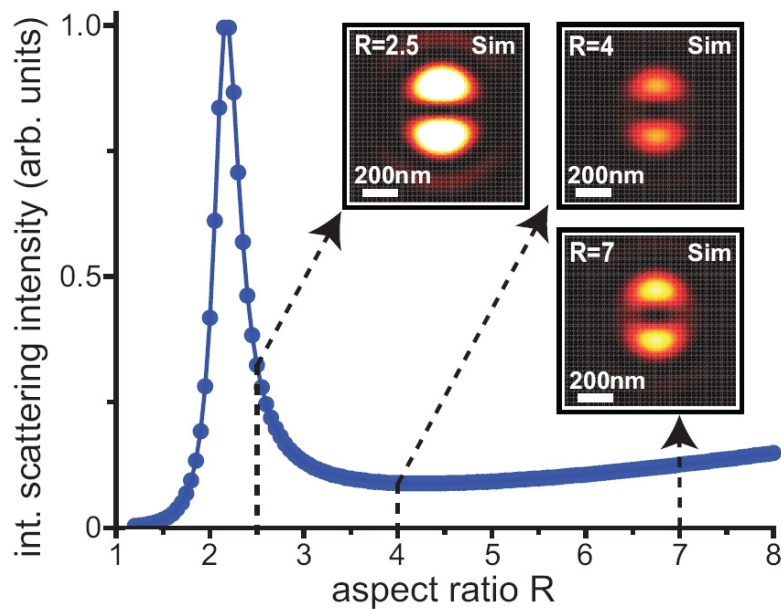
Figure 43: Integrated scattering intensity of a gold nanorod as a function of the aspect ratio R ($\lambda = 633$ nm), calculated assuming a constant nanorod width b of 15 nm as well as refractive index matching conditions $n_2 = n_1$ (*i.e.* the particle is located at a glass-oil interface, see also Figure 41). (Insets) Corresponding scattering patterns of gold nanorods simulated for $R = 2.5$, 4 and 7, respectively. The intensity scale is optimized for $R = 7$ and valid for all three images. Figure taken from reference [40].

In general, the scattering intensity moderately increases with the particle volume. However, when the particle's plasmon resonance overlaps with the laser excitation wavelength, a sharp maximum is found, as can be recognized from Figure 43 ($R = 2.1$, $\lambda = 633$ nm, index matching conditions). Three representative scattering patterns for aspect ratios $R = 2.5$, 4 and 7 have been simulated in Figure 43. The smallest particle, which comes closest to the experimentally found aspect ratio of $R = 2.6$, results to be the most intense one (please note that all three images have the same intensity scale optimized for $R = 7$). Consequently, the differences in the experimental scattering images can be attributed to slight variations in the particle size which drastically influence the scattering intensity when the plasmon resonance is close to the laser excitation wavelength. Surprisingly, the most intense particle in Figure 43 c is expected to be slightly smaller than the average because of its spectral SP properties. The size effect is most prominent at the glass-oil interface. In principle, a similar relative intensity distribution should be observed at the other two

interfaces. However, the experimental findings are different, especially at the glass-air interface (see Figure 41 a). For non-index matching conditions, this can be attributed both to a weaker impact of $\mathbf{E}_{sca}$ on the detected signal and influences of the particles' direct environments affecting the phase relation φ and hence the interference part of the image contrast. Additionally, the embedding medium also shifts the SP resonance relatively to the laser excitation wavelength. Close to the resonance frequency and taking into account the steepness of the scattering intensity distribution, even such slight variations can have a considerable influence on $\mathbf{E}_{sca}$. Therefore, under index matching conditions, the size of an individual gold nanorod can be expected to have a higher influence on the detected intensity while the dependence of the direct environment is negligible. At the glass-air and glass-water interfaces, both phenomena are entangled in the image contrast and for different particles, either enhancement or (partial) compensation might occur.

Another example is presented in Figure 44, where a sample area is depicted showing a total of six gold nanorods upon excitation with an APDM at 633 nm at different interfaces. Additionally, after evaporation of the water, a second set of images at the restored glass-air interface was acquired. The first row in Figure 44 shows an overview of all six particles while the second and third row provide close-ups of three particles per image. The intensity scale was optimized for each image individually.

5.1 Particles at Dielectric Interfaces with Different Refractive Properties
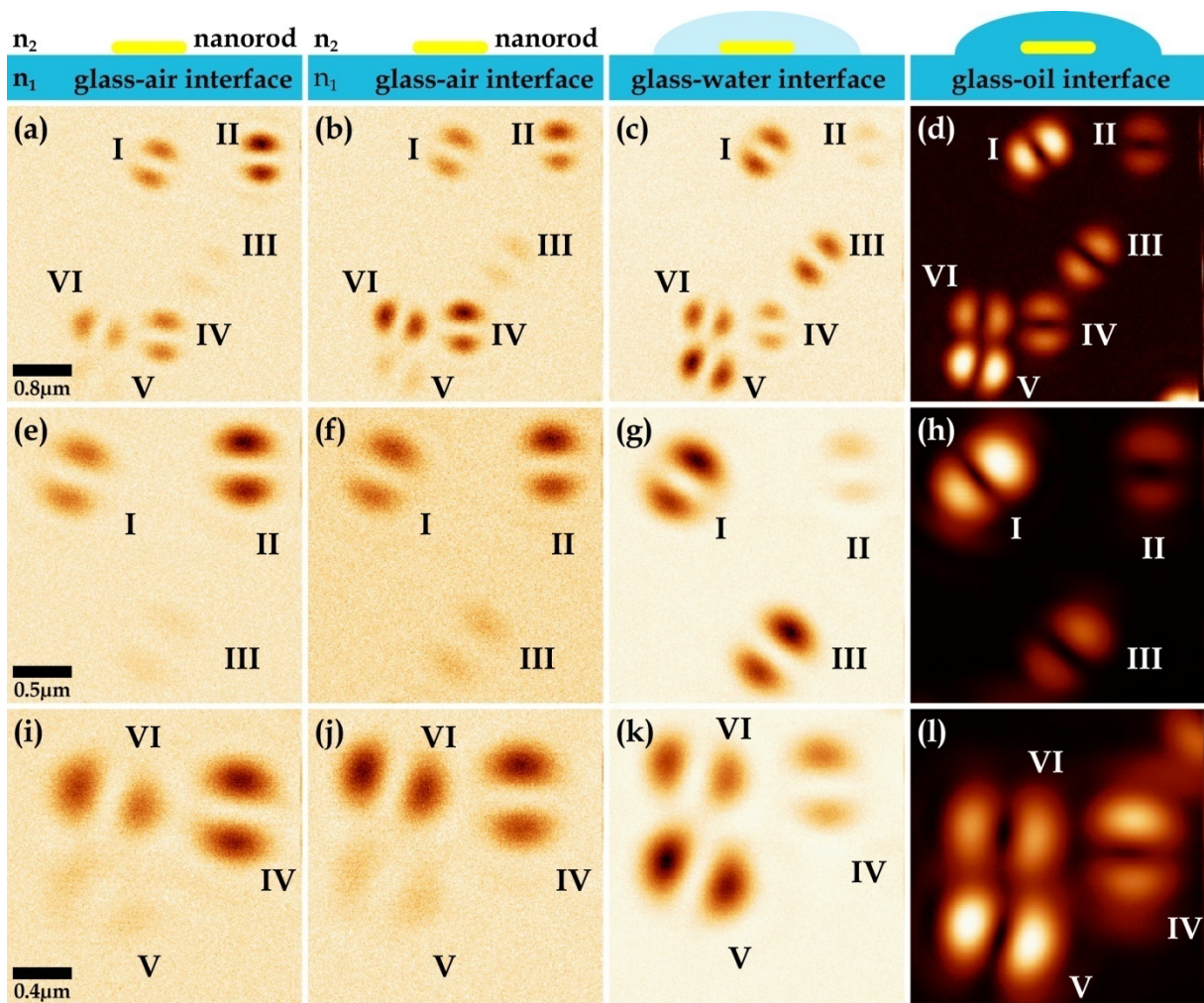
Figure 44: Scattering images of the same set of spatially isolated gold nanorods (APDM at 633 nm) at different interfaces as indicated schematically at the top (first/second column: glass-air/after evaporation of the water, third column: glass-water, last column: glass-oil). Besides differences in the overall image quality or contrast, the intensity of the individual particles varies for the different cases, that is, their visibility is not always the same neither is their relative intensity.

5.1 Particles at Dielectric Interfaces with Different Refractive Properties

Taking a closer look at Figure 44 one can recognized that the relative intensity of the particles changes depending on the sample interface. For the different interfaces, the particles' intensities increase in the following order:

glass-air interface (Figure 44, 1st column): V, III, I,   VI, II, IV

dried glass-air interface (Figure 44, 2nd column): III, V, I,   II, IV, VI

glass-water interface (Figure 44, 3rd column): II, IV, VI, I,   III, V

glass-oil interface (Figure 44, 4th column): II, IV, VI, III, V, I.

The relative intensity of the particles is strikingly similar for the glass-water and the glass-oil interface. For index matching conditions, solely the scattered intensity is detected. Therefore, the intensity order mainly resembles the overlap of the excitation wavelength and the SP resonances, that is their aspect ratio. At the glass-water interface, SP resonances are slightly shifted and the particles' direct environment comes into play, influencing the interference term. For the glass-air interfaces, obviously, the scattering term is overwhelmed by interference, *i.e.* the direct environment plays a key role. A strong dependence of the phase relation φ causes considerable intensity changes, which is also supported by the intensity variations after evaporation of the water.

5.1.2.2   Coming Back to Particles Sensing the Interface via SNRs

A more detailed analysis of the individual particles shown in Figure 44 is given in Figure 45. Close-ups of the particles at the different interfaces are provided. The contrast of the images at the glass-oil interface was inverted to allow for a better comparison. Each row shows the images of one particle, starting with particle I (for particles III and V, images at the initial glass-air interface were not acquired). In general, the overall scattering pattern does not change depending on the sample interface, regarding the pattern shape and relative contrast. As a consequence, one cannot necessarily tell at which sample interface an image has been taken without further information like *e.g.* numerical intensity values. However, this continuance in the shape of the pattern allows to directly transfer the results to determine the 2D orientation of gold nanorods at the glass-air interface to both a glass-water and a glass-oil interface. The same holds true for the determination of differently shaped nanoparticles. In addition, it can be safely assumed that these results can also be applied to other sample interfaces. However, taking a closer look at Figure 45, the orientation of some particles changes upon the addition of a liquid on top of the sample. For example, particle I changes its orientation three times, upon addition of the water (see Figure 45 a, c), after evaporation of the water (see Figure 45 c, b), and again upon addition of the immersion oil (see Figure 45 b, d). Particles II and IV also slightly change their orientation (see Figure 45, 2nd and 4th row). Such variations in the particle orientation are to be expected, since the gold nanorods were spin coated on the glass surface without any further attachment. Therefore, it makes sense that they might occasionally overcome the weak electrostatic forces which bind them to the glass substrate.

5.1 Particles at Dielectric Interfaces with Different Refractive Properties
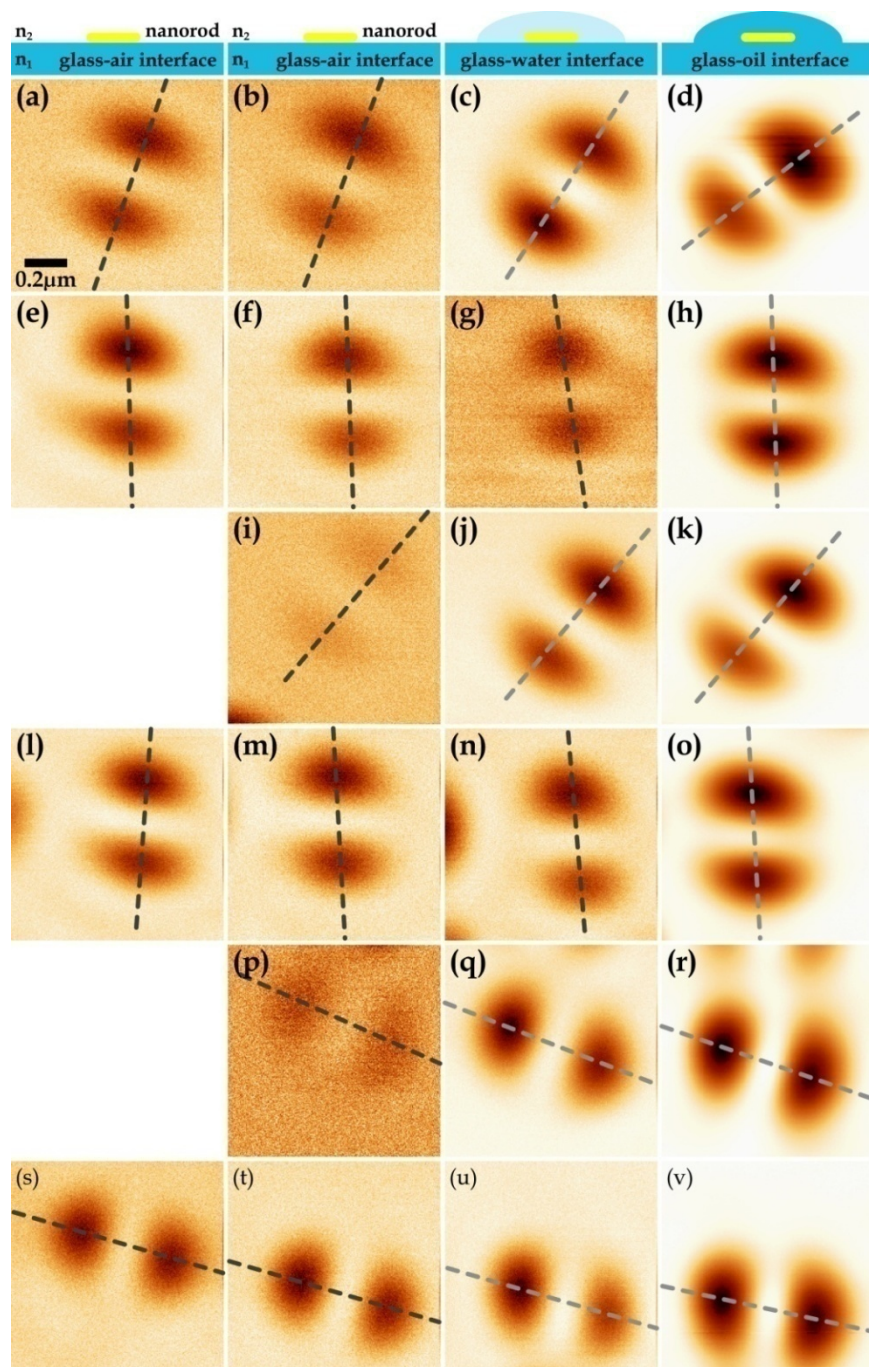
Figure 45: Scattering images (APDM at 633 nm) of the gold nanorods imaged in Figure 44 at different interfaces as indicated schematically at the top (first/second column: glass-air/after evaporation of the water, third column: glass-water, last column: glass-oil). The contrast of the images at the glass-oil interface was inverted for better comparison with the other interfaces. The shape of the patterns is not influenced by the optical properties of the sample interface. From images of individual particles, it is not even possible to tell at what kind of interface the image has been taken without knowing the numerical intensity values. However, for most particles, the image contrast increases with decreasing refractive index mismatch as can be recognized from the profiles taken along the dashed lines which are plotted in Figure 46.

To compare the intensity values, profiles were taken along the grey dashed lines for each image. The profiles are plotted in Figure 46. For better comparison, the values were background corrected, that is, the background values were set to zero. As can be already recognized from the confocal images, there is a considerable variation in the contrast for the particles at each interface. This variation is most pronounced at the glass-oil interface. For the glass-water and the glass-air interface, the values overlap partly. However, it is the most intense particles for the glass-air interface which overlap with the weakest ones at the glass-water interface.
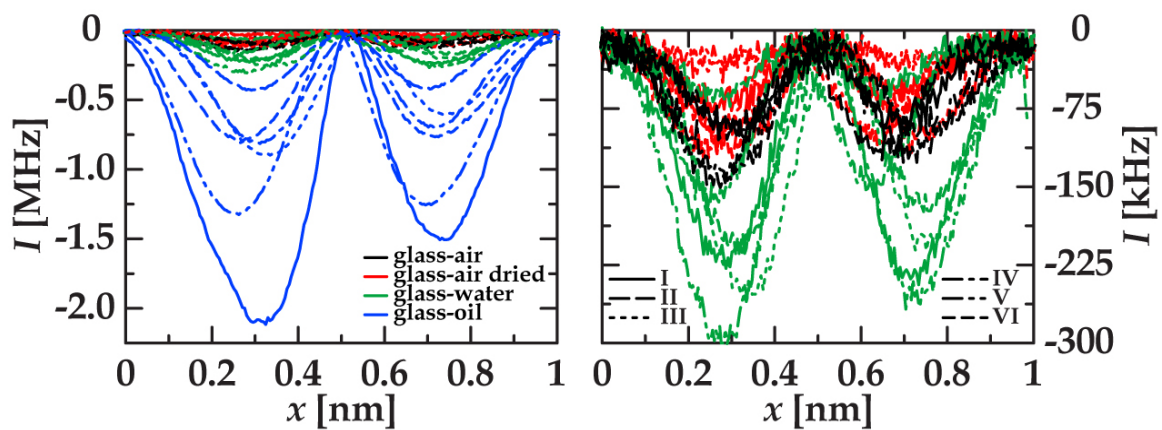
Figure 46:   Profiles taken along the dashed lines in the scattering images depicted in Figure 45. In all cases, the image contrast is strongest at index matching conditions and usually increases with decreasing refractive index mismatch. Despite some regions of overlapping, the optical properties at the interface lead to different intensity values, allowing to roughly determine the sample interface. In addition, the SNR varies for the three interfaces (see Table 8).

Although it is hence possible to roughly determine the sample interface by the numerical intensity values, another interesting parameter is the SNR. As can be recognized from the profiles in Figure 46, the SNR increases with decreasing refractive index mismatch. Such a dependence is already to be expected from the increasing image quality, for which the SNR can be regarded as a measure. For a more quantitative analysis, the SNR was determined for each interface, taking the intensity values measured along the profiles shown above and comparing them to the standard deviation of a signal-free region (*i.e.* the BG noise). Despite considerable variations in the values resulting for each particle due to contrast differences, the analysis resulted in a clear classification of the three interfaces by their SNR data. A

special case is the glass-oil interface, where in general the signals are so strong that the background is hardly signal-free in the acquired image area. However, the noise does not considerable change when slightly affected by the signal. The numerical results are summarized in Table 8.

Table 8: SNR for the six particles imaged in Figure 44, Figure 45. The intensity values were determined from the profiles shown in Figure 46. The noise was measured as the standard deviation from a signal-free region (*i.e.* the BG noise). Despite considerable variations in the data for individual particles, the three interfaces result in characteristic SNR values, which should allow for a classification of the interface when an ensemble of particles is analysed.

particle (cf. Figure 44, Figure 45)	SNR			
	glass-air	glass-air dried	glass-water	glass-oil
I	18	17	39	358
II	28	18	13	109
III	30	20	22	267
IV	20	21	37	260
V	7	15	37	243
VI	15	12	45	109
mean value	**20 ± 8**	**17 ± 3**	**32 ± 11**	**223 ± 89**

The analysis resulted for the glass-air interfaces in a mean SNR $\approx$ 20, for the glass-water interface of a SNR $\approx$ 30 and for the glass-oil interface of a SNR $\approx$ 200. As a consequence of the small number of analyzed particles, the standard deviations are considerable. Nevertheless, analyzing only the SNR values, in most cases, the correct sample interface would have been identified even on the basis of a single particle. This emphasizes that an analysis with more particles could easily identify a number of different interfaces. Since the identification does not have to rely on a single particle but can comprise a large number of particles, the analysis could be further refined. In general, the method would greatly benefit from highly size homogeneous samples since this minimizes intensity differences especially in liquid environments, where the influence of the SP resonance is crucial.

5.1.2.3 Direction of Refractive Index Transition and Contrast Inversion

As has been shown above, the sign of the image contrast changes approaching index matching conditions. This phenomenon also allows to distinguish the direction of refractive index transition, *i.e.* the transition from high *n* to low *n* vs. the transition from low *n* to high *n*. Such conditions were realized by sealing an aqueous solution of gold nanorods between two glass cover slips. As a consequence, a lower (glass-water) and an upper (water-glass) interface, with respect to the microscope objective focusing from below, are found. The resulting experimental scattering images are shown in Figure 47, together with a sketch of the sample layout.
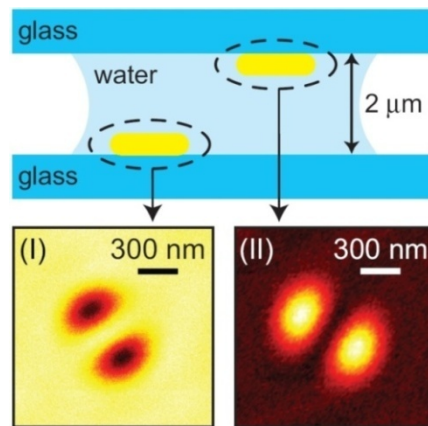
Figure 47: Schematic of a sample with individual, spatially isolated gold nanorods attached to a lower (glass-water) and an upper (water-glass) interface with respect to the optical setup. (I)/(II) The corresponding experimental scattering patterns measured for single nanorods (APDM at $\lambda = 633$ nm) at the lower/upper interface show negative/positive contrast. The intensity scale provided by the underlying colour map is optimized for each image separately. Figure taken from reference [40].

At both interfaces, spatially isolated gold nanorods could be detected. In each case, two-lobed patterns were observed. At the lower interface (high *n* to low *n*), the experimental image contrast was found to be negative in all cases. At the upper interface (low *n* to high *n*), however, the image contrast was always positive. This is attributed to the phase difference of π for the reflection coefficients of the two interfaces, switching the overall phase of $\mathbf{E}_{ref}$.[40] Measuring such variations in the image contrast could allow to precisely locate a scattering particle within a dielectric interface. Alternatively, local variations in the refractive properties of an interface, like *e.g.* a cell membrane, should be detectable.

6   Gold Nanorods in Cells

It has been reported that gold nanorods are taken up by cells without being cell-toxic.[42-44] Because of their favourable optical properties, they are interesting as optical labels in general and especially for biological samples. Since it has been shown that they are not cell-toxic and on the contrary are often tolerated as an additive in cell culture,[42, 43] we tested if the gold nanorods can be detected in cells. Therefore, diluted particle solutions were added to a cell culture of human cells (MR70).[12] The cells were fixed with formaldehyde and covered with vectashield® for the confocal experiments. The samples were stained with 4′,6-Diamidino-2-phenylindole (DAPI), which primarily binds to DNA and stains the cell nucleus. The absorption of DAPI occurs in the blue spectral region, consequently, a second, blue laser (at 390 nm) was coupled into the confocal microscope. The DAPI emission peaks around 470 nm and was detected with a 390 nm notch filter in the detection path. In most cases, however, the elastically scattered light at 633 nm was detected and an APDM was used for excitation.

The cells as well as their nuclei can be clearly identified by the red scattered light as shown in Figure 48: The elastically scattered light upon excitation with an APDM at 633 nm was detected (see Figure 48 a) for a sample of cells which were exposed to a solution of gold nanorods. For comparison, the same sample area is shown upon excitation with a linearly polarized Gaussian mode (LPGM) at 390 nm and detection of the fluorescent emission of the DAPI staining, clearly showing the cell nuclei while the signal of the remaining tissue is negligible (see Figure 48 e-g).

---

[12] The cells were cultured and samples kindly provided by the Group of Masashi Narita at The Cancer Research UK Cambridge Institute, University of Cambridge, Great Britain.
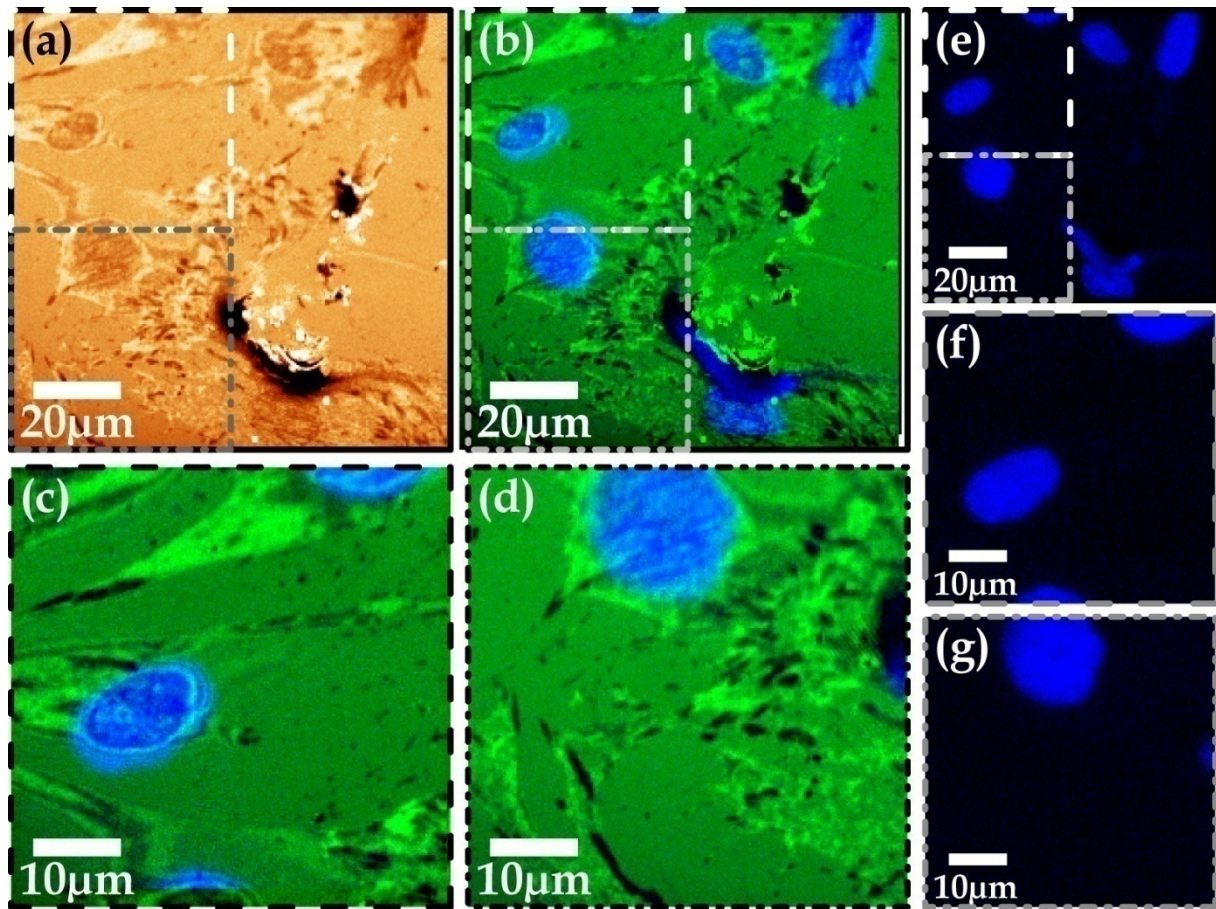
Figure 48: Confocal images of fixed human cells (MR70) which were exposed to gold nanorods and stained with DAPI. (a) Elastically scattered light (APDM at 633 nm), image size $100 \cdot 100$ μm². (b) Same sample area, overlay of the scattering data (green) and the fluorescent data (blue, LPGM at390 nm): (c, d) Sample area as given by the white/grey dashed lines, overlay of the scattering data (green) and the fluorescent data (blue). (e-g) Fluorescent DAPI emission upon excitation at 390 nm. The fluorescent DAPI emission results from the cell nuclei since the fluorescent dye primarily binds to the nuclear DNA.

Several cells are imaged in the overview given in Figure 48 a, when the scattered light is detected. In addition, the scattering data (green) and the fluorescent image (blue) are presented as an overlay in Figure 48 b. The areas given by the white and grey dashed lines in the overviews are provided as overlay images in Figure 48 c, d. From the overlays it is obvious that the cell nuclei can be easily recognized in the scattering data as well. To detect the red shifted light upon excitation with an APDM at 633 nm, a notch filter was implemented in the detection path. This resulted in images similar to the detection of the DAPI fluorescent emission upon excitation at

5.1 Particles at Dielectric Interfaces with Different Refractive Properties

390 nm, that is, primarily light emission from the cell nuclei was detected (cf. Figure 53, Figure 54).

In Figure 49, images from the control sample are presented, taken from cells which were not exposed to a gold particle solution.
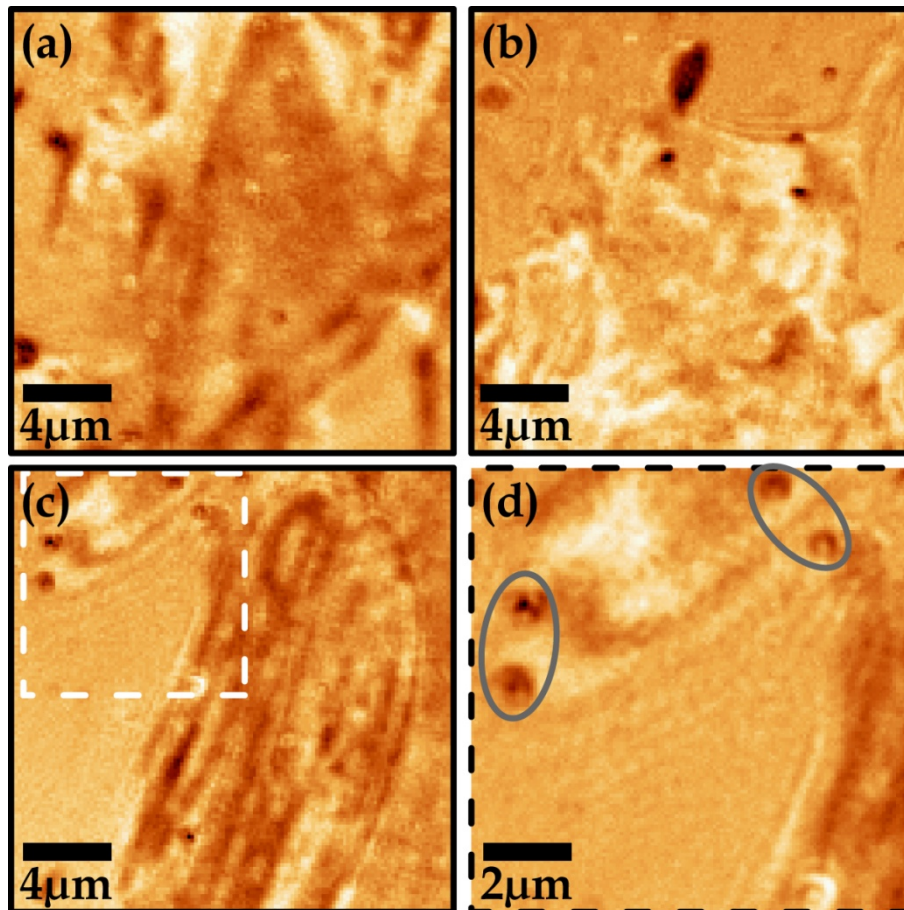
Figure 49: Confocal scattering images (APDM at 633 nm) of fixed human cells (MR70). (a-c) Different areas of the sample ($20 \cdot 20 \, \mu m^2$), (d) close-up ($10 \cdot 10 \, \mu m^2$) of the area given by the white dashed line in (c). The cells which were not exposed to a gold particle solution and serve as a negative control sample can be clearly identified by the elastically scattered light. The encircled features slightly remind of scattering patterns as caused by gold nanorods, therefore, such patterns have to be treated carefully.

The cells are clearly visible by the elastically scattered light upon illumination with an APDM at 633 nm (see Figure 49). They are spread out flat on the glass surface as can be recognized from the different overview areas in Figure 49 a-c ($20 \cdot 20 \, \mu m^2$ each). A smaller area is presented in Figure 49 d, providing a close-up of the area given by the white dashed line in Figure 49 c. Two ring-shaped or almost two-lobed

patterns can be recognized in the upper right corner of Figure 49 d (encircled), as well as spot-like patterns on the left (encircled), reminding of the scattering patterns of gold particles. However, the ring-shaped patterns are asymmetric, that is, the ring is opened at one point rather than forming a real two-lobed pattern or a closed ring. Additionally, while spot-like patterns can be easily explained upon excitation with a RPDM for particles with an orientation parallel to the optical axis, that is not the case upon excitation with azimuthally polarized light as used here. Therefore, it is not likely that these patterns are caused by gold nanoparticles but are due to scattering structures of the cells or the embedding medium. Either way, since these cells were not exposed to a gold particle solution, nanorods should not be present in the sample. However, it was to be clarified if similar patterns are found in a negative control. As can be recognized from Figure 49 c, d, one has to be careful in the image analysis since similar patterns might occur.

For samples containing cells which were exposed to a gold nanorod solution, one still has to clarify if and where there are particles to be found in the sample. An example for gold particles on the glass surface, that is outside of the cells but sometimes in their close proximity, is given in Figure 50.

5.1 Particles at Dielectric Interfaces with Different Refractive Properties
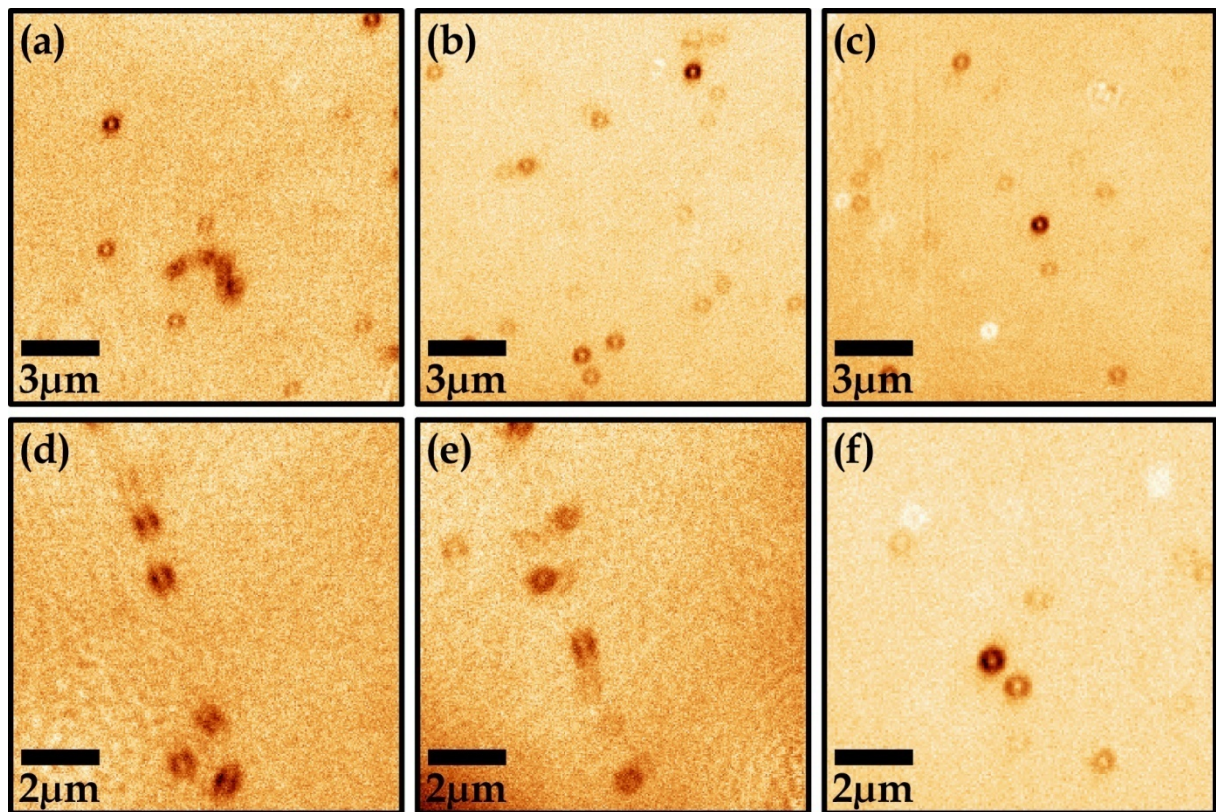
Figure 50: Confocal scattering images (APDM at 633 nm) of gold nanorods at the glass surface of a sample containing human cells (MR70) which were exposed to a gold particle solution. Besides the two-lobed patterns for individual gold nanorods, also aggregated particles are visible. Some appear to form chains, resulting in patterns of two short parallel lines. Additionally, ring-shaped patterns are observed, as well as patterns with a positive image contrast, suggesting a 3D particle orientation in the sample.

A number of individual gold particles is found on the glass surface. Besides a two-lobed pattern shape, particle aggregates are also observed, resulting in larger patterns (see *e.g.* Figure 50 a). Some of these patterns consist of two short parallel lines (see Figure 50 d, e), suggesting a chain of nanorods with similar orientation of the long particle axis running in parallel to these lines (equivalent to an end-to-end orientation of the particles). In addition, ring-shaped patterns are observed as well as patterns with a positive image contrast (see Figure 50 c, f), indicating a 3D orientation of the particles in the sample.

Images of a sample with cells which were exposed to gold nanorods are presented in Figure 51. Again, the elastically scattered light at 633 nm upon illumination with an APDM was detected.

5.1 Particles at Dielectric Interfaces with Different Refractive Properties

Figure 51: Confocal scattering images (APDM at 633 nm) of fixed human cells (MR70) which were exposed to gold nanorods. (a, c) Different areas of the sample ($30 \cdot 30\ \mu m^2$ and $20 \cdot 20\ \mu m^2$), (b, d) close-ups ($5 \cdot 5\ \mu m^2$) of the areas given by the dashed lines. The gold particles appear to be found both on the glass surface near the cells and co-located with the cells (see b, d).

As can be recognized from the overview images in Figure 51 a, c, the cells can easily be recognized by the scattered light. In Figure 51 a, an area of $30 \cdot 30\ \mu m^2$ is presented, imaging one cell lying flat on the glass surface. A close-up of the area given by the white dashed line ($5 \cdot 5\ \mu m^2$) is provided in Figure 51 b. Figure 51 c shows another sample area of $20 \cdot 20\ \mu m^2$, with the close-up of the area outlined by the grey dashed line ($5 \cdot 5\ \mu m^2$) in Figure 51 d. In the vicinity of the cells, a number of particles are visible. They appear to be on the glass surface (see Figure 51 a, c). In addition, individual particles are found co-located with the cells, as shown in Figure 51 b, d.

Other examples of particles co-located with cells are shown in Figure 52. In addition to the elastically scattered light (see Figure 52 a, c, d), the red shifted

5.1 Particles at Dielectric Interfaces with Different Refractive Properties

emission was also detected (see Figure 52 e). This emission is not clearly defined as it would be in the cell nucleus, however, it is not negligible.

Figure 52: Confocal images (APDM at 633 nm) of fixed human cells (MR70) which were exposed to gold nanorods. Overview of an area inside a cell ($20 \cdot 20\ \mu m^2$): (a) scattering data, (b) overlay of the scattering data (green) and the red shifted emission (red), (c) close-up ($10 \cdot 10\ \mu m^2$) of the area given by the white dashed line, (d) close-up ($2 \cdot 2\ \mu m^2$) of the area given by the grey dashed line, (e) overview, red shifted emission ($20 \cdot 20\ \mu m^2$).

The overview image in Figure 52 a ($20 \cdot 20\ \mu m^2$) shows that particles are co-located with the cells and are probably present in the cytosol. The overlay of the elastically scattered data (green) and the red shifted emission (red) in Figure 52 b ($20 \cdot 20\ \mu m^2$) does not reveal special features, as can be also recognized from the red shifted emission itself in Figure 52 e ($20 \cdot 20\ \mu m^2$). The close-ups as given by the dashed lines in the overview images are presented in Figure 52 c, d ($10 \cdot 10\ \mu m^2$ and $2 \cdot 2\ \mu m^2$, respectively). They clearly reveal the presence of individual particles inside the cell. However, the cell nucleus is not concerned in this case. For comparison, an example showing the nucleus is presented in Figure 53.

The cell nucleus is easily visible both in the elastically scattered data in Figure 53 a and in the red shifted emission in Figure 53 e ($20 \cdot 20\ \mu m^2$).
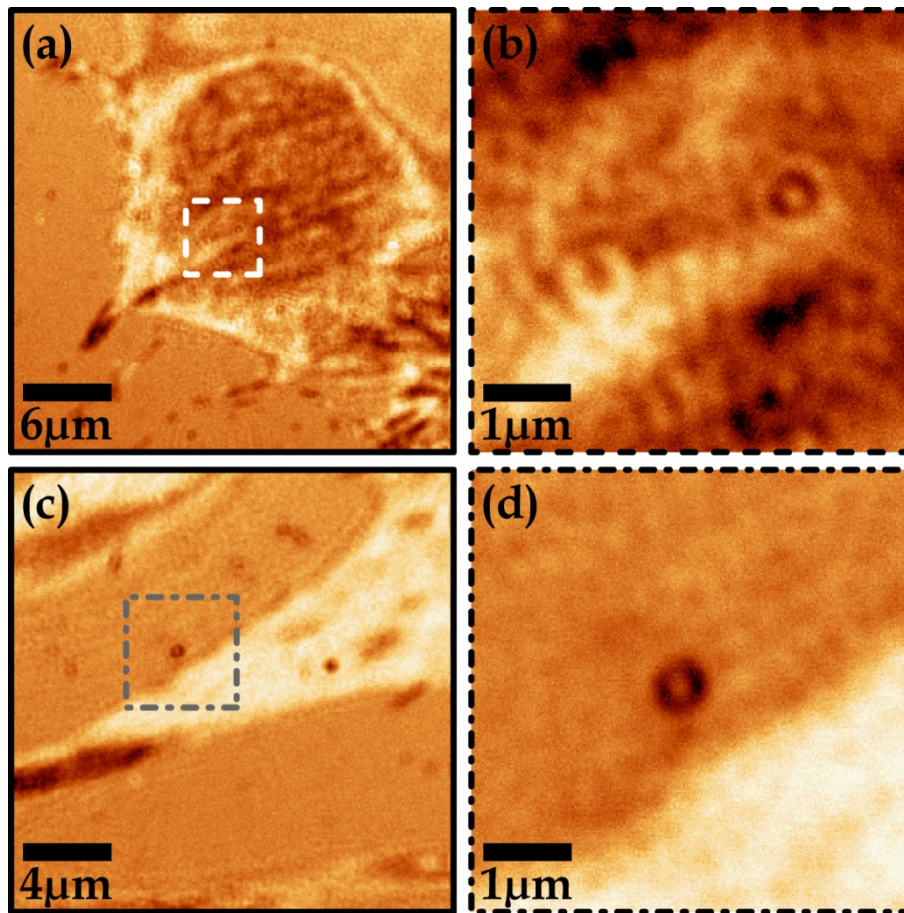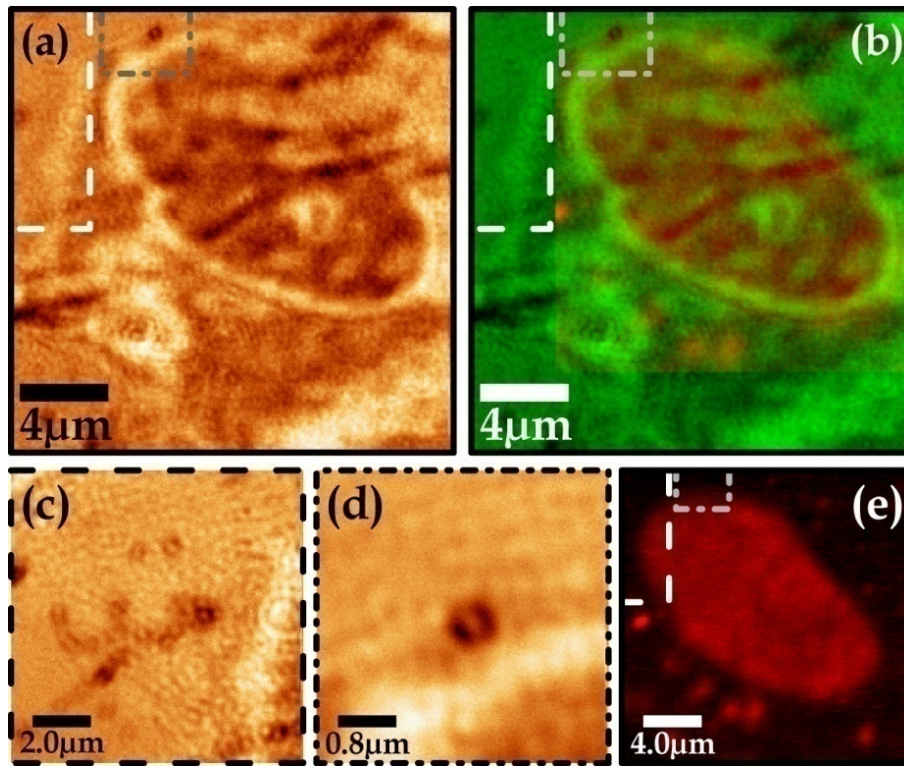

Figure 53: Confocal images (APDM at 633 nm) of fixed human cells (MR70) which were exposed to gold nanorods. Overview of an area showing the cell nucleus ($20 \cdot 20\ \mu m^2$): (a) scattering data, (b) overlay of the scattering data (green) and the red shifted emission (red), (c) close-up ($10 \cdot 10\ \mu m^2$) of the area given by the white dashed line, (d) close-up ($4 \cdot 4\ \mu m^2$) of the area given by the grey dashed line, (e) overview, red shifted emission ($20 \cdot 20\ \mu m^2$). Gold particles are found in the vicinity of the cell and might as well be taken up by the cell itself.

Additionally, an overlay of the scattered light (green) and the red shifted emission (red) is provided in Figure 53 b. The areas as indicated by the dashed lines in the overview data are provided as close-ups in Figure 53 c, d ($10 \cdot 10\ \mu m^2$ and $4 \cdot 4\ \mu m^2$, respectively), showing several gold particles close to or inside the cell. Especially the particles in Figure 53 c appear to be close to the cell membrane. Thus, the image might show the process of particle uptake.

Another example of gold particles being co-localized with the cell nucleus is given in Figure 54. Again, the elastically scattered light was detected in the overview image in Figure 54 a ($20 \cdot 20\ \mu m^2$).

5.1 Particles at Dielectric Interfaces with Different Refractive Properties

The red shifted emission is shown in Figure 54 e while Figure 54 b gives the overlay (20 · 20 µm²) of the scattered data (green) and the red shifted emission (red).
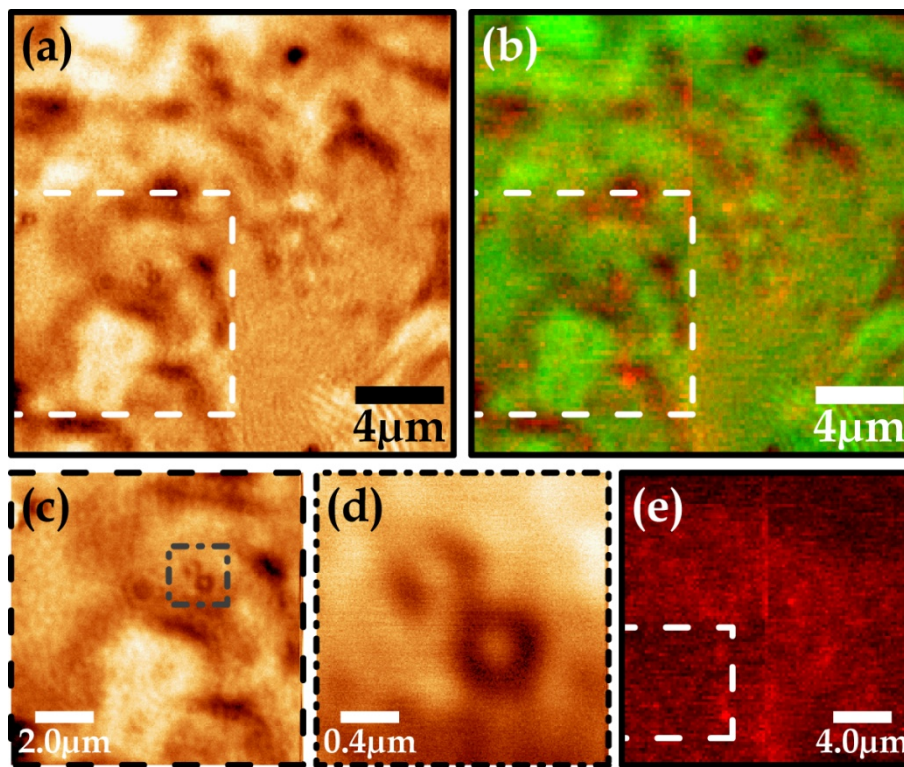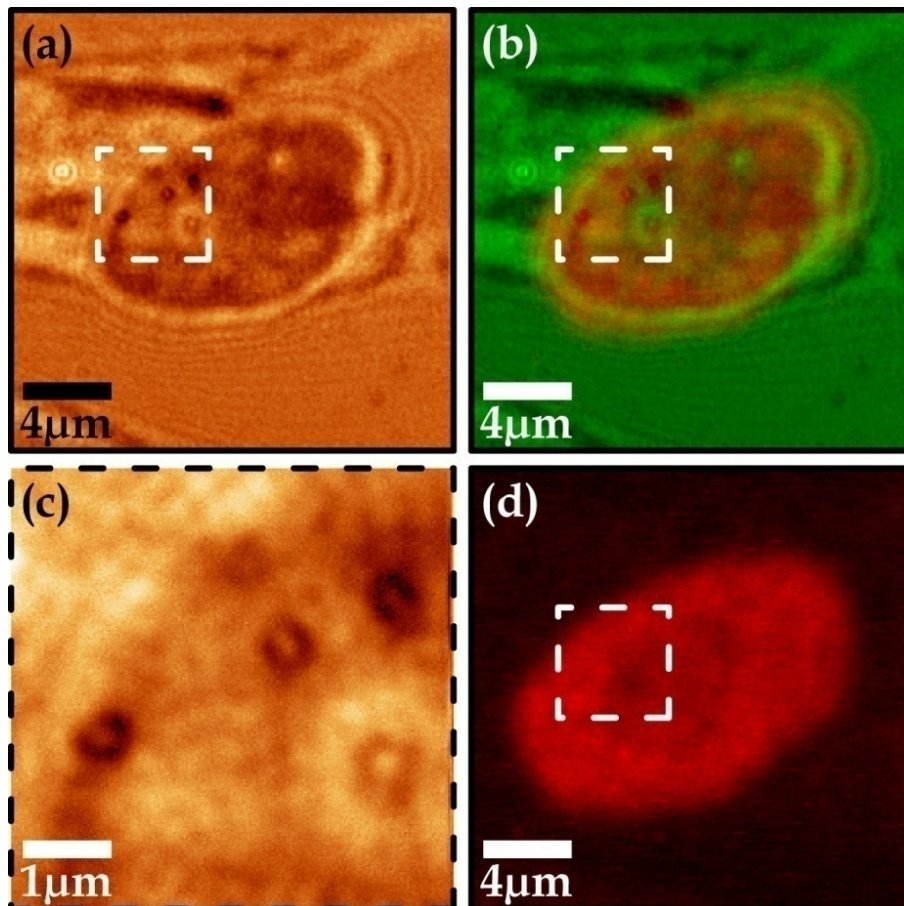

Figure 54: Confocal images (APDM at 633 nm) of fixed human cells (MR70) which were exposed to gold nanorods. Overview of an area showing the cell nucleus (20 · 20 µm²): (a) scattering data, (b) overlay of the scattering data (green) and the red shifted emission (red), (c) close-up (5 · 5 µm²) of the area given by the white dashed line, (d) overview, red shifted emission (20 · 20 µm²). Gold particles are found co-located with the cell nucleus.

Figure 54 c provides a close-up (5 · 5 µm²) of the area outlined by the dashed white line in the overview images. Individual particles are clearly visible in the cell nucleus.

In general, it has been shown that gold particles were incorporated in the cells. They were found both co-located with the cell nucleus and in the cytosol. In addition, the particles were also found outside of the cells but in their close proximity which might indicate the process of particle uptake through the cell membrane. Additionally, particles were also present on the glass surface (see Figure 50).

7 Tip-enhanced Scanning Optical Near-Field Microscopy on Single Gold Nanorods

The optical properties of individual gold nanorods were also investigated with a scanning near-field optical microscope (SNOM). The setup is based on the confocal microscope and described in chapter 3.4.4 (p. 47). A sharp gold tip was scanned over the sample to acquire the topography simultaneously with the photoluminescence (PL) data under excitation with light at 633 nm. Mainly, a RPDM was used for excitation since tight focussing of this mode generates a longitudinally polarized field component exciting electron oscillation along the tip-axis through SP resonances. For comparison, similar data was also acquired using an APDM at 633 nm for excitation, which has a purely transversally polarized field distribution in focus.

The acquired topography data was used to estimate tip and particle sizes in a similar way as for AFM measurements (cf. chapter 0, p. 72). The particle height was assumed as a measure for the particle's short axis to appraise the tip size. Profiles taken along the short and long particle axes in the sample plane were corrected accordingly. The particle orientation as determined from the optical data was used to eliminate any tip influences on an apparent orientation. Measured particle heights of approx. 30 nm are larger than the values determined by AFM measurements (h = 22.6±2.4 nm, see p. 72) and as given in the literature.[93-95, 152, 156] However, the z-axis of the near-field setup is not as accurate as the x- and y-axes because only the latter are closed loop controlled. Therefore, the resulting values have to be treated carefully. In addition, the absolute tip-sample distance is not known but can be assumed to be in the order of a few nanometres. Only distance changes can be sensitively measured. Therefore, the SNOM heights are regarded as an upper limit for the particle width. Hence, a rough estimate of the particles' sizes and aspect ratios R can be extracted. This approach will result in an underestimation of the tip size and R, as well as an overestimation of the particle axes. Alternatively, the particle

5.1 Particles at Dielectric Interfaces with Different Refractive Properties

height was assumed as measured by AFM, resulting in more reasonable values for *a*, *b* and *R* (compared to UV/Vis spectra and literature values,[93-95, 152, 156] see Table 9).

In general, the size and shape variation of the gold tips is larger as compared to commercially available AFM probes (cf. chapter 3.4.4, p. 49). A tip radius at the apex in the order of 10-20 nm can be expected, as supported by SEM (see chapter 3.4.4, p. 49) and estimations from the topography data. During measurements, the tip shape and size might change due to particle pick up or the softness of the material. Since the physical tip shape and size is not necessarily the same as the optically active part of the probe, the effects on topography and optical data do not have to coincide. Consequently, the topography data has to be treated carefully in terms of particle size and shape determination, taking into account the actual tip geometry, which might also be highly asymmetric. The shape and visibility of small glass pores on the sample surface are a good first indicator for tip sharpness.

Regarding estimated tip sizes, in most cases, radii in the order of 10-20 nm fairly correspond with the expectations from SEM images (cf. chapter 3.4.4, p. 49). Additionally, much higher values are found, indicating tip deterioration upon measuring, which is also reflected in the corresponding topography images (*e.g.* glass pores not visible). In the last line of Table 9, mean values and standard deviations for measurements with an estimated tip size < 40 nm are given.

Table 9:   Particle sizes as determined from SNOM measurements. The values for *a* and *b* are the FWHM from profiles of the topography. The particle height *h* served as a measure for *b*, due to the associated uncertainties for absolute heights in SNOM, the mean height from AFM measurements was taken alternatively. These values show a nice agreement with the mean *R* = 2.5 from UV/Vis spectra and sizes expected from literature.[93-95, 152, 156] Mean values and standard deviations for tip sizes < 40 nm are given in the last line.

values as measured by SNOM		corrected values considering the height measured by SNOM				corrected values considering the height measured by AFM			
long axis *a* [nm]	short axis *b* [nm]	height h_{SNOM} [nm]	tip size SNOM [nm]	long axis $a_{corr,SNOM}$ [nm]	aspect ratio R_{SNOM} [ ]	height h_{AFM} [nm]	tip size SNOM [nm]	long axis $a_{corr,AFM}$ [nm]	aspect ratio R_{AFM} [ ]
83	47	29	18	65	2.2	22.6	24.4	58.6	2.6
77	44	28	16	61	2.2	22.6	21.4	55.6	2.5
107	69	27	42	65	2.4	22.6	46.4	60.6	2.7
80	80	30	50	30	1.0	22.6	57.4	22.6	1.0
70	59	29	30	40	1.4	22.6	36.4	33.6	1.5
80	50	28	22	58	2.1	22.6	27.4	52.6	2.3
75	44	27	17	58	2.1	22.6	21.4	53.6	2.4
75	50	28	22	53	1.9	22.6	27.4	47.6	2.1
72	43	27	16	56	2.1	22.6	20.4	51.6	2.3
84	41	28	13	71	2.5	22.6	18.4	65.6	2.9
74	48	29	19	55	1.9	22.6	25.4	48.6	2.2
103	57	29	28	75	2.6	22.6	34.4	68.6	3.0
78	51	30	21	57	1.9	22.6	28.4	49.6	2.2
78	39	30	11	67	2.4	22.6	16.4	61.6	2.7
79±8.2	**48±5.8**	**29±0.8**	**19±5.4**	**60±8.8**	**2.1±0.3**	**-**	**25±5.8**	**54±8.9**	**2.4±0.4**

Since the gold nanoparticles were spin coated on the glass substrate and not especially fixed, it is easily possible to move the particles with the tip when the parameters are not carefully adjusted (see Figure 55).

5.1 Particles at Dielectric Interfaces with Different Refractive Properties
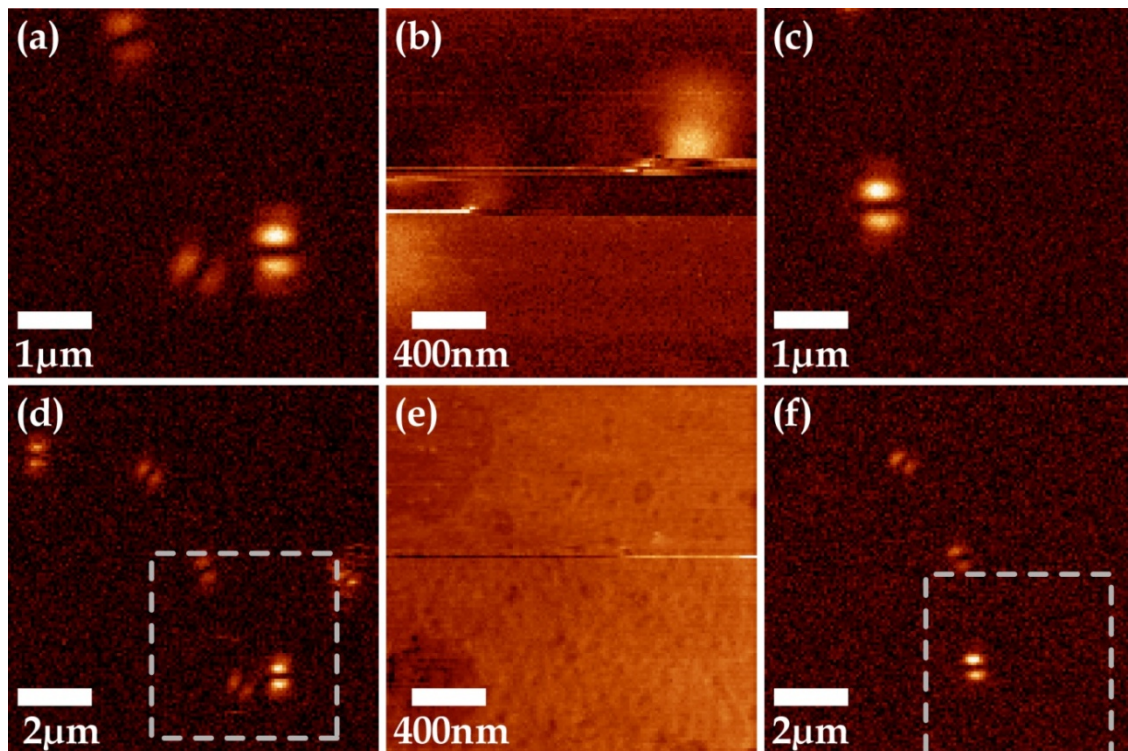
Figure 55: Series of three consecutive (a-c) confocal PL and (e) corresponding topography data. Two particles were moved by the scanning probe. (d, f) Overview of the same sample area imaged with confocal microscopy (the respective areas (a), (b) are indicated by the grey dashed squares). The movement of the two particles is visible in the PL image (b) as well as in the topography (horizontal line in (e)). The displacement of the brightest particle can be recognized comparing the larger scan areas depicted in (d) and (f): it is shifted to the left while its orientation remains unaffected. The second particle is missing after scanning the tip over the surface, therefore it might have been picked up by the tip. Particle moving can happen when the scanning parameters are not carefully adjusted, *e.g.* when the *QF* is too low as in this case (*QF* = 180).

In this case, the *QF* was too low (*QF* = 180). The figure shows a series of three consecutive confocal scans (Figure 55 a-c) with the corresponding topography image in Figure 55 e. Larger scans of the same area were acquired with confocal microscopy (see Figure 55 d, f) to provide a better overview. For convenience, the scan areas shown in (a) and (b) are indicated by the grey dashed squares. The images where acquired consecutively from left to right, that is, the images shown on the left (see Figure 55 a, d) were measured before the tip was moved over the sample, while those on the right (see Figure 55 c, f) were taken after the scanning. The movement of the two particles by the scanning probe is directly visualized in the central column (see Figure 55 b, e): in the PL data, the horizontal lines indicate the movement of both

particles. The scanning was undertaken from the top downwards, therefore, the far-field PL signal of the particles is still partly visible because it was detected before the tip came close enough to shift the particle itself. However, as soon as the tip touched the particle, it was moved. Consequently, the optical signal was lost. The movement of the first particle is also visible in the topography image as a horizontal line (see Figure 55 e). Surprisingly, the topography of the sample surface remains remarkably clear after the particles have been shifted, suggesting that they were probably not picked up by the tip-apex. However, as can be clearly recognized from Figure 55 c, d and f, one particle is missing after scanning the tip over the sample. It is not simply moved out of the scanning area as revealed by the larger confocal image (Figure 55 f). Therefore, it cannot be ruled out that the particle was collected by the probe. The second, brightest particle, which is still visible, was moved to the left and relatively to the other, surrounding particles while its orientation remained unchanged as shown in the larger image (cf. Figure 55 b, f).

When the topographic information is acquired in parallel with the optical image using radially or azimuthally polarized light, the orientation of individual gold nanorods can in principle be determined from both the topographic and the optical data. Usually, the orientation of the long particle axis can be recognized from the topography data and nicely corresponds with the orientational visualization in the two-lobed far-field patterns (see Figure 56). However, when considerable convolution of the scanning probe and the gold particle occurs, the topographic data does not necessarily give the actual physical orientation of the nanorods. Consequently, the orientation from the optical data was used to determine the FWHM in the topography.

Since the tip was not well aligned in the optical focus upon acquiring the images shown in Figure 56, an optical near-field enhancement is not observed. However, the topography (Figure 56 b) of the gold nanorod nicely shows its orientation in comparison with the optical far-field pattern upon excitation with a RPDM (Figure 56 a).

5.1 Particles at Dielectric Interfaces with Different Refractive Properties

Figure 56: PL (a) and topography (b) data of an individual gold nanorod (RPDM at 633 nm). Profiles (c, d) along the grey dashed lines (a = 83 nm, b = 47 nm, h = 29 nm). Optical and topographic data are considerably shifted due to misalignment of the scanning probe in focus. An enhanced PL signal was not observed but particle orientation coincides in (a, b). Small pores in the glass substrate (encircled in grey) confirm tip sharpness.

The profiles taken along the grey dashed lines are plotted in Figure 56 c, d. From these values, the particle size was estimated (cf. Table 9, p. 124). Small pores are visible in the glass surface as dark dots in the topography image (some of them encircled in grey) with a measured depth of 2-4 nm and a FWHM of 10-17 nm. The size of these pores should be considered as a rough estimate only because the probe might be too large to determine the depth of the pores accurately. Regardless, the data is supported by similar values obtained with AFM, confirming a reasonable tip sharpness here as well. Basically, it does not matter if the scattered or PL light is detected to determine the particle orientation. As shown above (see chapter 3.2.1, p. 35), the shapes of the resulting patterns are directly comparable. Changing between the RPDM and the APDM mainly involves a rotation of the patterns by 90 °.

7.1 Excitation with a RPDM

Upon focussing of a RPDM, the electric field distribution splits into two components: One having a transversal polarisation in the sample plane and a second one with a longitudinal polarisation along the optical axis (see chapter 2.1.2, p. 11). When a sharp gold probe is brought into the focus of a RPDM at 633 nm, the longitudinally polarized field component excites SPs along the tip-axis. As a consequence, the excitation field is enhanced with the tip-apex being the area with the highest overall intensity. This also results in an extreme spatial confinement of the excitation light, leading to a much smaller focal area which is mainly given by the size of the tip itself. When gold nanorods are excited with a RPDM at 633 nm and a sharp gold probe is scanned in close proximity over the sample, an enhanced PL is observed with the highest intensity found at the tips of the particles. This is to be expected, considering the curvature of the particle and the resulting field enhancement. The optical images in the following were BG corrected and are shown together with the respective topography data. A 3D representation of the topography with the PL intensity as colour code shows the localization of highest PL emission. An example is presented in Figure 57.
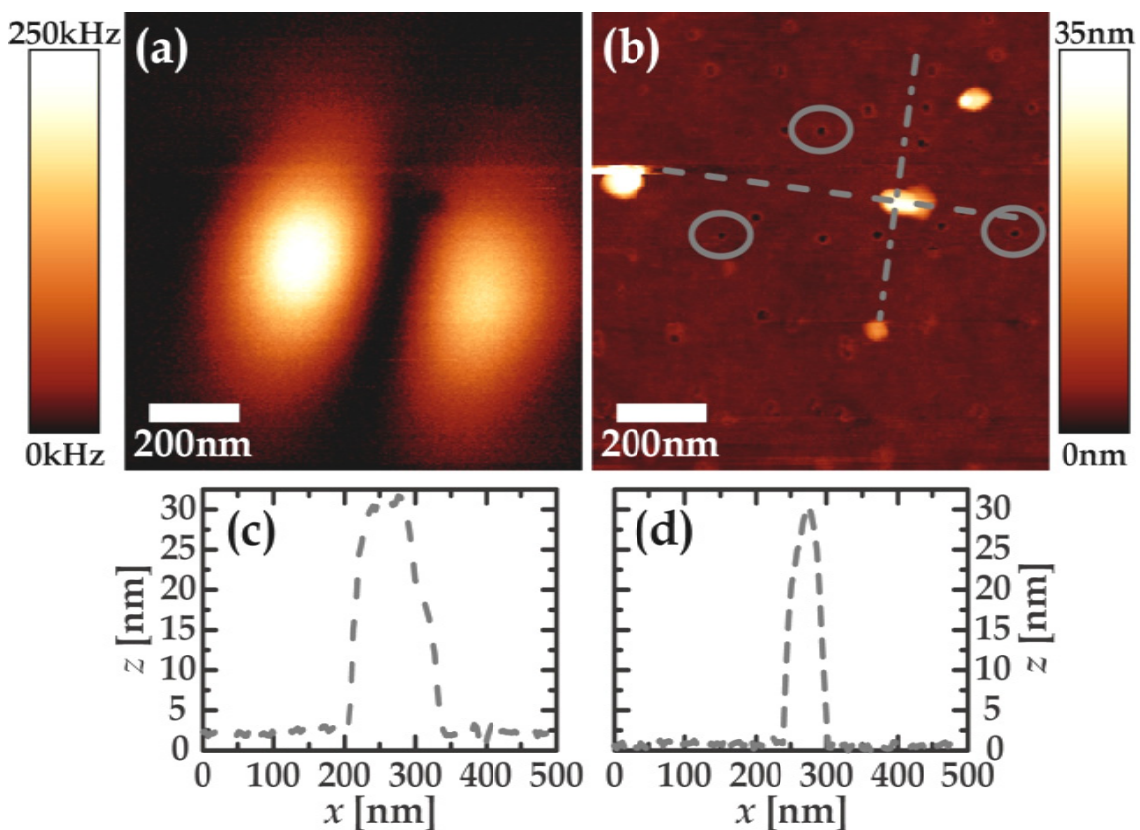
7.1 Excitation with a RPDM

Figure 57: PL (a) and topography (b) data of an individual gold nanorod (RPDM at 633 nm). Profiles (d, e) along the grey dashed lines (a = 77 nm, b = 44 nm, h = 28 nm). Optical and topographic data are shifted due to misalignment of the scanning probe in focus. Consequently, the enhanced PL signal is not in the centre of the far-field pattern. Small pores in the glass substrate (encircled in grey) confirm tip sharpness. 3D topography plot (c) with the optical data as colour code shows highest PL emission at the particle's tips. The image has been rotated as indicated by the black arrow at the top.

Figure 57 shows the PL (a) and topographic data (b) of an individual nanorod upon excitation with a RPDM at 633 nm in the proximity of a gold tip which was scanned over the sample. Consequently, the luminescence and the topographic data could be collected in parallel. The optical data in Figure 57 a consists of both the far-field and the near-field PL intensities. The far-field pattern corresponds to the one observed in the conventional confocal mode, that is, it is of the characteristic two-lobed shape reflecting the particle's orientation. The near-field pattern also has a somehow two-lobed shape, however, the two parts originate from the particle's tips as the areas of strongest PL emission. The topography data in Figure 57 b closely resembles the actual particle shape, as can be recognized from the FWHMs of the profiles taken along the grey dashed lines in Figure 57 d, e, which were used to estimate particle and tip size (cf. Table 9, p. 124). In addition, small pores are visible in the otherwise smooth glass substrate as small dark dots (see Figure 57 b, to guide the eye, some of them are encircled in grey). Again, the mapping of these pores implies that the tip is

reasonably sharp. The gold probe was not perfectly aligned in the focus centre resulting in an offset between the optical and topographic data. The PL intensity is obviously highest at the particle's tips, where the field enhancement should be strongest and the nanorod should consequently be glowing most intensely (see Figure 57 a, b). In Figure 57 c, a 3D topography plot is presented with the optical information as colour code. Please note that the 3D plot has been rotated for better visualization of the data (as indicated by the black arrow at the top). Overlaying the topographic and optical information illustrates the particle's tips as the areas of the most intense PL.

Similar examples are shown in Figure 58-Figure 60. In Figure 58, a sharp tip was used but not perfectly aligned in focus. An asymmetric near-field pattern is observed with higher PL emission at one particle end only (see Figure 58 a, c).
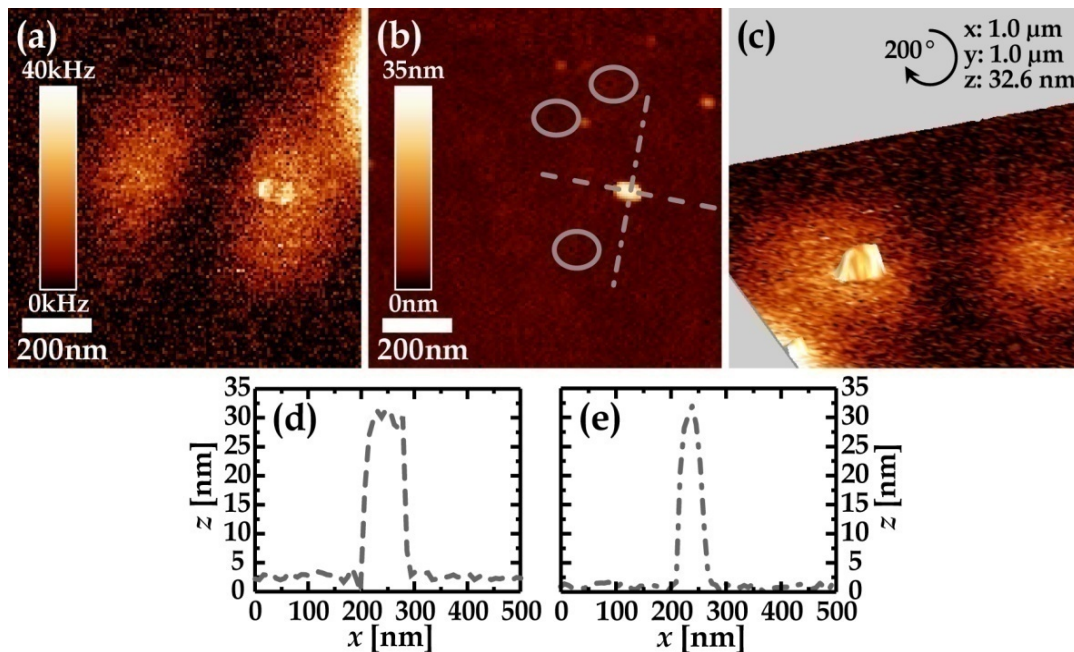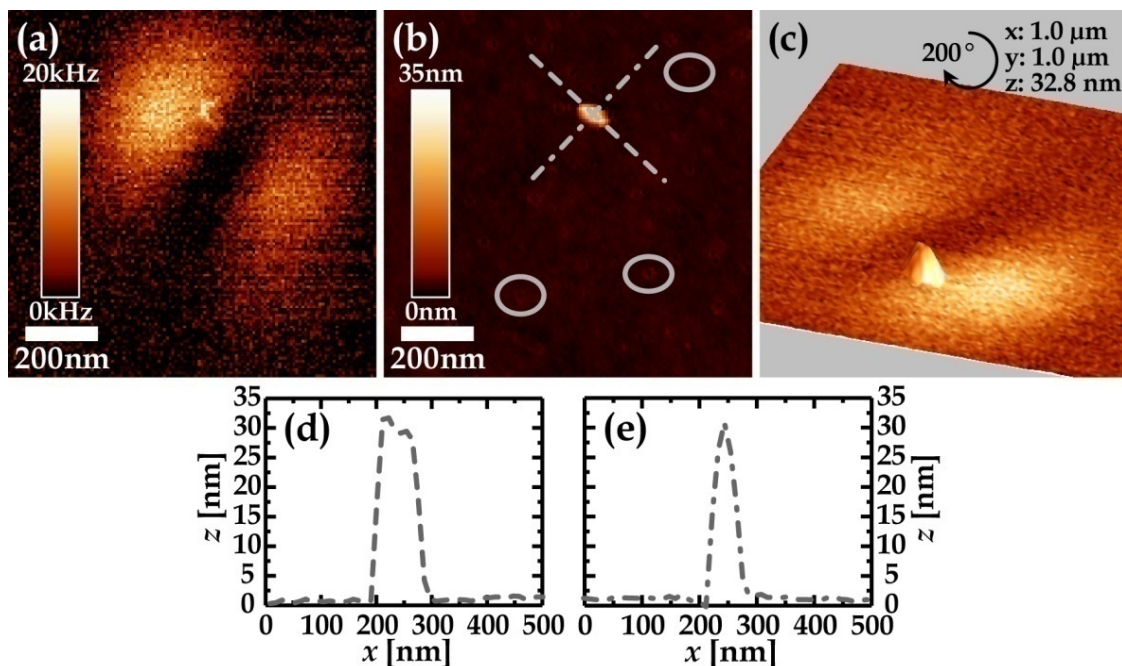

Figure 58: PL (a) and topography (b) data of an individual gold nanorod (RPDM at 633 nm). Profiles (d, e) along the grey dashed lines (a = 78 nm, b = 39 nm, h = 28 nm). Optical and topographic data are shifted due to misalignment of the scanning probe in focus. Consequently, the enhanced PL signal is not in the centre of the far-field pattern. Small pores in the glass substrate (encircled in grey) confirm tip sharpness. 3D topography plot (c) with the optical data as colour code shows highest PL emission at one particle tip. The image has been rotated as indicated by the black arrow at the top.

7.1 Excitation with a RPDM

The topography data reveals a reasonable particle size together with small glass pores (see Figure 58 b, encircled in grey), confirming tip sharpness. However, the physical tip shape does not necessarily have to resemble the optically active part of the probe. Although the tip induced highest PL emission is asymmetric, it is clearly located at one particle tip. Another asymmetric case is shown in Figure 59, where the topography data has to be treated carefully due to a considerable tip size. This is also reflected in the glass pores not being visible in Figure 59 b. Nevertheless, the asymmetric enhanced PL emission is highly localized (cf. Figure 59 a, c).
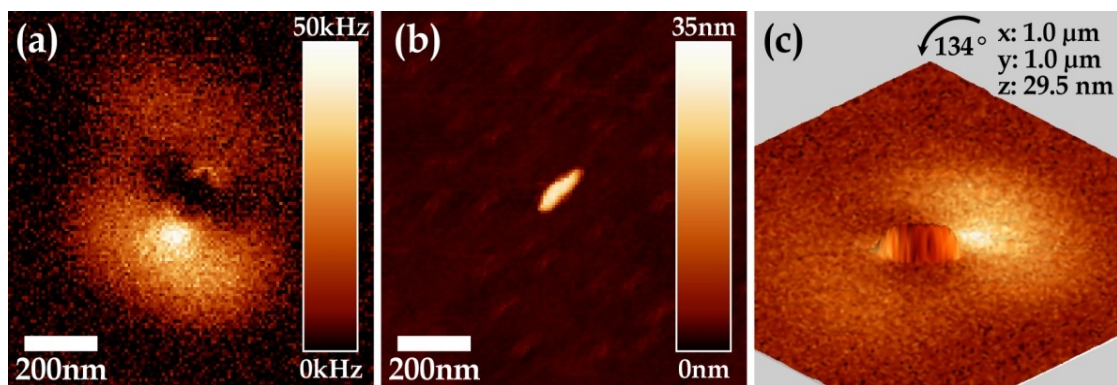
Figure 59: PL (a) and topography (b) data of an individual gold nanorod (RPDM at 633 nm). The topography has to be treated carefully due to tip deterioration. 3D topography plot (c) with the optical data as colour code. shows asymmetric enhanced PL emission at the particle's tips. The image has been rotated as indicated by the black arrow at the top:

Comparable data for two gold nanorods is shown in Figure 60. In the topography, small glass pores are only visible in the upper part of Figure 60 b (encircled in grey), indicating a change of the tip size and/or shape during scanning. Accordingly, the apparent particle shapes do not match their physical dimensions since the sizes of particles and tip are comparable. Taking into account the different particle orientations of about 60 °as mapped by the optical signal, the probe appears to be highly asymmetric. For particle I, orientation and overall shape from the topography agree with the optical pattern although that might be coincidentally. In contrast, this is not at all the case for particle II which appears rather spherical in the topography. A size estimation with these values is not substantially significant, but in combination with AFM values, a rough estimation of the (asymmetric) tip size can be obtained (cf. Table 9, p. 124). Besides the limited value of the topography data, the

optical image clearly indicates two single gold nanorods as well as their orientation. Combining the topography and optical data in Figure 60 c again shows a located PL emission peaking at the particles' tips.
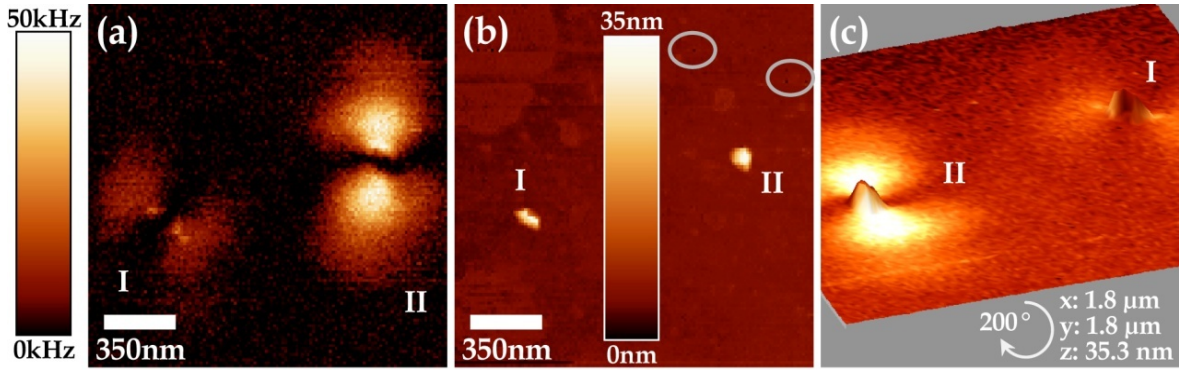
Figure 60: (a) PL and (b) topography data of two individual gold nanorods (RPDM at 633 nm). The topography data has to be treated carefully due to tip deterioration during the scan. However, a localized peaking of the PL can be recognized from (c), a 3D topography plot with the optical data as colour code. The image has been rotated as indicated by the white arrow at the bottom.

In the following, the PL SNOM images of the particles shown above are compared to the purely confocal case, *i.e.* with the probe being scanned over the sample and being fully retracted. For better comparison, confocal and SNOM images have the same intensity scale and are BG corrected. Profiles as taken along the grey dashed lines show the different PL intensities for both cases. The maximum intensity values for the confocal and near-field case were determined from the overall respective patterns (and not from the profiles). In Figure 61, the same particle is shown as in Figure 57. A considerably higher PL intensity in the vicinity of the gold probe is observed. The confocal intensity of 25 kHz increases to 56 kHz in the SNOM data, the intensity scale for both images was accordingly set to 0-40 kHz.

7.1 Excitation with a RPDM

Figure 61: (a) Confocal and (b) near-field PL data from an individual gold nanorod (RPDM at 633 nm, cf. Figure 57). Both images share the same intensity scale (0-40 kHz) and are BG corrected. Intensity profiles along the grey dashed lines are plotted in (e-h). Localized PL enhancement is observed at the particles' tips.

The intensity profile in Figure 61 d shows both the far- and near-field features. The far-field intensity is comparable to the confocal case (see Figure 61 c), while the enhanced emission is visible as additional sharp peaks. Because of the small size of the near-field pattern, this enhanced intensity is distributed over relatively few pixels which show considerable intensity variations. Hence, the pattern shows a higher asymmetry in the profile as expected from the image.

A somewhat lower intensity enhancement is observed for the particle in Figure 62 (cf. Figure 58). Only a slight enhancement from 22 to 26 kHz was found for this highly asymmetric case (see Figure 62). The intensity profiles in Figure 62 c, d again show a similar intensity for the far-field patterns with the increased near-field intensity as an additional spike. Although the tip was pretty sharp in this case ($d_{tip} \approx 16$ nm), the actual enhancement of an individual gold probe highly depends on its shape. In addition, the physical shape does not necessarily have to coincide with the optically active part.

Figure 62. (a) Confocal and (b) near-field PL data from an individual gold nanorod (RPDM at 633 nm, cf. Figure 58). Both images share the same intensity scale (0-20 kHz) and are BG corrected. Intensity profiles along the grey dashed lines are plotted in (e-h). PL enhancement is observed at one particle tip only.

Figure 63: (a) Confocal and (b) near-field PL data from an individual gold nanorod (RPDM at 633 nm, cf. Figure 59). Both images share the same intensity scale (0-50 kHz) and are BG corrected. Intensity profiles along the grey dashed lines are plotted in (e-h). An asymmetric localized PL enhancement is observed at the particles' tips.

7.1 Excitation with a RPDM

For the other asymmetric case, PL increases from 45 to 69 kHz (cf. Figure 63, Figure 59). The observed far-field intensities are again comparable (see Figure 63 c, d). Due to the central localization of the scanning probe in focus, the asymmetric spikes of the near-field intensity are observed in the centre of the far-field pattern.

Much lower values were observed for the particles in Figure 64 (cf. Figure 60). Again, the PL images in Figure 64 a, b share the same intensity scale (0-50 kHz). For convenience, the images are provided with an individually optimized scale in the insets (c, d).

PL intensity increases from 19 to 33 kHz (42 to 57 kHz) for particle I (II). The profile of particle I shows additional near-field peaks, while the far-field intensity is comparable to the confocal case (see Figure 64 e, d). For particle II, the enhancement might appear to be less localized from the profile (see Figure 64 g, h). However, the image (Figure 64 b) shows two sharp rims of strongest PL in the centre of the far-field pattern.
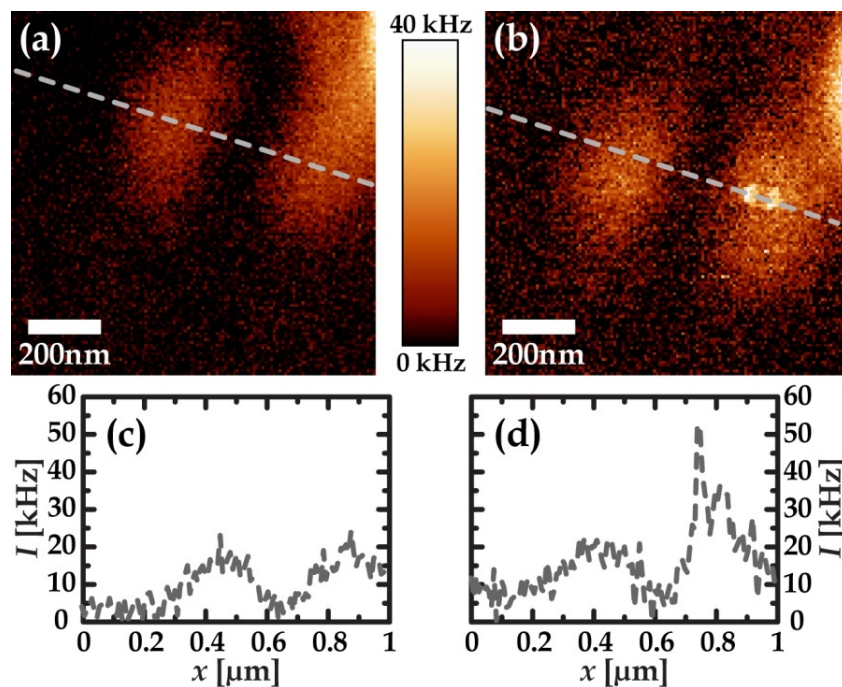
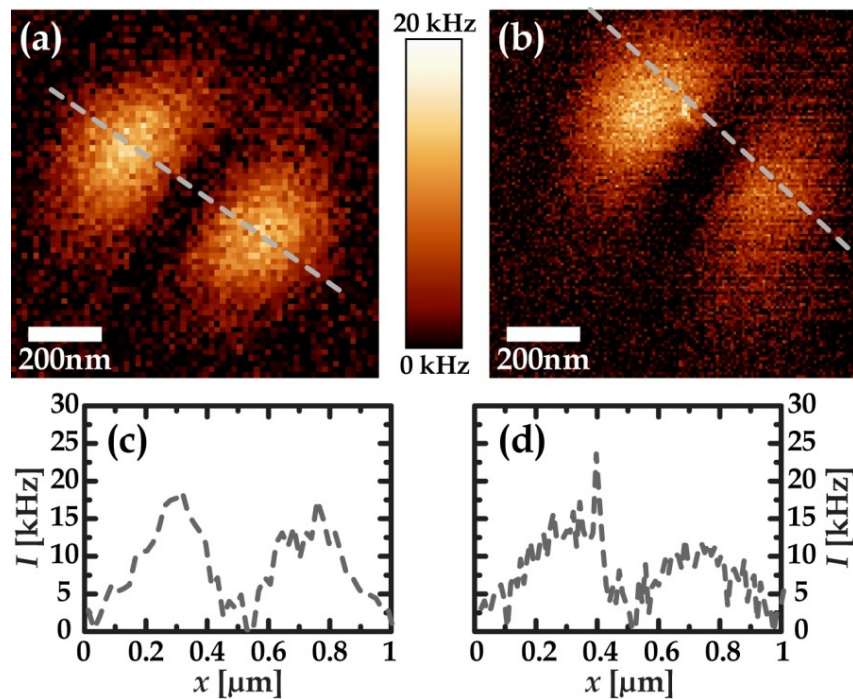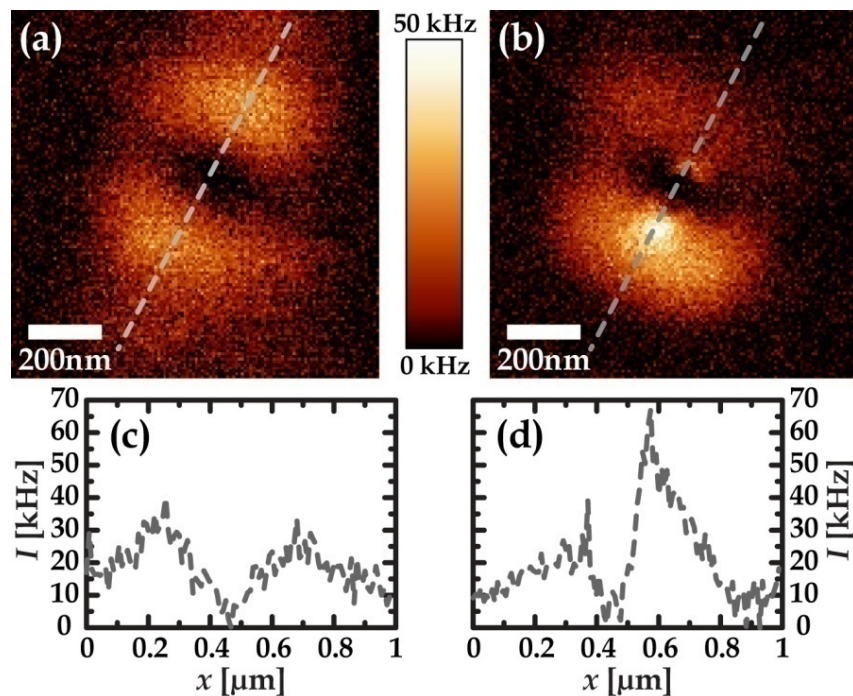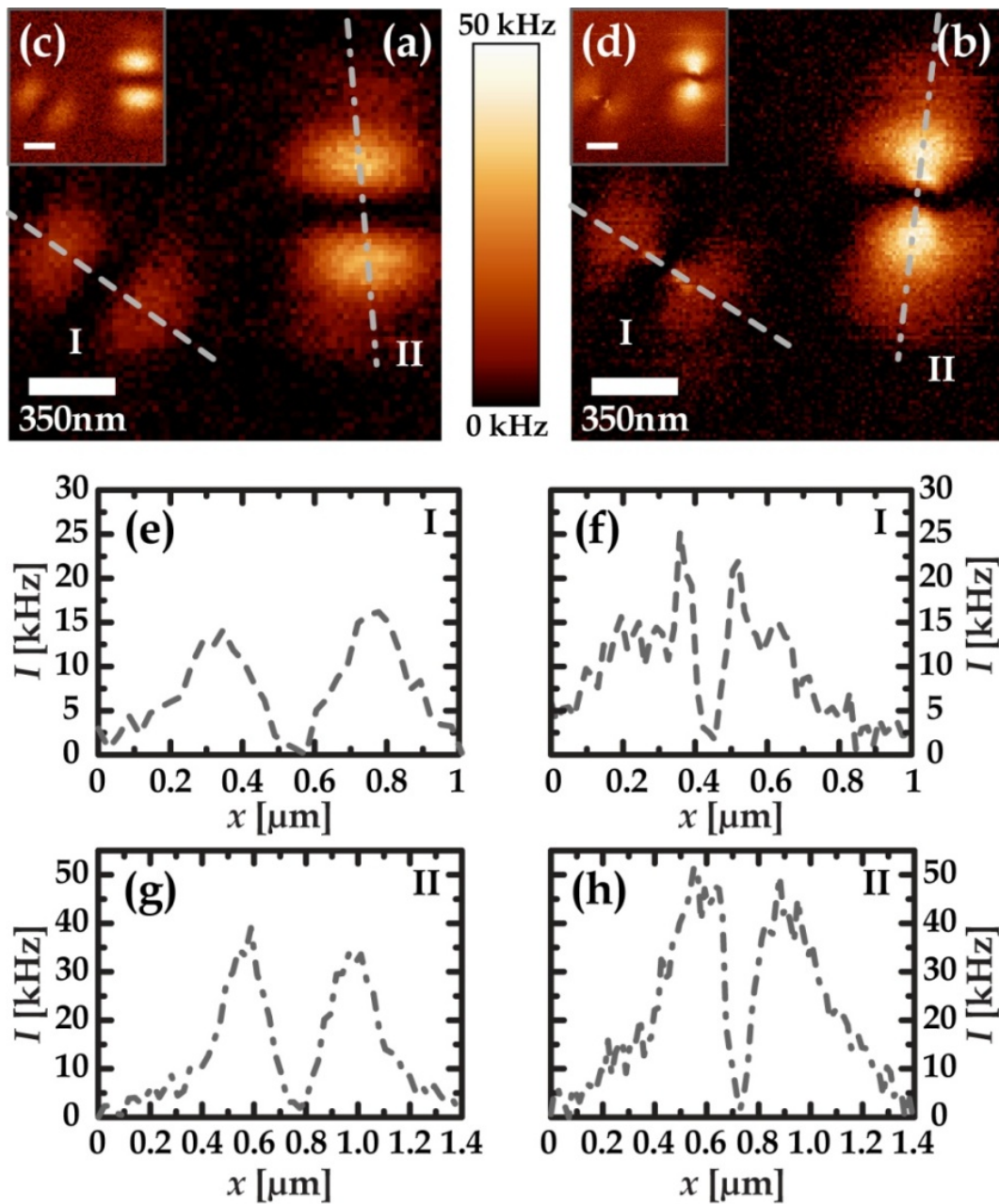Figure 64: (a) Confocal and (b) near-field PL data from two individual gold nanorods (I, II, RPDM at 633 nm, cf. Figure 60). Both images share the same intensity scale (0-50 kHz) and are BG corrected. The data is provided once again with individually adjusted intensity (c, d). Intensity profiles along the grey dashed lines are plotted in (e-h). PL enhancement is strongest at the particles' tips.

7.1 Excitation with a RPDM

To calculate enhancement factors, the PL induced by the near-field probe is compared to the purely confocal case, when the tip is not in the vicinity of the sample. Additionally, the different focal areas $A_{conf,NF}$ are taken into account:[165]

$$F_{enh} = \frac{I_{NF} \cdot A_{conf}}{I_{conf} \cdot A_{NF}} \tag{7.44}$$

The FWHM from intensity profiles served as a measure for the confocal area. For the near-field areas, estimated tip sizes (cf. Table 9, p. 124) were considered. An elliptic tip shape was assumed for the data in Figure 64. The resulting values are presented in Table 10.

Table 10: Experimental near-field enhancement factors F_{enh} of the PL for the gold nanorods shown above (RPDM at 633 nm). To determine the resulting enhancement, the different focal areas of the confocal and the near-field case were considered (see eq. 7.44).[165] Tip sizes were estimated from the topography data (cf. Table 9, p. 124). For Figure 64, an elliptic tip shape was assumed.

particle	confocal			near-field			F_{enh} [ ]
	I_{conf} [kHz]	FWHM [nm]	A_{conf} [m^2]	I_{NF} [kHz]	r_{tip} [nm]	A_{NF} [m^2]	
Figure 61	25	630	$3.1 \cdot 10^{-13}$	56	10.7	$3.6 \cdot 10^{-16}$	1900
Figure 62	22	600	$2.8 \cdot 10^{-13}$	26	8.2	$2.1 \cdot 10^{-16}$	1600
Figure 63	45	630	$3.1 \cdot 10^{-13}$	69	10.2	$3.3 \cdot 10^{-16}$	1500
Figure 64 I	19	620	$3.0 \cdot 10^{-13}$	57	23.2/28.7	$2.1 \cdot 10^{-15}$	250
Figure 64 II	42	610	$2.9 \cdot 10^{-13}$	33	23.2/28.7	$2.1 \cdot 10^{-15}$	200

For sharp tips, enhancement factors from 1500 to 2000 are found. When larger tip sizes are estimated, the enhancement factor drops accordingly. The main influence can be attributed to the area ratio, since the variation in the absolute intensity enhancement is less pronounced. Similar intensities are observed, regardless of the actual gold probe or nanorod in question. Even variations in the alignment of the probe in focus do not show a remarkable influence for the cases presented here.

7.2 Excitation with an APDM

Also with azimuthally polarized light, an enhanced PL signal can be extracted with a sharp gold probe, as shown in the following. However, there is no longitudinally polarized field component for an APDM. Therefore, the excitation of SPs along the tip-axis is not possible and consequently, the excitation field cannot be enhanced at the tip-apex. However, the gold probe may still act as an antenna, as may the gold particles. PL enhancement is observed at the tips of the particles, similarly to excitation with radially polarized light. Because of the different polarization properties of an APDM and a RPDM, the orientation of the patterns is different. The confocal far-field patterns of the two modes are turned by 90 ° relatively to each other. The near-field patterns, however, do not depend on the excitation mode. They are also of a somehow two-lobed shape because the particles' tips appear bright. Since they correspond to the actual physical orientation of the particle (as long as the scanning probe is small enough), their orientation does not depend on the excitation polarization. Consequently, the near-field pattern runs perpendicularly to the line connecting the two lobes for an APDM while it is parallel to this line for a RPDM. In other words, thinking of the far-field pattern as the "wings" of a butterfly, the near-field pattern forms its "body" for an APDM. In case of a RPDM, the far-field pattern is turned by 90 ° while the near-field pattern remains unaffected.

7.2 Excitation with an APDM
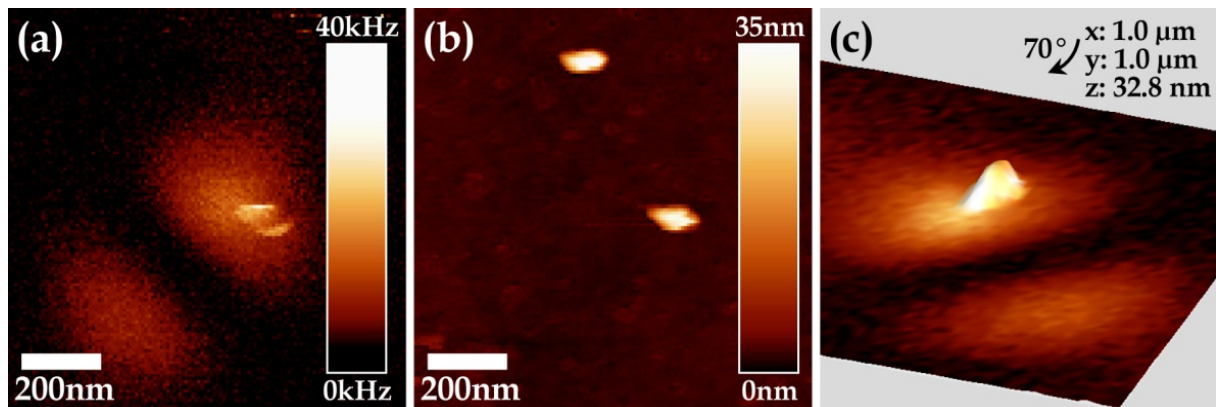
Figure 65: (a) PL and (b) topography data of a gold nanorod (APDM at 633 nm). Optical and topography data are shifted due to misalignment of the scanning probe in focus. Although the topography data does not clearly reveal the particle orientation, the characteristic optical pattern indicates both the orientation and the rod shape. 3D topography plot (c) with the optical data as colour code shows most intense PL at the particle's tips. The image has been rotated as indicated by the black arrow on top.

Although the topographic information in Figure 65 b is not totally clear because of tip deterioration, the particle's orientation is resembled as compared to the optical image (see Figure 65, a). The tip alignment was not perfectly realized, but since the probe was still inside the focus region, an enhanced PL signal could be collected. A 3D representation of the topographic data is provided in Figure 65 c with the optical image as colour code (please note that the image has been rotated for better visualization of the data as indicated by the black arrow at the top). A very similar situation is found in Figure 66, were another particle is imaged. The position of the probe is slightly different and tip alignment is not perfectly in the focus centre, but an enhanced PL signal could nevertheless be detected.
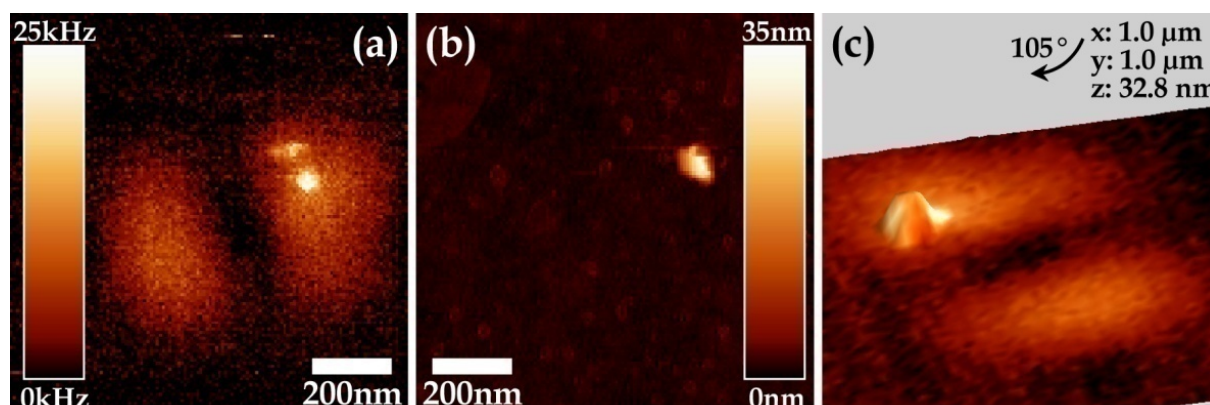
Figure 66: (a) PL and (b) topography data of a gold nanorod (APDM at 633 nm). Optical and topography data are shifted due to misalignment of the scanning probe in focus. Both the topography and the optical data clearly reveal the rod shape as well as the orientation of the particle. 3D topography plot (c) with the optical data as colour code shows highest PL emission at the particles' tips. The image has been rotated as indicated by the black arrow on top.

The strongest signal is clearly located at the ends of the particle and the shape as well as the orientation can be readily recognized both from the optical data and from the topographic information (cf. Figure 66 a, b). That the strongest PL correlates with the particle's tips is illustrated in the 3D topography plot in Figure 66 c, where the optical information is provided as colour code (please note that the 3D plot has been rotated for better visualization of the data as indicated by the black arrow at the top). The slight differences in the optical near-field and topographic data might result from the fact that not necessarily all parts of the scanning probe that contribute to the topography are also optically active. During the scanning process, the probe can pick up material from the sample surface which might alter the tip shape and consequently the topographic information. It can be also recognized from the representation of the pores in the glass surface in Figure 66 b that the gold tip was reasonably sharp when the image was acquired.

Confocal and near-field PL emission are compared in Figure 67, for the particle already shown in Figure 65. Intensity profiles as taken along the grey dashed lines are also provided.

7.2 Excitation with an APDM
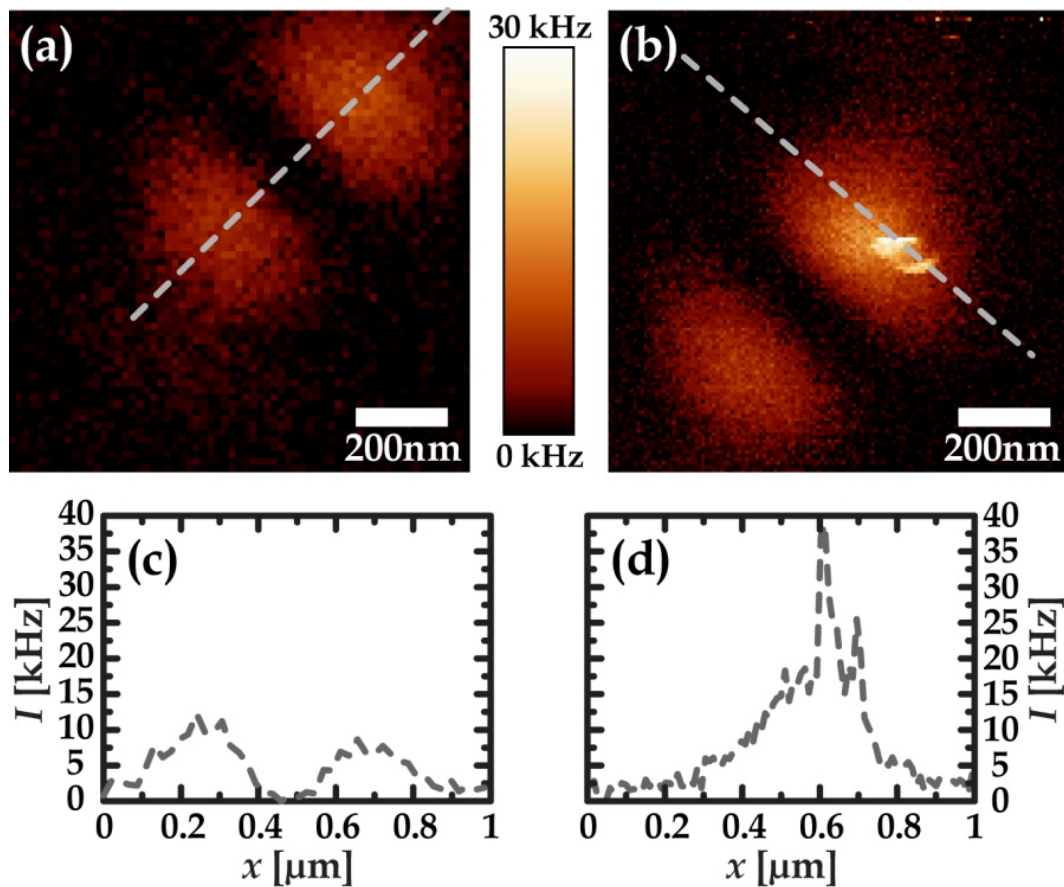
Figure 67: (a) Confocal and (b) near-field PL data from an individual gold nanorod (APDM at 633 nm, cf. Figure 65). Both images share the same intensity scale (0-30 kHz) and are BG corrected. (c, d) Intensity profiles along the grey dashed lines. The PL is enhanced when the gold probe is scanned over the particle compared to the purely confocal case while the enhancement is strongest at the particle's tips.

Similarly to excitation with an RPDM, a remarkable increase in PL intensity from 15 to 40 kHz is observed. Again, the highest intensity in the overall confocal or near-field pattern was taken, while FWHM values were extracted from the profiles to estimate the confocal area. Because of to the relative orientation of the far-field and near-field patterns, the profile in Figure 67 d shows only half of the far-field pattern. The far-field intensity is comparable to the confocal case (see Figure 67 c) with distinct peaks of enhanced PL.

For the particle shown in Figure 68 (cf. Figure 66), the intensity increases from 11 to 35 kHz. Again, similar far-field intensities are observed for both imaging modes as

can be recognized from the profiles in Figure 68 c, d. An enhanced PL emission is visible as sharp spikes on the far-field part in Figure 68 d.
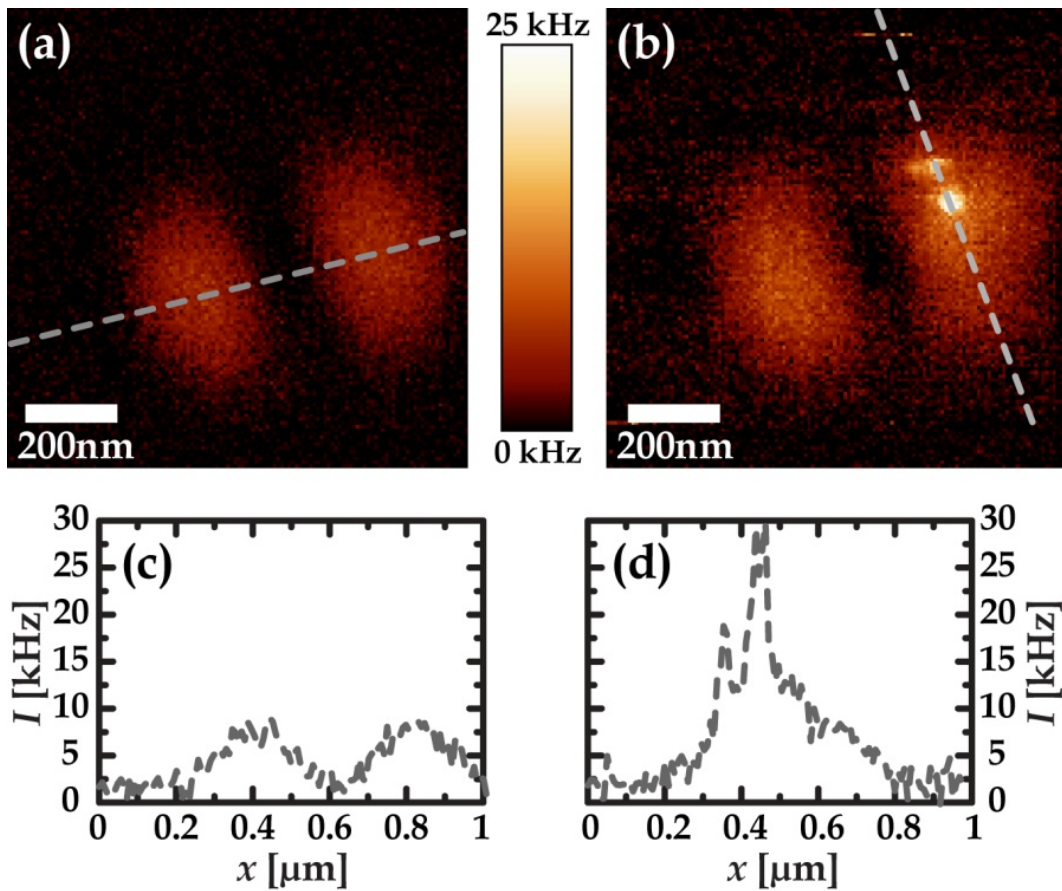
Figure 68: (a) Confocal and (b) near-field PL data from an individual gold nanorod (APDM at 633 nm, cf. Figure 66). Both images share the same intensity scale (0-25 kHz) and are BG corrected. The intensity profiles taken along the grey dashed lines are plotted in (c, d). The PL is enhanced when the gold probe is scanned over the particle compared to the purely confocal case while the enhancement is strongest at the particle's tips.

For excitation with an APDM, a similar PL enhancement was observed as upon excitation with radially polarized light. Consequently, enhancement factors were calculated accordingly (see eq. 7.44) as shown in Table 11.

7.2 Excitation with an APDM

Table 11: Experimental near-field enhancement factors F_{enh} of the PL for the two individual gold nanorods shown above (APDM at 633 nm). To determine the resulting enhancement, the different focal areas of the confocal and the near-field case were considered (see eq. 7.44). Tip sizes were estimated from the topography data (cf. Table 9, p. 124).

particle	confocal			near-field			F_{enh} [ ]
	I_{conf} [kHz]	FWHM [nm]	A_{conf} [m²]	I_{NF} [kHz]	r_{tip} [nm]	A_{NF} [m²]	
Figure 67	15	630	$3.1 \cdot 10^{-13}$	40	18.2	$1.0 \cdot 10^{-15}$	800
Figure 68	11	630	$3.1 \cdot 10^{-13}$	35	13.7	$5.9 \cdot 10^{-16}$	1700

Although only two particles were considered, the resulting enhancement factors in the order of 1000 to 2000 are pretty comparable to the values found for a RPDM. Again, the high dependency on the estimated tip size is obvious. Due to the APDM being purely transversally polarized, SPs in the gold probe cannot be excited along the tip-axis and the excitation field cannot be enhanced at the apex. However, the antenna effect can still be exploited to observe an enhanced PL signal from gold nanorods and should not be underestimated.

The enhancement factors observed upon excitation with either radially or azimuthally polarized light of approximately three orders of magnitude are ten times lower than found in a similar study involving gold nanocones performed in our group.[166] However, the system studied there forms a 3D bowtie antenna suggesting a stronger field enhancement. In addition, a parabolic mirror was used as focussing element, providing a higher intensity of the longitudinally polarized field component in focus. Thus, higher enhancement factors are to be expected and the values reported here appear to be reasonable.

8 Summary

The 2D orientation of individual gold nanorods can be precisely determined from their scattering as well as their photoluminescence (PL) pattern with confocal microscopy in combination with either an azimuthally or radially polarized doughnut mode (APDM or RPDM). The characteristic two-lobed patterns directly visualize the orientation of the particles and their shape does not depend on the detection mode as confirmed by *in situ* atomic force microscopy (AFM) measurements. Upon excitation with an APDM, the line connecting the two lobes runs perpendicular to the long particle axis, while for a RPDM, this line is oriented in parallel to the particle's long axis. In addition, differently shaped particles as gold nanospheres, nanorods or nanotriangles can be distinguished by the shape of their scattering or luminescence patterns. The orientation of nanotriangles is similarly reflected in the scattering or PL patterns upon excitation with DMs. The shape of the patterns in this case also critically depends on particle size. In general, an APDM is better suited to visualize the particle orientation of nanotriangles while a RPDM is the optimal choice to localize the particles because the acquired patterns are smaller.

A general benefit of detecting the PL light is that the images are almost background free and the SNR is usually improved compared to the scattering data. However, for particles at a glass-air interface, the sensitivity of the two imaging modes appears to be partly complementary. Although most particles are detected in both modes, a few are only visible upon either detecting the elastically scattered or the luminescent light. This effect can possibly be attributed to a different sensitivity of the two modes on particle size. Since the scattering intensity is caused by interference, the huge influence of the local particle environment on the phase term - which might become (almost) zero - is crucial. Because the PL signal is not affected by interference, the influence of the local environment is not as dramatic. Considering PL spectra of individual particles upon excitation at 633 nm, slight differences in the emission maxima could be observed. In addition, the spectral range does not coincide with the PL emission attributed to electron-hole recombination in

rough gold films or nanoparticles. Additionally, the excitation energy should not be sufficient to generate electron-hole pairs. Therefore, a plasmon-mediated process for the observed PL emission is suggested which would readily account for differences in the spectra being due to variations in the particle size and hence the SP resonances.

An arbitrary 3D orientation of gold nanorods embedded in a polymer film of polyvinylalcohol (PVA) leads to a variety of scattering patterns and different image contrasts. The patterns are considered in pairs for azimuthal and radial polarization and thus can be classified into different categories according to the observed image contrast and shape. Negative and positive contrast in both modes was observed, as well as negative contrast (APDM) in combination with positive contrast (RPDM). Regardless of the contrast combination, a transition of the pattern shape from two-lobed (comparable to the 2D case) over elongation of the modes to ring-shaped patterns was found. Especially upon excitation with a RPDM, some patterns show additional central features of inverted contrast. Comparing the experimental to theoretically simulated patterns, an estimation of the 3D orientation was feasible. The simulated patterns suggest a distinct dependence of the image contrast on particle size which corresponds to the experimental findings. The APDM appears to be more sensitive to changes of the out-of-plane angle θ for small values. The patterns acquired with a RPDM, on the other hand, show a stronger dependence of orientational changes for large values of θ. Consequently, the two modes nicely complement each other to determine the 3D particle orientation.

Scattering images for particles at interfaces with different refractive properties (glass-air, glass-water, glass-oil) were compared. An overall improve in image quality with a decreasing refractive index mismatch was observed. Variations in the signal intensity of individual particles can be attributed to size variations, as suggested by theoretical simulations. Additionally, the image acquisition process varies at the three studied interfaces. At the glass-air interface, the signal is formed by interference, while at the glass-oil interface, solely the light directly scattered by the particles is detected. Both interference and scattering contribute to the signal at

the glass-water interface. Consequently, the influence of particle size and particle environment changes for the three studied interfaces. The improved image quality is also reflected in an increasing SNR with decreasing refractive index mismatch. The preliminary data indicates that it should be possible to identify different interfaces by their SNR. For example, gold particles can be used to sense the direction of refractive index transition (from low *n* to high *n* or vice versa).

Gold nanoparticles are potential candidates for biological labelling, since they are taken up by cells without being cell-toxic. Preliminary results on fixed human cells (MR70) which were exposed to a solution of gold nanorods indicate that scattering microscopy with DMs allows for particle localization in cells. Particles were found both in close proximity of the cells and co-located with the cells (cytosol and nuclei). The observed patterns suggest a 3D orientation in the sample. Thus, the method appears to be feasible for the detection of individual particles in such a complex environment.

Apertureless scanning near-field optical microscopy (SNOM) measurements on individual gold nanorods show an enhanced PL emission at the particles' tips upon excitation with a RPDM. Both the gold nanorod and the sharp gold tip are expected to contribute to the observed field enhancement through the excitation of SPs. Enhancement factors taking into account the different focal areas (confocal vs. near-field) resulted in values of approximately three orders of magnitude. Upon excitation with an APDM, similar results showing an increased PL emission at the particles' tips were found, together with comparable enhancement factors. Due to the purely transversal polarization of an APDM, excitation of SPs in the tip should not occur. These results show that the antenna effect should not be underestimated, neither should the field enhancement from the particle itself.

9 Zusammenfassung

Die 2D Orientierung einzelner Goldnanostäbchen kann mit konfokaler Mikroskopie in Kombination mit azimutal oder radial polarisierten Doughnut-Moden (APDM/ RPDM) exakt bestimmt werden, sowohl durch Detektion der elastischen Streuung als auch der Photolumineszenz (PL). Die charakteristischen Flügelmuster bilden direkt die Partikelorientierung ab, wobei das entstehende Muster nicht von der Detektionsart (Streuung oder PL) abhängt, wie durch *in situ* Atomkraftmikroskopie (AFM) bestätigt werden konnte. Bei Anregung mit einem APDM steht die Verbindungslinie zwischen den zwei Flügeln demnach senkrecht zur langen Stäbchenachse, während sie für einen RPDM parallel verläuft. Zusätzlich lassen sich unterschiedliche Partikelformen wie Goldnanokugeln, -stäbchen oder –dreiecke aufgrund der Musterform sowohl in Streuung als auch durch PL unterscheiden. Auch die Orientierung von Nanodreiecken spiegelt sich in den Streu- oder PL-Mustern bei Verwendung von Doughnut-Moden (DM) wider. Außerdem hängt die Musterform bei Anregung mit DMs für Goldnanodreiecken entscheidend von der Partikelgröße ab. Allgemein ist dabei ein APDM besser zur Orientierungsabbildung geeignet, während die Partikel mit einem RPDM besonders gut lokalisiert werden können, da die entstehenden Muster kleiner sind.

Ein Vorteil der Detektion der PL ist, dass die Bilder beinahe frei von Hintergrundsignalen sind und das Signal-Rausch-Verhältnis (SNR) verbessert wird im Vergleich zur Streuung. Dabei ergänzt sich die Empfindlichkeit der beiden Abbildungsarten an Glas-Luft-Oberflächen teilweise. Obwohl hier die meisten Partikel in beiden Moden abgebildet werden können, sind einige nur in Streuung oder PL sichtbar. Dieser Effekt lässt sich höchstwahrscheinlich auf unterschiedliche Empfindlichkeiten der beiden Moden auf die Partikelgröße zurückführen. Da das Streusignal durch Interferenz zustande kommt, ist der Einfluss der lokalen Partikel-umgebung enorm. Über die Phasendifferenz kann der Interferenzterm - und damit das Signal - so (beinahe) verschwinden. Das PL-Signal wird dagegen nicht von Interferenz beeinflusst, weshalb die lokale Umgebung weniger wichtig ist. Die

gemessenen PL-Spektren einzelner Partikel (Anregung bei 633 nm) unterscheiden sich leicht in ihren Emissionsmaxima. Der Emissionsbereich unterscheidet sich von dem, der bei der PL rauer Goldfilme oder Nanopartikel auftritt, die auf die Rekombination von Elektron-Loch-Paaren zurückgeführt wird. Außerdem sollte die hier verwendete Anregungsenergie nicht ausreichen, um Elektron-Loch-Paare entstehen zu lassen. Daher liegt es nahe, die hier beschriebene PL-Emission auf eine Wechselwirkung mit Oberflächenplasmonen (SP) zurückzuführen, womit sich auch die Unterschiede in den Spektren mit einer Variation der Partikelgröße und damit der SP-Resonanzen erklären ließen.

Werden Goldnanostäbchen mit zufälliger 3D Orientierung in einen Polymerfilm aus Polyvinylalkohol (PVA) eingebettet, treten eine Vielzahl unterschiedlicher Streumuster sowie unterschiedliche Bildkontraste auf. Betrachtet man diese Muster für Anregung mit azimutaler und radialer Polarisation in Paaren, lassen sich diese in verschiedene Kategorien, sowohl nach Bildkontrast als auch nach Form, sortieren. Negativer und positiver Bildkontrast in beiden Anregungsmoden wurde genauso beobachtet wie die Kombination von negativem (APDM) und positivem (RPDM) Kontrast. Unabhängig vom Bildkontrast lässt sich ein Übergang von Flügelmustern (vergleichbar dem 2D Fall) über eine Verlängerung der Flügel hin zu ringförmigen Mustern beobachten. Besonders bei Anregung mit einem RPDM zeigen sich in einigen Mustern zusätzliche zentrale Bereiche mit invertiertem Kontrast. Durch den Vergleich der experimentellen Ergebnisse mit simulierten Mustern ist eine Abschätzung der 3D Partikelorientierung möglich. Die simulierten Muster weisen dabei auf einen großen Einfluss der Partikelgröße auf den Bildkontrast hin, was mit den experimentellen Ergebnissen übereinstimmt. Der Vergleich der beiden DM zeigt dabei eine unterschiedliche Empfindlichkeit auf Änderungen des polaren Winkels θ. Während der APDM stärker auf Änderungen für kleine Werte von θ reagiert, ist dies für den RPDM bei großen Werten von θ der Fall. Damit ergänzen sich die beiden Moden in der Bestimmung der 3D Partikelorientierung.

Beim Vergleich von Streubildern einzelner Partikel an Grenzflächen mit unterschiedlichen Brechungseigenschaften wurde eine Zunahme der Bildqualität bei abnehmendem Unterschied der Brechungsindices an der Grenzfläche beobachtet. Unterschiede in den Intensitäten einzelner Partikel lassen sich auf Größenvariationen zurückführen, was durch Simulationen gestützt wird. Außerdem unterscheidet sich die Bildentstehung an den drei betrachteten Grenzflächen. Während das Signal an der Glas-Luft-Grenzfläche durch Interferenz zustande kommt, wird an der Glas-Öl-Grenzfläche ausschließlich das direkt am Partikel gestreute Licht detektiert. Sowohl Interferenz als auch Streuung spielen dagegen an der Glas-Wasser-Grenzfläche eine entscheidende Rolle. Daher ändert sich der Einfluss der Partikelgröße und der lokalen Umgebung an den unterschiedlichen Grenzflächen. Die höhere Bildqualität spiegelt sich auch in der Zunahme des Signal-Rausch-Verhältnisses (SNR) mit abnehmendem Unterschied der Brechungsindices wider. Erste Ergebnisse deuten darauf hin, dass eine Bestimmung verschiedener Grenzflächen aufgrund des SNR möglich ist. So lässt sich mit Goldpartikeln beispielsweise die Richtung einer Änderung im Brechungsindex (niedrige n nach hohen n bzw. umgekehrt) detektieren.

Goldnanopartikel sind mögliche Kandidaten als biologische Marker, da sie von Zellen aufgenommen werden, ohne zelltoxisch zu sein. Erste Ergebnisse an fixierten menschlichen Zellen (MR70), die einer Lösung von Goldnanostäbchen ausgesetzt waren, weisen darauf hin, dass Streulichtmikroskopie mit DMs die Lokalisierung der Partikel in Zellen ermöglicht. Partikel wurden sowohl in direkter Nähe der Zellen gefunden, als auch kolokalisiert (Zytosol und Zellkerne). Die experimentell gefundenen Muster deuten auf eine 3D Partikelorientierung in der Probe hin. Die Methode scheint demnach die Detektion einzelner Nanopartikel selbst in so komplexer Umgebung zu ermöglichen.

Mit aperturloser Nahfeldmikroskopie (SNOM) an einzelnen Goldnanostäbchen konnte unter Anregung mit einem RPDM verstärkte PL-Emission an den Partikelenden festgestellt werden. Dabei wird erwartet, dass sowohl die Goldnano-

stäbchen als auch die dünne Goldspitze zu der beobachteten Feldverstärkung durch SP-Anregung beitragen. Verstärkungsfaktoren, bei denen die unterschiedlichen Fokusgrößen (konfokal vs. Nahfeld) berücksichtigt wurden, liegen im Bereich von drei Größenordnungen. Auch Anregung mit einem APDM führte zu vergleichbarer Verstärkung der PL an den Partikelenden. Aufgrund der rein transversalen Polarisation des APDM sollten SP in der Goldspitze nicht angeregt werden können. Die Ergebnisse deuten daher darauf hin, dass der Antenneneffekt ebenso wenig unterschätzt werden sollte wie die Feldverstärkung der Partikel.

10 References

[1]   Bundesinstitut für Risikobewertung, *Nanotechnologie - Einsatz, Trends und Risiken*. (2006), accessed on 15.02.2014; available from: http://www.bfr.bund.de/de/presseinformation/2006/09/nanotechnologie__ _einsatz__trends_und_risiken-7720.html.

[2]   E. Dulkeith, T. Niedereichholz, T. A. Klar, J. Feldmann, G. von Plessen, D. I. Gittins, K. S. Mayya and F. Caruso, *Plasmon Emission in Photoexcited Gold Nanoparticles.* Phys. Rev. B (2004) **70**, p. 205424.

[3]   P. Apell, R. Monreal and S. Lundqvist, *Photoluminescence of Noble Metals.* Phys. Scr. (1988) **38**, p. 174.

[4]   G. T. Boyd, Z. H. Yu and Y. R. Shen, *Photoinduced Luminescence from the Noble Metals and its Enhancement on Roughened Surfaces.* Phys. Rev. B (1986) **33**, p. 7923.

[5]   J. P. Wilcoxon, J. E. Martin, F. Parsapour, B. Wiedenman and D. F. Kelley, *Photoluminescence from Nanosize Gold Clusters.* J. Chem. Phys. (1998) **108**, p. 9137.

[6]   Y.-N. Hwang, D. H. Jeong, H. J. Shin, D. Kim, S. C. Jeoung, S. H. Han, J.-S. Lee and G. Cho, *Femtosecond Emission Studies on Gold Nanoparticles.* J. Phys. Chem. B (2002) **106**, p. 7581.

[7]   M. B. Mohamed, V. Volkov, S. Link and M. A. El-Sayed, *The 'Lightning' Gold Nanorods: Fluorescence Enhancement of over a Million Compared to the Gold Metal.* Chem. Phys. Lett. (2000) **317**, p. 517.

[8]   S. Eustis and M. El-Sayed, *Aspect Ratio Dependence of the Enhanced Fluorescence Intensity of Gold Nanorods: Experimental and Simulation Study.* J. Phys. Chem. B (2005) **109**, p. 16350.

[9]   O. P. Varnavski, M. B. Mohamed, M. A. El-Sayed and T. Goodson, *Relative Enhancement of Ultrafast Emission in Gold Nanorods.* J. Phys. Chem. B (2003) **107**, p. 3101.

[10]   O. P. Varnavski, T. Goodson, M. B. Mohamed and M. A. El-Sayed, *Femtosecond Excitation Dynamics in Gold Nanospheres and Nanorods.* Phys. Rev. B (2005) **72**, p. 235405.

[11]   K. Imura, T. Nagahara and H. Okamoto, *Plasmon Mode Imaging of Single Gold Nanorods.* J. Am. Chem. Soc. (2004) **126**, p. 12730.

[12]   K. Imura, T. Nagahara and H. Okamoto, *Near-Field Two-Photon-Induced Photoluminescence from Single Gold Nanorods and Imaging of Plasmon Modes.* J. Phys. Chem. B (2005) **109**, p. 13214.

[13]   A. Mooradian, *Photoluminescence of Metals.* Phys. Rev. Lett. (1969) **22**, p. 185.

[14]   T. Züchner, A. V. Failla and A. J. Meixner, *Light Microscopy with Doughnut Modes: A Concept to Detect, Characterize, and Manipulate Individual Nanoobjects.* Angew. Chem. Int. Ed. (2011) **50**, p. 5274.

[15]   S. Kawata, M. Ohtsu and M. Irie, *Nano-optics.* Springer Series in Optical Sciences, Springer Verlag, Berlin Heidelberg (2002).

[16]   L. Novotny and B. Hecht, *Principles of Nano-Optics*, Cambridge University Press, Cambridge (2006).

[17] W. Chen and Q. Zhan, *Realization of an Evanescent Bessel Beam via Surface Plasmon Interference Excited by a Radially Polarized Beam.* Opt. Lett. (2009) **34**, p. 722.

[18] T. Grosjean and D. Courjon, *Immaterial Tip Concept by Light Confinement.* J. Microsc. (2001) **202**, p. 273.

[19] T. Grosjean, D. Courjon and D. van Labeke, *Bessel Beams as Virtual Tips for Near-Field Optics.* J. Microsc. (2003) **210**, p. 319.

[20] H. Kano, S. Mizuguchi and S. Kawata, *Excitation of Surface-Plasmon Polaritons by a Focused Laser Beam.* J. Opt. Soc. Am. B (1998) **15**, p. 1381.

[21] K. J. Moh, X.-C. Yuan, J. Bu, S. W. Zhu and B. Z. Gao, *Surface Plasmon Resonance Imaging of Cell-Substrate Contacts with Radially Polarized Beams.* Opt. Express (2008) **16**, p. 20734.

[22] K. Watanabe, N. Horiguchi and H. Kano, *Optimized Measurement Probe of the Localized Surface Plasmon Microscope by Using Radially Polarized Illumination.* Appl. Opt. (2007) **46**, p. 4985.

[23] Q. Zhan, *Evanescent Bessel Beam Generation via Surface Plasmon Resonance Excitation by a Radially Polarized Beam.* Opt. Lett. (2006) **31**, p. 1726.

[24] K. Yoshiki, M. Hashimoto and T. Araki, *Second-Harmonic-Generation Microscopy Using Excitation Beam with Controlled Polarization Pattern to Determine Three-Dimensional Molecular Orientation.* Jpn. J. Appl. Phys. (2005) **44**, p. L1066.

[25] K. Yoshiki, K. Ryosuke, M. Hashimoto, N. Hashimoto and T. Araki, *Second-Harmonic-Generation Microscope Using Eight-Segment Polarization-Mode Converter to Observe Three-Dimensional Molecular Orientation.* Opt. Lett. (2007) **32**, p. 1680.

[26] S. W. Hell and J. Wichmann, *Breaking the Diffraction Resolution Limit by Stimulated Emission: Stimulated-Emission-Depletion Fluorescence Microscopy.* Opt. Lett. (1994) **19**, p. 780.

[27] H. Kawauchi, K. Yonezawa, Y. Kozawa and S. Sato, *Calculation of Optical Trapping Forces on a Dielectric Sphere in the Ray Optics Regime Produced by a Radially Polarized Laser Beam.* Opt. Lett. (2007) **32**, p. 1839.

[28] K. C. Neuman and S. M. Block, *Optical Trapping.* Rev. Sci. Instrum. (2004) **75**, p. 2787.

[29] T. A. Nieminen, N. R. Heckenberg and H. Rubinsztein-Dunlop, *Forces in Optical Tweezers with Radially and Azimuthally Polarized Trapping Beams.* Opt. Lett. (2008) **33**, p. 122.

[30] S. Yan and B. Yao, *Radiation Forces of a Highly Focused Radially Polarized Beam on Spherical Particles.* Phys. Rev. A: At., Mol., Opt. Phys. (2007) **76**, p. 053836.

[31] Q. Zhan, *Trapping Metallic Rayleigh Particles with Radial Polarization.* Opt. Express (2004) **12**, p. 3377.

[32] D. W. Zhang and X.-C. Yuan, *Optical Doughnut for Optical Tweezers.* Opt. Lett. (2003) **28**, p. 740.

[33] M. Meier, V. Romano and T. Feurer, *Material Processing with Pulsed Radially and Azimuthally Polarized Laser Radiation.* Appl. Phys. A: Mater. Sci. Process. (2007) **86**, p. 329.

[34] V. G. Niziev and A. V. Nesterov, *Influence of Beam Polarization on Laser Cutting Efficiency.* J. Phys. D: Appl. Phys. (1999) **32**, p. 1455.

[35] A. V. Failla, S. Jäger, T. Züchner, M. Steiner and A. J. Meixner, *Topology Measurements of Metal Nanoparticles with 1 nm Accuracy by Confocal Interference Scattering Microscopy.* Opt. Express (2007) **15**, p. 8532.

[36] A. V. Failla, H. Qian, H. Qian, A. Hartschuh and A. J. Meixner, *Orientational Imaging of Subwavelength Au Particles with Higher Order Laser Modes.* Nano Lett. (2006) **6**, p. 1374.

[37] F. Wackenhut, A. V. Failla and A. J. Meixner, *Sensing Dielectric Media on the Nanoscale with Freely Oriented Gold Nanorods.* Phys. Chem. Chem. Phys. (2013) **15**, p. 5407.

[38] F. Wackenhut, A. Virgilio Failla, T. Züchner, M. Steiner and A. J. Meixner, *Three-Dimensional Photoluminescence Mapping and Emission Anisotropy of Single Gold Nanorods.* Appl. Phys. Lett. (2012) **100**, p. 263102.

[39] T. Züchner, A. V. Failla, A. Hartschuh and A. J. Meixner, *A Novel Approach to Detect and Characterize the Scattering Patterns of Single Au Nanoparticles Using Confocal Microscopy.* J. Microsc. (2008) **229**, p. 337.

[40] T. Züchner, A. V. Failla, M. Steiner and A. J. Meixner, *Probing Dielectric Interfaces on the Nanoscale with Elastic Scattering Patterns of Single Gold Nanorods.* Opt. Express (2008) **16**, p. 14635.

[41] T. Züchner, F. Wackenhut, A. V. Failla and A. J. Meixner, *Nanoscale Characterization of Single Au Nanorods by Confocal Microscopy.* Appl. Surf. Sci. (2009) **255**, p. 5391.

[42] E. E. Connor, J. Mwamuka, A. Gole, C. J. Murphy and M. D. Wyatt, *Gold Nanoparticles Are Taken Up by Human Cells but Do Not Cause Acute Cytotoxicity.* Small (2005) **1**, p. 325.

[43] T. S. Hauck, A. A. Ghazani and W. C. W. Chan, *Assessing the Effect of Surface Chemistry on Gold Nanorod Uptake, Toxicity, and Gene Expression in Mammalian Cells.* Small (2008) **4**, p. 153.

[44] D. Nagesha, G. S. Laevsky, P. Lampton, R. Banyal, C. Warner, C. DiMarzio and S. Sridhar, *In Vitro Imaging of Embryonic Stem Cells Using Multiphoton Luminescence of Gold Nanoparticles.* Int. J. Nanomed. (2007) **2**, p. 813.

[45] G. Mie, *Beiträge zur Optik trüber Medien, speziell kolloidaler Metallösungen.* Ann. Phys. (1908) **330**, p. 377.

[46] R. Gans, *Über die Form ultramikroskopischer Goldteilchen.* Ann. Phys. (1912) **342**, p. 881.

[47] C. F. Bohren and D. R. Huffman, *Absorption and Scattering of Light by Small Particles*, John Wiley & Sons, New York (1983).

[48] H. Niedrig, *Optik: Wellen- und Teilchenoptik.* Bergmann Schaefer: Lehrbuch der Experimentalphysik, Band 3, 10. Auflage, Walter de Gruyter, Berlin (2004).

[49] D. Meschede, *Optik, Licht und Laser.* 3. Auflage, Vieweg + Teubner, Wiesbaden (2008).

[50] K. S. Youngworth and T. G. Brown, *Focusing of High Numerical Aperture Cylindrical-Vector Beams.* Opt. Express (2000) **7**, p. 77.

[51] N. K. Viswanathan and V. V. G. Inavalli, *Generation of Optical Vector Beams Using a Two-Mode Fiber.* Opt. Lett. (2009) **34**, p. 1189.

[52] Q. Zhan, *Radiation Forces on a Dielectric Sphere Produced by Highly Focused Cylindrical Vector Beams.* J. Opt. A: Pure Appl. Opt. (2003) **5**, p. 229.

[53] G. M. Lerman, Y. Lilach and U. Levy, *Demonstration of Spatially Inhomogeneous Vector Beams with Elliptical Symmetry.* Opt. Lett. (2009) **34**, p. 1669.

[54] N. Davidson and N. Bokor, *High-Numerical-Aperture Focusing of Radially Polarized Doughnut Beams with a Parabolic Mirror and a Flat Diffractive Lens.* Opt. Lett. (2004) **29**, p. 1318.

[55] M. Steiner, F. Schleifenbaum, C. Stupperich, A. V. Failla, A. Hartschuh and A. J. Meixner, *Microcavity-Controlled Single-Molecule Fluorescence.* ChemPhysChem (2005) **6**, p. 2190.

[56] K. Sakai and S. Noda, *Optical Trapping of Metal Particles in Doughnut-Shaped Beam Emitted by Photonic-Crystal Laser.* IET Electron. Lett. (2007) **43**, p. 107.

[57] S. Quabis, R. Dorn, M. Eberler, O. Glöckl and G. Leuchs, *Focusing Light to a Tighter Spot.* Opt. Commun. (2000) **179**, p. 1.

[58] S. Quabis, R. Dorn, M. Eberler, O. Glöckl and G. Leuchs, *The Focus of Light – Theoretical Calculation and Experimental Tomographic Reconstruction.* Appl. Phys. B: Lasers Opt. (2001) **72**, p. 109.

[59] S. Quabis, R. Dorn and G. Leuchs, *Generation of a Radially Polarized Doughnut Mode of High Quality.* Appl. Phys. B: Lasers Opt. (2005) **81**, p. 597.

[60] E. Wolf, *Electromagnetic Diffraction in Optical Systems. I. An Integral Representation of the Image Field.* Proc. R. Soc. London, Ser. A (1959) **253**, p. 349.

[61] M. Born and E. Wolf, *Principles of Optics.* 5th Edition, Pergamon Press, Oxford (1975).

[62] B. Richards and E. Wolf, *Electromagnetic Diffraction in Optical Systems. II. Structure of the Image Field in an Aplanatic System.* Proc. R. Soc. London, Ser. A (1959) **253**, p. 358.

[63] R. Dorn, S. Quabis and G. Leuchs, *Sharper Focus for a Radially Polarized Light Beam.* Phys. Rev. Lett. (2003) **91**, p. 233901.

[64] J. R. Zurita-Sánchez and L. Novotny, *Multipolar Interband Absorption in a Semiconductor Quantum Dot. II. Magnetic Dipole Enhancement.* J. Opt. Soc. Am. B (2002) **19**, p. 2722.

[65] U. Kreibig and M. Vollmer, *Optical Properties of Metal Clusters.* Springer Series in Materials Science, Vol. 25, Springer-Verlag, Berlin (1995).

[66] I. B. Dold and R. Mecke, *Optical Properties of Noble Metals, Transition Metals, and their Alloys in the Infrared.* Optik (Jena, Ger.) (1965) **22**, p. 435.

[67] G. A. Bolotin, A. N. Voloshinkii, M. M. Kirillova, M. M. Noskov, A. V. Sokolov and B. A. Charikov, *Optical Properties of Ti and V in the Infrared Spectral Region.* Fiz. Met. Metalloved. (1962) **13**, p. 823.

[68] L. G. Schulz, *The Optical Constants of Silver, Gold, Copper, and Aluminum. I. The Absorption Coefficient k.* J. Opt. Soc. Am. (1954) **44**, p. 357.

[69] L. R. Canfield, G. Hass and W. R. Hunter, *The Optical Properties of Evaporated Gold in the Vacuum Ultraviolet from 300 Å to 2000 Å.* J. Phys. France (1964) **25**, p. 124.

[70] M.-L. Thèye, *Investigation of the Optical Properties of Au by Means of Thin Semitransparent Films.* Phys. Rev. B (1970) **2**, p. 3060.

[71] G. B. Irani, T. Huen and F. Wooten, *Optical Constants of Silver and Gold in the Visible and Vacuum Ultraviolet.* J. Opt. Soc. Am. (1971) **61**, p. 128.

[72] P. B. Johnson and R. W. Christy, *Optical Constants of the Noble Metals.* Phys. Rev. B (1972) **6**, p. 4370.

[73] H. J. Hagemann, W. Gudat and C. Kunz, *Optical Constants from the Far Infrared to the X-Ray Region: Mg, Al, Cu, Ag, Au, Bi, C, and Al$_2$O$_3$.* J. Opt. Soc. Am. (1975) **65**, p. 742.

[74] H.-J. Hagemann, W. Gudat and C. Kunz, *Optical Constants from the Far Infrared to the X-ray region: Mg,Al,Cu,Ag,Au,Bi,C and Al.* Deutsches Elektronen-Synchroton Report DESY SR-74/7, Hamburg (1974).

[75] L. G. Schulz and F. R. Tangherlini, *Optical Constants of Silver, Gold, Copper, and Aluminum. II. The Index of Refraction n.* J. Opt. Soc. Am. (1954) **44**, p. 362.

[76] K. Weiß, *Optical Constants and Electrical Resistance of Thick Metal Layers.* Z. Naturforsch. (1948) **3a**, p. 143.

[77] M. Otter, *Optische Konstanten massiver Metalle.* Z. Phys. A: Hadrons Nucl. (1961) **161**, p. 163.

[78] V. G. Padalka and I. N. Shklyarevskii, *Determination of the Microcharacteristics of Silver and Gold by Optical Constants in the Infrared Spectrum Region, and the Specific Conductance at 82 and 295°K.* Opt. Spektrosk. (1961) **11**, p. 527.

[79] M. Guerrisi, R. Rosei and P. Winsemius, *Splitting of the Interband Absorption Edge in Au.* Phys. Rev. B (1975) **12**, p. 557.

[80] U. Kreibig, *Electronic Properties of Small Silver Particles: the Optical Constants and Their Temperature Dependence.* J. Phys. F: Met. Phys. (1974) **4**, p. 999.

[81] P. Debye, *Der Lichtdruck auf Kugeln von beliebigem Material.* Ann. Phys. (1909) **335**, p. 57.

[82] L. Lorenz, *Lysbevægelsen i og uden for en af plane Lysbølger belyst Kugle.* Det Kongelige Danske Videnskabernes Selskabs Skrifter (1890) **6**, p. 1.

[83] M. Kerker, *The Scattering of Light, and Other Electromagnetic Radiation.* Physical Chemistry, Vol. 16, Academic Press, New York (1969).

[84] U. Kreibig, *Hundert Jahre Mie-Theorie. Optische Eigenschaften von Nanopartikeln.* Phys. Unserer Zeit (2008) **39**, p. 281.

[85] U. Kreibig, *Hundert Jahre Mie-Theorie. Optische Eigenschaften von Nanopartikeln.* Phys. Unserer Zeit (2008) **39**, Ergänzung.

[86] M. A. Yurkin and A. G. Hoekstra, *The Discrete Dipole Approximation: An Overview and Recent Developments.* J. Quant. Spectrosc. Radiat. Transfer (2007) **106**, p. 558.

[87] T. Züchner, *Neuartige Streulichtmikroskopie an einzelnen Goldnanopartikeln.* Diploma thesis, Eberhard Karls Universität Tübingen (2006).

[88] C. J. R. Sheppard and D. M. Shotton, *Confocal Laser Scanning Microscopy*, BIOS Scientific Publishers, London (1997).

[89] R. H. Webb, *Confocal Optical Microscopy.* Rep. Prog. Phys. (1996) **59**, p. 427.

[90] B. R. Boruah and M. A. A. Neil, *Laser Scanning Confocal Microscope with Programmable Amplitude, Phase, and Polarization of the Illumination Beam.* Rev. Sci. Instrum. (2009) **80**, p. 013705.

[91] S. W. Hell, *Far-Field Optical Nanoscopy.* Science (2007) **316**, p. 1153.

[92] K. L. Kelly, E. Coronado, L. L. Zhao and G. C. Schatz, *The Optical Properties of Metal Nanoparticles: The Influence of Size, Shape, and Dielectric Environment.* J. Phys. Chem. B (2003) **107**, p. 668.

[93] C. J. Murphy, T. K. Sau, A. M. Gole, C. J. Orendorff, J. Gao, L. Gou, S. E. Hunyadi and T. Li, *Anisotropic Metal Nanoparticles: Synthesis, Assembly, and Optical Applications.* J. Phys. Chem. B (2005) **109**, p. 13857.

[94] J. Pérez-Juste, I. Pastoriza-Santos, L. M. Liz-Marzán and P. Mulvaney, *Gold Nanorods: Synthesis, Characterization and Applications.* Coord. Chem. Rev. (2005) **249**, p. 1870.

[95] B. Nikoobakht and M. A. El-Sayed, *Preparation and Growth Mechanism of Gold Nanorods (NRs) Using Seed-Mediated Growth Method.* Chem. Mater. (2003) **15**, p. 1957.

[96] A. M. van Oijen, J. Köhler, J. Schmidt, M. Müller and G. J. Brakenhoff, *3-Dimensional Super-Resolution by Spectrally Selective Imaging.* Chem. Phys. Lett. (1998) **292**, p. 183.

[97] A. Lewis, M. Isaacson, A. Harootunian and A. Muray, *Development of a 500 Å Spatial Resolution Light Microscope: I. Light is Efficiently Transmitted Through λ/16 Diameter Apertures.* Ultramicroscopy (1984) **13**, p. 227.

[98] D. W. Pohl, W. Denk and M. Lanz, *Optical Stethoscopy: Image Recording with Resolution λ/20.* Appl. Phys. Lett. (1984) **44**, p. 651.

[99] A. Hartschuh, *Tip-Enhanced Near-Field Optical Microscopy.* Angew. Chem. Int. Ed. (2008) **47**, p. 8178.

[100] V. Deckert, D. Zeisel, R. Zenobi and T. Vo-Dinh, *Near-Field Surface-Enhanced Raman Imaging of Dye-Labeled DNA with 100-nm Resolution.* Anal. Chem. (1998) **70**, p. 2646.

[101] N. Hayazawa, Y. Inouye, Z. Sekkat and S. Kawata, *Metallized Tip Amplification of Near-Field Raman Scattering.* Opt. Commun. (2000) **183**, p. 333.

[102] E. M. Purcell, *Proceedings of the American Physical Society.* Phys. Rev. (1946) **69**, p. 674.

[103] H. Metiu, *Surface Enhanced Spectroscopy.* Prog. Surf. Sci. (1984) **17**, p. 153.

[104] H. Xu, J. Aizpurua, auml, M. ll and P. Apell, *Electromagnetic Contributions to Single-Molecule Sensitivity in Surface-Enhanced Raman Scattering.* Phys. Rev. E (2000) **62**, p. 4318.

[105] F. R. Aussenegg, A. Leitner, M. E. Lippitsch, H. Reinisch and M. Riegler, *Novel Aspects of Fluorescence Lifetime for Molecules Positioned Close to Metal Surfaces.* Surf. Sci. (1987) **189-190**, p. 935.

[106] P. Anger, P. Bharadwaj and L. Novotny, *Enhancement and Quenching of Single-Molecule Fluorescence.* Phys. Rev. Lett. (2006) **96**, p. 113002.

[107] F. Cannone, G. Chirico, A. R. Bizzarri and S. Cannistraro, *Quenching and Blinking of Fluorescence of a Single Dye Molecule Bound to Gold Nanoparticles.* J. Phys. Chem. B (2006) **110**, p. 16491.

[108] Y. Chen, K. Munechika and D. S. Ginger, *Dependence of Fluorescence Intensity on the Spectral Overlap between Fluorophores and Plasmon Resonant Single Silver Nanoparticles.* Nano Lett. (2007) **7**, p. 690.

[109] E. Dulkeith, A. C. Morteani, T. Niedereichholz, T. A. Klar, J. Feldmann, S. A. Levi, F. C. J. M. van Veggel, D. N. Reinhoudt, M. Moller and D. I. Gittins, *Fluorescence Quenching of Dye Molecules near Gold Nanoparticles: Radiative and Nonradiative Effects.* Phys. Rev. Lett. (2002) **89**, p. 203002/1.

[110] E. Dulkeith, M. Ringler, T. A. Klar, J. Feldmann, A. M. Javier and W. J. Parak, *Gold Nanoparticles Quench Fluorescence by Phase Induced Radiative Rate Suppression.* Nano Lett. (2005) **5**, p. 585.

[111] T. Härtling, P. Reichenbach and L. M. Eng, *Near-Field Coupling of a Single Fluorescent Molecule and a Spherical Gold Nanoparticle.* Opt. Express (2007) **15**, p. 12806.

[112] S. Kühn, U. Hakanson, L. Rogobete and V. Sandoghdar, *Enhancement of Single-Molecule Fluorescence Using a Gold Nanoparticle as an Optical Nanoantenna.* Phys. Rev. Lett. (2006) **97**, p. 0174021.

[113] C. Li, X. Liu, M. Yuan, J. Li, Y. Guo, J. Xu, M. Zhu, J. Lv, H. Liu and Y. Li, *Unusual Fluorescence Enhancement of a Novel Carbazolyldiacetylene Bound to Gold Nanoparticles.* Langmuir (2007) **23**, p. 6754.

[114] O. L. Muskens, V. Giannini, J. A. Sanchez-Gil and J. GomezRivas, *Strong Enhancement of the Radiative Decay Rate of Emitters by Single Plasmonic Nanoantennas.* Nano Lett. (2007, p.

[115] N. Nerambourg, M. H. V. Werts, M. Charlot and M. Blanchard-Desce, *Quenching of Molecular Fluorescence on the Surface of Monolayer-Protected Gold Nanoparticles Investigated Using Place Exchange Equilibria.* Langmuir (2007) **23**, p. 5563.

[116] M. Ringler, A. Schwemer, M. Wunderlich, A. Nichtl, K. Kurzinger, T. A. Klar and J. Feldmann, *Shaping Emission Spectra of Fluorescent Molecules with Single Plasmonic Nanoresonators.* Phys. Rev. Lett. (2008) **100**, p. 203002.

[117] J. Seelig, K. Leslie, A. Renn, S. Kuhn, V. Jacobsen, M. vandeCorput, C. Wyman and V. Sandoghdar, *Nanoparticle-Induced Fluorescence Lifetime Modification as Nanoscopic Ruler: Demonstration at the Single Molecule Level.* Nano Lett. (2007) **7**, p. 685.

[118] T. Soller, M. Ringler, M. Wunderlich, T. A. Klar, J. Feldmann, H. P. Josel, Y. Markert, A. Nichtl and K. Kürzinger, *Radiative and Nonradiative Rates of Phosphors Attached to Gold Nanoparticles.* Nano Lett. (2007) **7**, p. 1941.

[119] M. Steiner, C. Debus, A. V. Failla and A. J. Meixner, *Plasmon-Enhanced Emission in Gold Nanoparticle Aggregates.* J. Phys. Chem. C (2008) **112**, p. 3103.

[120] J. Zhang, Y. Fu, M. H. Chowdhury and J. R. Lakowicz, *Metal-Enhanced Single-Molecule Fluorescence on Silver Particle Monomer and Dimer: Coupling Effect between Metal Particles.* Nano Lett. (2007) **7**, p. 2101.

[121] J. Zhang, Y. Fu and J. R. Lakowicz, *Enhanced Förster Resonance Energy Transfer (FRET) on a Single Metal Particle.* J. Phys. Chem. C (2007) **111**, p. 50.

[122] N. Hayazawa, Y. Inouye and S. Kawata, *Evanescent Field Excitation and Measurement of Dye Fluorescence in a Metallic Probe Near-Field Scanning Optical Microscope.* J. Microsc. (1999) **194**, p. 472.

[123] L. Novotny and N. van Hulst, *Antennas for Light.* Nat. Photonics (2011) **5**, p. 83.

[124] P. K. Jain, D. Ghosh, R. Baer, E. Rabani and A. P. Alivisatos, *Near-Field Manipulation of Spectroscopic Selection Rules on the Nanoscale.* Proc. Natl. Acad. Sci. U. S. A. (2012) **109**, p. 8016.

[125] C. L. Jahncke, C. J. Ayars and H. D. Hallen, *Raman Selection Rules in the Presence of an Electric Field Gradient.* Microsc. Microanal. (2002) **8**, p. 1518.

[126] I. Horcas, R. Fernández, J. M. Gómez-Rodríguez, J. Colchero, J. Gómez-Herrero and A. M. Baro, *WSXM: A Software for Scanning Probe Microscopy and a Tool for Nanotechnology.* Rev. Sci. Instrum. (2007) **78**, p. 013705.

[127] Nanotec Electronica, *WSxM Software*, accessed on 15.02.2014; available from: www.nanotec.es.

[128] Y. Mushiake, K. Matsumura and N. Nakajima, *Generation of Radially Polarized Optical Beam Mode by Laser Oscillation.* Proc. IEEE (1972) **60**, p. 1107.

[129] R. Oron, S. Blit, N. Davidson, A. A. Friesem, Z. Bomzon and E. Hasman, *The Formation of Laser Beams with Pure Azimuthal or Radial Polarization.* Appl. Phys. Lett. (2000) **77**, p. 3322.

[130] Y. Kozawa and S. Sato, *Generation of a Radially Polarized Laser Beam by Use of a Conical Brewster Prism.* Opt. Lett. (2005) **30**, p. 3063.

[131] M. A. Ahmed, J. Schulz, A. Voss, O. Parriaux, J.-C. Pommier and T. Graf, *Radially Polarized 3 kW Beam from a CO_2 Laser with an Intracavity Resonant Grating Mirror.* Opt. Lett. (2007) **32**, p. 1824.

[132] G. Machavariani, Y. Lumer, I. Moshe, A. Meir, S. Jackel and N. Davidson, *Birefringence-Induced Bifocusing for Selection of Radially or Azimuthally Polarized Laser Modes.* Appl. Opt. (2007) **46**, p. 3304.

[133] A. Ito, Y. Kozawa and S. Sato, *Selective Oscillation of Radially and Azimuthally Polarized Laser Beam Induced by Thermal Birefringence and Lensing.* J. Opt. Soc. Am. B (2009) **26**, p. 708.

[134] F. Enderli and T. Feurer, *Radially Polarized Mode-Locked Nd:YAG Laser.* Opt. Lett. (2009) **34**, p. 2030.

[135] M. Stalder and M. Schadt, *Linearly Polarized Light with Axial Symmetry Generated by Liquid-Crystal Polarization Converters.* Opt. Lett. (1996) **21**, p. 1948.

[136] T. A. Klar, E. Engel and S. W. Hell, *Breaking Abbe's Diffraction Resolution Limit in Fluorescence Microscopy with Stimulated Emission Depletion Beams of Various Shapes.* Phys. Rev. E (2001) **64**, p. 066613.

[137] Z. Bomzon, G. Biener, V. Kleiner and E. Hasman, *Radially and Azimuthally Polarized Beams Generated by Space-Variant Dielectric Subwavelength Gratings.* Opt. Lett. (2002) **27**, p. 285.

[138] M. A. A. Neil, F. Massoumian, R. Juškaitis and T. Wilson, *Method for the Generation of Arbitrary Complex Vector Wave Fronts.* Opt. Lett. (2002) **27**, p. 1929.

[139] T. Grosjean, D. Courjon and M. Spajer, *An All-Fiber Device for Generating Radially and other Polarized Light Beams.* Opt. Commun. (2002) **203**, p. 1.

[140] T. Grosjean, A. Sabac and D. Courjon, *A Versatile and Stable Device Allowing the Efficient Generation of Beams with Radial, Azimuthal or Hybrid Polarizations.* Opt. Commun. (2005) **252**, p. 12.

[141] J.-i. Hotta, H. Uji-i and J. Hofkens, *The Fabrication of a Thin, Circular Polymer Film Based Phase Shaper for Generating Doughnut Modes.* Opt. Express (2006) **14**, p. 6273.

[142] T. Hirayama, Y. Kozawa, T. Nakamura and S. Sato, *Generation of a Cylindrically Aymmetric, Polarized Laser Beam with Narrow Linewidth and Fine Tunability.* Opt. Express (2006) **14**, p. 12839.

[143] D. P. Biss, K. S. Youngworth and T. G. Brown, *Dark-Field Imaging with Cylindrical-Vector Beams.* Appl. Opt. (2006) **45**, p. 470.

[144] G. Machavariani, Y. Lumer, I. Moshe, A. Meir and S. Jackel, *Efficient Extracavity Generation of Tadially and Azimuthally Polarized Beams.* Opt. Lett. (2007) **32**, p. 1468.

[145] P. B. Phua, W. J. Lai, Y. L. Lim, B. S. Tan, R. F. Wu, K. S. Lai and H. W. Tan, *High Power Radially Polarized Light Generated from Photonic Crystal Segmented Half-Wave-Plate.* arXiv:0710.4979v1 [physics.optics] (2007).

[146] T. Grosjean, M. Suarez and A. Sabac, *Generation of Polychromatic Radially and Azimuthally Polarized Beams.* Appl. Phys. Lett. (2008) **93**, p. 231106.

[147] G. M. Lerman and U. Levy, *Generation of a Radially Polarized Light Beam Using Space-Variant Subwavelength Gratings at 1064 nm.* Opt. Lett. (2008) **33**, p. 2782.

[148] S. Sato and Y. Kozawa, *Radially Polarized Annular Beam Generated Through a Second-Harmonic-Generation Process.* Opt. Lett. (2009) **34**, p. 3166.

[149] S. C. Tidwell, D. H. Ford and W. D. Kimura, *Generating Radially Polarized Beams Interferometrically.* Appl. Opt. (1990) **29**, p. 2234.

[150] S. C. Tidwell, G. H. Kim and W. D. Kimura, *Efficient Radially Polarized Laser Beam Generation with a Double Interferometer.* Appl. Opt. (1993) **32**, p. 5222.

[151] H.-C. Chu, C.-H. Kuo and M. H. Huang, *Thermal Aqueous Solution Approach for the Synthesis of Triangular and Hexagonal Gold Nanoplates with Three Different Size Ranges.* Inorg. Chem. (2006) **45**, p. 808.

[152] T. K. Sau and C. J. Murphy, *Seeded High Yield Synthesis of Short Au Nanorods in Aqueous Solution.* Langmuir (2004) **20**, p. 6414.

[153] B. D. Busbee, S. O. Obare and C. J. Murphy, *An Improved Synthesis of High-Aspect-Ratio Gold Nanorods.* Adv. Mater. (2003) **15**, p. 414.

[154] A. Gole and C. J. Murphy, *Seed-Mediated Synthesis of Gold Nanorods: Role of the Size and Nature of the Seed.* Chem. Mater. (2004) **16**, p. 3633.

[155] H.-Y. Wu, H.-C. Chu, T.-J. Kuo, C.-L. Kuo and M. H. Huang, *Seed-Mediated Synthesis of High Aspect Ratio Gold Nanorods with Nitric Acid.* Chem. Mater. (2005) **17**, p. 6447.

[156] N. R. Jana, L. Gearheart and C. J. Murphy, *Wet Chemical Synthesis of High Aspect Ratio Cylindrical Gold Nanorods.* J. Phys. Chem. B (2001) **105**, p. 4065.

[157] T. Mortier, A. Persoons and T. Verbiest, *Two-Step Synthesis of High Aspect Ratio Gold Nanorods.* Cent. Eur. J. Chem. (2006) **4**, p. 160.

[158] X. Kou, S. Zhang, C.-K. Tsung, Z. Yang, Man H. Yeung, Galen D. Stucky, L. Sun, J. Wang and C. Yan, *One-Step Synthesis of Large-Aspect-Ratio Single-Crystalline Gold Nanorods by Using CTPAB and CTBAB Surfactants.* Chem. Eur. J. (2007) **13**, p. 2929.

[159] C. J. Murphy and N. R. Jana, *Controlling the Aspect Ratio of Inorganic Nanorods and Nanowires.* Adv. Mater. (2002) **14**, p. 80.

[160] H. J. Park, C. S. Ah, W.-J. Kim, I. S. Choi, K.-P. Lee and W. S. Yun, *Temperature-Induced Control of Aspect Ratio of Gold Nanorods.* J. Vac. Sci. Technol., A (2006) **24**, p. 1323.

[161] W. E. Moerner, *Those Blinking Single Molecules.* Science (1997) **277**, p. 1059.

[162] S. Link, M. B. Mohamed and M. A. El-Sayed, *Simulation of the Optical Absorption Spectra of Gold Nanorods as a Function of Their Aspect Ratio and the Effect of the Medium Dielectric Constant.* J. Phys. Chem. B (1999) **103**, p. 3073.

[163] L. Novotny, M. R. Beversluis, K. S. Youngworth and T. G. Brown, *Longitudinal Field Modes Probed by Single Molecules.* Phys. Rev. Lett. (2001) **86**, p. 5251.

[164] M. A. Lieb, J. M. Zavislan and L. Novotny, *Single-Molecule Orientations Determined by Direct Emission Pattern Imaging.* J. Opt. Soc. Am. B (2004) **21**, p. 1210.

[165] A. Hartschuh, *Tip-Enhanced Optical Spectroscopy.* Philos. Trans. R. Soc. London A (2004) **362**, p. 807.

[166] M. Fleischer, C. Stanciu, F. Stade, J. Stadler, K. Braun, A. Heeren, M. Haffner, D. P. Kern and A. J. Meixner, *Three-Dimensional Optical Antennas: Nanocones in an Apertureless Scanning Near-Field Microscope.* Appl. Phys. Lett. (2008) **93**, p. 111114.

11 Lebenslauf

Tina Züchner
geboren am 15. Januar 1981 in Reutlingen

Ausbildung und beruflicher Werdegang

- Juni 2000:
  Abitur am Friedrich-Schiller-Gymnasium Pfullingen,
  Leistungsfächer Chemie und Deutsch

- Oktober 2000-Juni 2006:
  Chemie-Studium (Diplom) an der Eberhard Karls Universität Tübingen,
  Wahlpflichtfach Materialwissenschaften
  Stipendium des Studienfonds der Chemischen Industrie (2000-2002)

- Dezember 2005-Juni 2006:
  Diplomarbeit an der Eberhard Karls Universität Tübingen,
  Institut für Physikalische und Theoretische Chemie
  Betreuer: Prof. Dr. Alfred J. Meixner und Junprof. Dr. Achim Hartschuh
  „Neuartige Streulichtmikroskopie an einzelnen Goldnanopartikeln
  – Aufbau eines konfokalen Laser-Mikroskops sowie Untersuchungen zu
  Nachweisgrenze und Bildkontrast"

- seit 2006:
  Promotion an der Eberhard Karls Universität Tübingen,
  Institut für Physikalische und Theoretische Chemie
  Betreuer: Prof. Dr. Alfred J. Meixner
  "High Resolution Optical Microscopy on Single Gold Nanoparticles"

- seit 2012:
  wissenschaftliche Mitarbeiterin am Forschungszentrum Jülich GmbH,
  Institut für komplexe Systeme, Molekulare Biophysik (ICS-5)
  in der Arbeitsgruppe von Prof. Dr. Jörg Fitter

Preise und Auszeichnungen:

Best Poster Award bei der 9th International Conference on Near-Field Optics,
Nanophotonics and Related Techniques, NFO-9, Lausanne (Schweiz) 2006

Young Scientist Award beim 2008 Spring Meeting of the European Materials
Research Society, Strasbourg (Frankreich) 2008

12 List of Publications

Papers

- A. V. Failla, S. Jäger, **T. Züchner**, M. Steiner and A. J. Meixner, *Topology Measurements of Metal Nanoparticles with 1 nm Accuracy by Confocal Interference Scattering Microscopy.*
  Opt. Express (2007) **15**, p. 8532.

- **T. Züchner**, A. V. Failla, A. Hartschuh and A. J. Meixner, *A Novel Approach to Detect and Characterize the Scattering Patterns of Single Au Nanoparticles Using Confocal Microscopy.* J. Microsc. (2008) **229**, p. 337.

- **T. Züchner**, A. V. Failla, M. Steiner and A. J. Meixner, *Probing Dielectric Interfaces on the Nanoscale with Elastic Scattering Patterns of Single Gold Nanorods.*
  Opt. Express (2008) **16**, p. 14635.

- **T. Züchner**, F. Wackenhut, A. V. Failla and A. J. Meixner, *Nanoscale Characterization of Single Au Nanorods by Confocal Microscopy.* Appl. Surf. Sci. (2009) **255**, p. 5391.

- **T. Züchner**, A. V. Failla and A. J. Meixner, *Light Microscopy with Doughnut Modes: A Concept to Detect, Characterize, and Manipulate Individual Nanoobjects.*
  Angew. Chem. Int. Ed. (2011) **50**, p. 5274.

- F. Wackenhut, A. Virgilio Failla, **T. Züchner**, M. Steiner and A. J. Meixner, *Three-Dimensional Photoluminescence Mapping and Emission Anisotropy of Single Gold Nanorods.*
  Appl. Phys. Lett. (2012) **100**, p. 263102.

Talks

- International Conference on Nanoscience and Technology in Basel (Switzerland) 2006:
  T. Züchner, A. V. Failla, A. Hartschuh and A. J. Meixner, *A Novel Method to Detect and Characterize Single Gold Nanoparticles Using Confocal Microscopy.*

- 13th International Workshop on Single Molecule Spectroscopy and Ultrasensitive Analysis in Life Sciences in Berlin (Germany) 2007: **T. Züchner**, A. V. Failla, A. Hartschuh and A. J. Meixner, *Gold Nanorods as Non-Bleaching Labels: a New Confocal Microscopy Technique to Characterize the Scattering Patterns and to Detect their Orientation.*

- 72. Jahrestagung der Deutschen Physikalischen Gesellschaft in Berlin (Germany) 2008:
  T. Züchner, A. V. Failla, A. Hartschuh and A. J. Meixner, *A New Method to Detect and Characterize Single Metallic Nanoparticles Using Confocal Microscopy.*

- Spring Meeting of the European Materials Research Society in Strasbourg (France) 2008:
  T. Züchner, F. Wackenhut, A. V. Failla and A. J. Meixner, *Sensing the Nano Environment of Metallic Nanoparticles with Confocal Interference Scattering Microscopy.*

- 73. Jahrestagung der Deutschen Physikalischen Gesellschaft in Dresden (Germany) 2009:
  T. Züchner, F. Wackenhut, A. V. Failla and A. J. Meixner, *Nanoscale Characterization of Single Metal Nanoparticles by their Scattering Patterns.*

- Frontiers in Optics - Laser Science XXV in Rochester (NY, USA) 2009:
  T. Züchner, A. V. Failla, F. Wackenhut and A. J. Meixner, *Nanoscale Characterization of Single Metal Nanoparticles by their Scattering Patterns.*

- Spring Meeting of the Materials Research Society in San Francisco (CA, USA) 2010:
  T. Züchner, F. Wackenhut, A. V. Failla and A. J. Meixner, *Nanoscale Characterization of Individual Metal Nanoparticles by their Scattering and Luminescence Patterns.*

- 74. Jahrestagung der Deutschen Physikalischen Gesellschaft in Regensburg (Germany) 2010: F. Wackenhut, **T. Züchner**, A. V. Failla and A. J. Meixner, *Characterization of Single Gold Nanoparticles by Using Higher Order Lasermodes*

- 15th European Conference on Spectroscopy of Biological Molecules in Oxford (Great Britain) 2013: M. Gabba, D. Kempe, T. Rosenkranz, **T. Züchner**, A. Katranidis, J. Fitter, *Substrate induced changes in the dynamics of phosphoglycerate kinase studied by single-molecule FRET.*

Posters

- 9th International Conference on Near-Field Optics, Nanophotonics and Related Techniques, NFO⁻⁹ in Lausanne (Switzerland) 2006: **T. Züchner**, A. V. Failla, S. W. Jäger, A. Hartschuh and A. J. Meixner, *A New Approach to Detect and Characterize Scattering Patterns of Single Gold Nanoparticles Using Confocal Microscopy.*

- International Symposium: Optical Analysis of Biomolecular Machines in Berlin (Germany) 2006: A.V. Failla, **T. Züchner**, A. Hartschuh and A.J. Meixner, *Gold Nanorods as Non Bleaching Labels: a Novel Confocal Microscopy Technique to Detect and Characterize their Scattering Patterns.*

- 4th International Conference on Surface Plasmon Photonics, SPP4 in Amsterdam (the Netherlands) 2009: **T. Züchner**, A. V. Failla, F. Wackenhut and A. J. Meixner, *Nanoscale Characterization of Single Metal Nanoparticles by their Scattering Patterns.*

- SPIE NanoScience + Engineering in San Diego (CA, USA) 2009:
  T. Züchner, A. V. Failla, F. Wackenhut and A. J. Meixner,
  Nanoscale Characterization of Single Metal Nanoparticles by their Scattering Patterns.

- International Conference on Spectral Hole Burning in Palm Cove (Australia) 2009:
  T. Züchner, A. V. Failla, F. Wackenhut and A. J. Meixner,
  Nanoscale Characterization of Single Metal Nanoparticles by their Scattering Patterns.

- Bio-Plasmonics Conference Functional Plasmonic Nanostructures for Biosensing in Zürich (Switzerland) 2010: F. Wackenhut, **T. Züchner**, A. V. Failla and A. J. Meixner, *Characteriztion of Single Gold Nanoparticles Using Confocal Interference Microscopy in Combination with Higher Order Laser Modes*

- 11th International Conference on Near-Field Optics, Nanophotonics and Related Techniques, NFO-11 in Peking (China) 2010: F. Wackenhut, A. V. Failla, **T. Züchner** and A. J. Meixner, *Exploring Dielectric Interfaces and their Environment on the Nanoscale by Direct Imaging of Gold Nanorods*

- SPIE NanoScience + Engineering in San Diego (CA, USA) 2011:
  F. Wackenhut, A. V. Failla, **T. Züchner** and A. J. Meixner, *Complete Three-Dimensional Optical Characterization of Single Gold Nanorods.*

- 19th International Workshop on Single Molecule Spectroscopy and Ultra Sensitive Analysis in the Life Sciences in Berlin (Germany) 2013:
  S. Poblete, D. Kempe, **T. Züchner**, A. Schöne, R. Winkler, G. Gompper, J. Fitter, *Interdomain dynamics of phosphoglycerate kinase studied by single-molecule FRET and a random MPC approach.*

- 58th Annual Meeting of the Biophysical Society in San Francisco (CA, USA) 2014:
  M. Gabba, S. Poblete, D. Kempe, A. Schöne, **T. Züchner**, G. Gompper, J. Fitter, *Interdomain dynamics of phosphoglycerate kinase studied by smFRET and a mesoscale hydrodynamics simulation.*